

# Proposal for a Silicon Strip Detector for STAR (SSD)

Abdelkrim Boucham, Stéphane Bouvier, Manoel Dialinas, Cyril Drancourt,  
Barbara Erazmus, Marie Germain, Sandra Giliberto, Gérard Guilloux,  
Hans H. Gutbrod, Bernard Kubica, Richard Lednický<sup>1</sup>, Frédéric Lefèvre,  
Christine Le Moal, Piotr Leszczyński<sup>2</sup>, Lilian Martin, Thierry Milletto,  
Tomasz Pawlak<sup>2</sup>, Walter Pinganaud, Jan Pluta<sup>2</sup>, Johann Rafelski<sup>3</sup>,  
Olivier Ravel, Fabrice Retiere, Louis-Marie Rigalleau, Christelle Roy

*SUBATECH, Université de Nantes/Ecole des Mines de Nantes/IN2P3/CNRS  
44070 Nantes, France*

*1 Permanent address : Institute of Physics, Prague, Czech Republic*

*2 Permanent address : Institute of Physics, Warsaw University of Technology, Poland*

*3 Permanent address : Department of Physics, University of Arizona, Tucson, USA*

Laurent Arnold, Jérôme Baudot, Jean-Pierre Coffin, Georges Guillaume,  
Lionel Guthneck, Stéphane Higuieret, Francis Jundt, Christian Kuhn,  
Jean-Robert Lutz, Alain Michalon, Christophe Suire, Alberto Tarchini

*IReS, IN2P3-CNRS/ULP-PB28, 67037 Strasbourg, France*

Jean-Daniel Berst, Jean-Philippe Blondé, Claude Colledani,  
Luc Hébrard, Wojciech Duliński

*LEPSI, BP28, 67037 Strasbourg, France*

Rene Bellwied, Claude A. Pruneau, Ken W. Wilson

*Physics Department, Wayne State University, Detroit, USA*

# Contents

<b>1</b>	<b>Physics capabilities</b>	<b>4</b>
1.1	<b>Global simulation of the SSD in the STAR detector</b>	<b>4</b>
1.1.1	Tracking strategies . . . . .	4
1.1.2	Impact of the SSD on STAR tracking capabilities . . . . .	6
1.1.3	Improvement of the track finder and future plans . . . . .	11
1.1.4	Low transverse momentum particles . . . . .	12
1.1.5	Impact of the SSD on the TPC . . . . .	14
1.2	<b>Strangeness as observable of QGP</b>	<b>16</b>
1.3	<b>Light-particle correlations at STAR</b>	<b>19</b>
1.3.1	Introduction . . . . .	19
1.3.2	Detector performances . . . . .	21
1.3.3	Simulations . . . . .	21
1.3.4	Identical-pion correlations . . . . .	23
1.3.5	Correlations of identical kaons . . . . .	26
1.3.6	Two-proton correlations . . . . .	28
1.3.7	Non-identical particle correlations . . . . .	30
1.3.8	Correlations of short-lived particles . . . . .	32
1.3.9	Conclusions . . . . .	32
1.4	<b>Search for exotic forms of strange matter with STAR</b>	<b>33</b>
1.4.1	Detection ability of exotic strange object in STAR . . . . .	34
1.4.1.1	Long-lived objects . . . . .	35
1.4.1.2	Short-lived objects . . . . .	37
1.4.1.3	Unstable objects . . . . .	40
<b>2</b>	<b>Performances of Silicon Microstrip detectors</b>	<b>43</b>
2.1	<b>Detector Response Simulation</b>	<b>43</b>
2.1.1	Intrinsic spatial resolutions . . . . .	43
2.1.2	Charge matching efficiency . . . . .	45
2.1.3	Number of ambiguous hits, overlapping clusters and resolved particles	45
2.2	<b>Tests of Silicon Microstrip detectors</b>	<b>48</b>
2.2.1	Introduction . . . . .	48
2.2.2	Single-sided versus double-sided microstrip detectors . . . . .	48
2.2.3	Tested detectors . . . . .	48
2.2.4	Experimental setups . . . . .	48

2.2.5	Extraction of the noise and the signal from the raw data . . . . .	49
2.2.6	Determination of the mean track positions . . . . .	49
2.2.7	Spatial resolution . . . . .	52
<b>3.</b>	<b>Design of the Silicon Strip Detector</b>	<b>55</b>
<b>3.1</b>	<b>General characteristics of the SSD</b>	<b>55</b>
<b>3.2</b>	<b>Silicon strip detectors</b>	<b>57</b>
<b>3.3</b>	<b>SSD mechanics</b>	<b>59</b>
3.3.1	Mechanical requirements . . . . .	59
3.3.2	Clamshell structure . . . . .	59
3.3.3	Ladder . . . . .	60
3.3.4	Mechanical assembly . . . . .	60
<b>3.4</b>	<b>Mechanical interface between TPC and SVT</b>	<b>61</b>
3.4.1	Requirements . . . . .	61
3.4.2	Design . . . . .	61
<b>3.5</b>	<b>Readout system</b>	<b>66</b>
3.5.1	Description of the readout system . . . . .	66
3.5.2	The Front End Electronics . . . . .	67
3.5.3	Hybrids circuit . . . . .	69
3.5.4	Detector and FEE module . . . . .	70
3.5.4.1	Connection between the silicon strip detector and the front end electronics . . . . .	70
3.5.4.2	Connections between FE electronics and the rest of the system	71
3.5.5	ADC&control board . . . . .	71
3.5.6	Readout control board . . . . .	72
3.5.7	DAQ . . . . .	73
3.5.7.1	Readout via the GigaLink . . . . .	73
3.5.7.2	Data processing with the STAR ASIC . . . . .	74
3.5.8	Readout timing . . . . .	75
<b>3.6</b>	<b>Slow control</b>	<b>76</b>
3.6.1	Specifications . . . . .	76
3.6.2	Communication . . . . .	76
3.6.3	Power supply . . . . .	77
3.6.4	High voltage monitoring . . . . .	77
3.6.5	Temperature control . . . . .	77
3.6.6	FEE control and test . . . . .	77

3.6.7 Opto isolation . . . . .	78
3.6.8 Alternative option . . . . .	78
<b>3.7. Front End Electronics Cooling Systems</b>	<b>78</b>
3.7.1 Water Cooling . . . . .	78
3.7.2 Air Cooling . . . . .	80
<b>4. Integration issues</b>	<b>84</b>
<b>4.1 Total power dissipation</b>	<b>84</b>
4.1.1 Evaluation of the SSD barrel power dissipation . . . . .	84
<b>4.2 Timing</b>	<b>84</b>
4.2.1 TPC timing requirement . . . . .	84
4.2.2 SSD trigger requirement . . . . .	84
<b>4.3 TPC high voltage</b>	<b>84</b>
4.3.1 2D simulations . . . . .	87
<b>4.4 Radiation length of the SSD</b>	<b>88</b>
<b>4.5 Cable issues</b>	<b>91</b>
4.5.1 Cables along the cones . . . . .	91
4.5.2 Cables from the TPC wheels to the platform . . . . .	91
4.5.3 Cable crosstalk tests . . . . .	92
<b>4.6 Room requirement on the TPC wheel</b>	<b>93</b>
<b>4.7 Room requirement on the platform</b>	<b>93</b>
<b>Plannings and organization</b>	<b>95</b>
<b>Appendices</b>	<b>103</b>
<b>References</b>	<b>116</b>

# 1 Physics capabilities

## 1.1 Global simulation of the SSD in the STAR detector

In order to evaluate the impact of the SSD layer on both the SVT and STAR capabilities, global simulations have been performed using the different existing STAR software packages.

The SSD geometry has been implemented into GSTAR, the STAR-GEANT simulation package (Fig. 1). The support structures, cooling system, detectors and front end electronics are currently included according to their respective characteristics described in section 3.

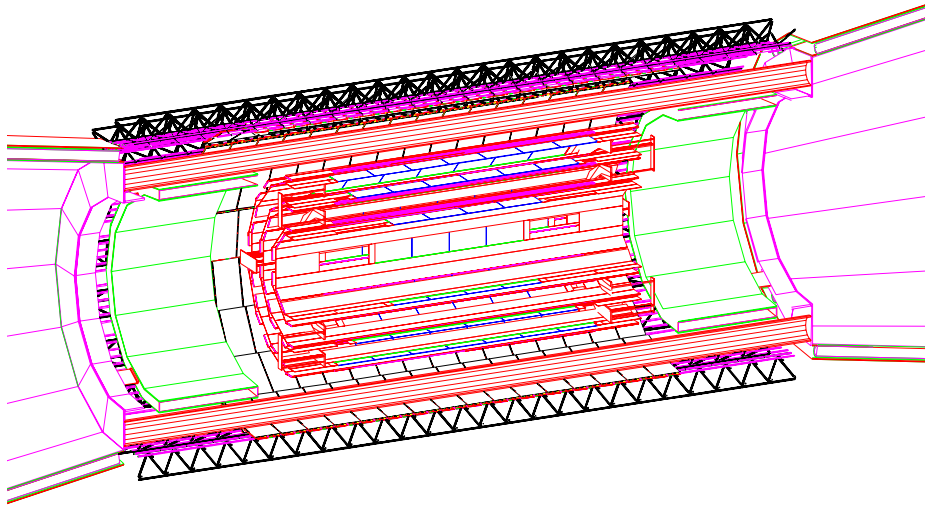


**Figure 1:** 3D view of the SVT and SSD as currently implemented in GSTAR.

### 1.1.1 Tracking strategies

#### *a - Current tracking method in STAR*

The current STAR tracking philosophy is based on separated tracking in the SVT and TPC followed by a matching of the tracks reconstructed in both detectors. The efficiency to reconstruct correctly a complete track depends highly on the individual performances of each track finders since no information on tracks is shared during their application.

The current SVT tracking strategy is a track following method which uses straight-line extrapolation [1]. Starting from the vertex and a given hit in the first SVT layer, a straight-line projection is performed on the second SVT layer and an association to

a hit is done. The associated hit in the second layer is then used to predict a position in the third SVT layer. Track segments of three hits are thus constructed. For the specific tracking of secondary particles, the constraint on the vertex position is less severe i.e. the segment made with the hits in the 1st and the 2nd layers do not need to point to the primary vertex. This tracking method has been optimized for the SVT including 3 layers and produces very good results with such geometry [1, 2].

The SVT tracking method has been applied to search for tracks in the vertex detector including the SSD. The poor results obtained (namely for secondary tracks) in terms of tracking efficiency and number of fake tracks highlighted the failure of such a tracking method when adding a fourth layer to the STAR vertex detector. Indeed, this method does not anticipate the bending of tracks due to the magnetic field and consequently is unable to correctly predict a track projection on the SSD. The specific tracking of secondary particles produces a much higher number of hit associations (the vertex cannot be used to determine an initial track direction) and leads to an intolerable number of fake tracks.

*b - A new tracking method for STAR*

A new tracking strategy, based on the method successfully applied for the ALICE experiment [3], has been developed to take full advantage of the SSD in finding tracks in the STAR vertex detector. As a matter of fact, for a Pb+Pb event at ALICE characterized by a very high multiplicity ( $dN/dy=8000$ ), a tracking efficiency of 90% has been achieved with a probability of fake tracks lower than 5%. This tracking algorithm is a track following method. The basic steps performed are the following :

1. Start with a TPC track projected on the SSD wafers
2. Scan for a possible association of a SSD hit with the TPC track
3. Update of the track parameters including the new hit
4. Calculation of the track projection on the outermost layer of the SVT
5. Scan for a possible association with a hit in the 3rd SVT layer.
6. Two last steps repeated for the 2nd and 1st layers of the SVT

The track finding starts with the TPC tracks with the highest transverse momentum which are less affected by multiple Coulomb scattering. Several iterations are thus made each for a given transverse momentum threshold. All hits associated to a given TPC track are then removed, lowering the hit density in the SVT and SSD layers for the next iterations. A track which cannot be associated to any hit at a given momentum step is presented back at the next iteration where the constraints for hit association are less severe. The sizes of the scanning area around the projection used to look for hit association are set individually for each SVT and SSD layer and each transverse momentum range.

In order to improve the algorithm performances, these iterations are repeated in several passes where different constraints are applied :

- The first pass requires a hit in each layer.
- The second pass looks for segments with at least 3 hits.
- Finally the last pass searches for segments with at least one hit in the SSD or segments with at least a hit in each SVT layer and with enlarged searching areas.

The constraint applied during the first pass is based on two observations. First, a large fraction of the TPC tracks corresponds to particles which left a hit in each layer of the SVT+SSD. Second, when a TPC track is associated with an wrong hit in the SSD, most of the time it leads to a segment with less than 4 hits.

This new tracking method features two important characteristics which should be emphasized :

- No information on the main vertex location was used during the tracking. It implies that the distinction between primary and secondary tracks is irrelevant.
- Although specific conditions are applied during the various passes, no lower limit was set on the number of hits required to form a segment. Segments of SVT+SSD track with a hit missing in a given layer are allowed in order to recover the geometrical and hardware inefficiency of the SVT layers. The current tracking is also successful in dealing with tracks producing two hits in areas of a given layer where wafers are overlapping. Moreover, segments of tracks limited to the outermost layers are found. It implies that secondary tracks produced by short-lived particles decaying within the SVT are simultaneously considered by the current tracking.

### **1.1.2 Tracking performances of the new algorithm and impact of the SSD on STAR tracking capabilities**

In order to quantify the performances of this new tracking method simulations have been performed with Au+Au events produced by Hijing. Several types of tracks have been defined :

- **findable track** : a track reconstructed in the TPC which has at least a hit in the vertex detector and can be found by the track finder.
- **correct track** : a track reconstructed in the TPC with all or a part of its hits in the SVT+SSD correctly associated by the track finder.
- **ghost track** : a track reconstructed in the TPC<sup>1</sup> with one or more wrong hits associated by the track finder.

The **tracking efficiency** is then defined as :

$$\frac{\textit{correct tracks}}{\textit{findable tracks}}$$

and the **ghost track probability** :

$$\frac{\textit{ghost tracks}}{\textit{ghost tracks} + \textit{correct tracks}}$$

Only TPC tracks with  $-1.14 < \eta < 1.14$  (within the SSD acceptance) have been considered by the track finder. Moreover, we use a transverse momentum cut-off limit of 100 MeV/c corresponding roughly to the minimum transverse momentum for a track to punch through the SVT and the SSD and to leave enough hits in the TPC. Below this value the tracking efficiency in the TPC drops rapidly down to zero. Finally the tracking of electrons, positrons and muons was not considered in these studies.

Quite good performances were observed with the new tracking method as illustrated by the Fig. 2 for the SVT+SSD. The transverse momentum distribution of findable tracks, correct tracks and ghost tracks for all, primary and secondary tracks are plotted respectively in the panel A, B and C. The overall efficiency is better than 75% and the probability of producing ghost tracks is limited to 17%. The efficiency depends on the transverse momentum of the track. The efficiency is better than 90% at high transverse momentum and decreases slowly from 500 MeV/c to reach 50% at 100 MeV/c. A better tracking efficiency and ghost track probability are observed for primary tracks than for secondary tracks. The tracking efficiency does not seem to depend on the pseudo-rapidity of the tracks as illustrated by the panel D of the Fig. 2. The number of hits in the SVT+SSD is plotted on the figure 3 for each type of tracks (findable, correct and ghost). One can observe that for the majority of the tracks the full segment of hits is correctly associated to the tracks illustrating the correct behavior of the tracking method.

---

<sup>1</sup>The track finder in the TPC produces itself a small fraction of ghost tracks. For most of them, only one or two incorrect hits are associated to a segment composed of several tens of hits. Consequently the quality of the TPC tracks is only slightly affected by those wrong hits. In addition, a label is attached to the reconstructed TPC track which is given by the real track contributing the most to the segment. When looking for incorrect association in the vertex detector, the SVT+SSD hits are compared to this label.

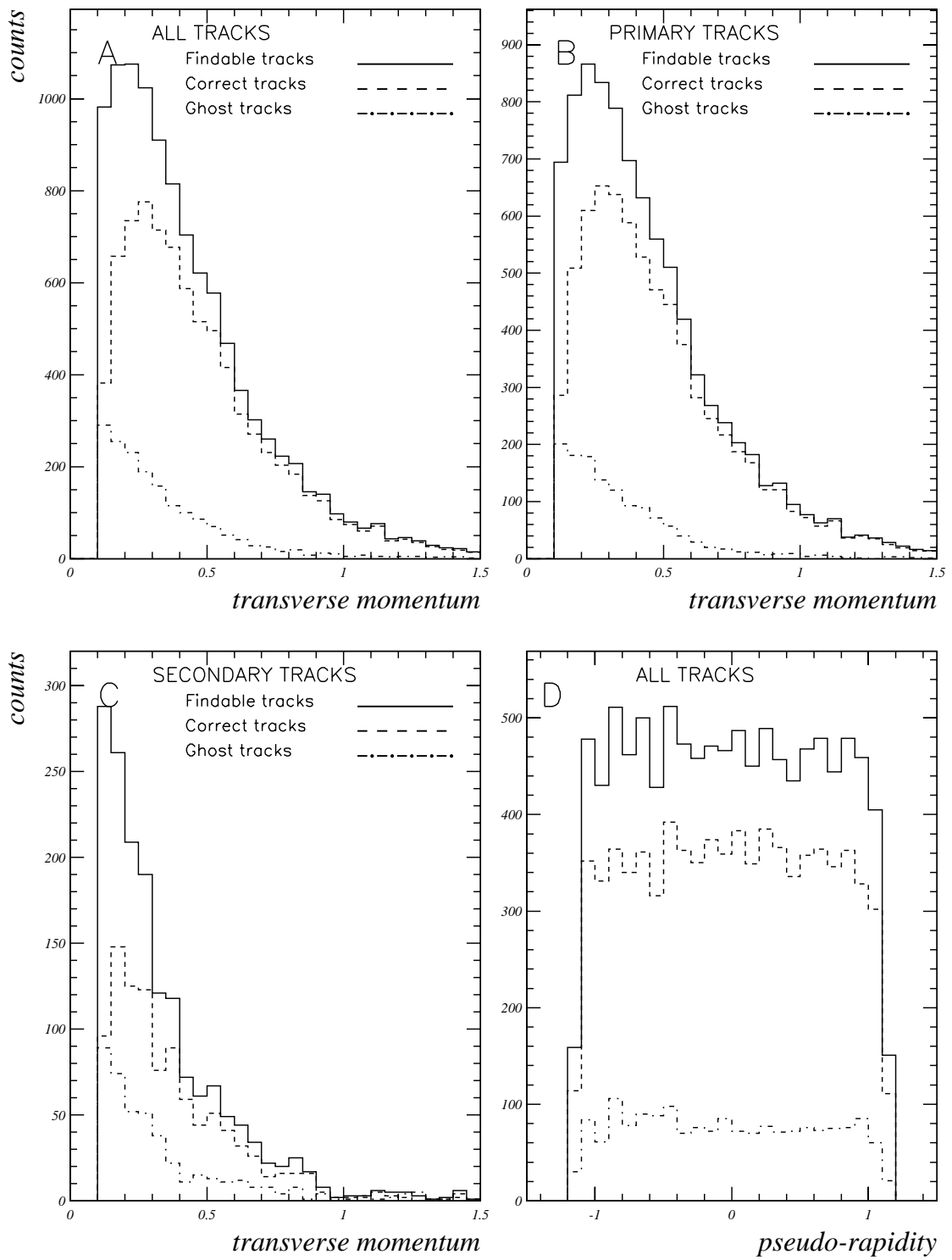


**Figure 2:** Transverse momentum distribution of tracks (A), primary tracks (B) and secondary tracks (C). Pseudo-rapidity distribution of all tracks (D).

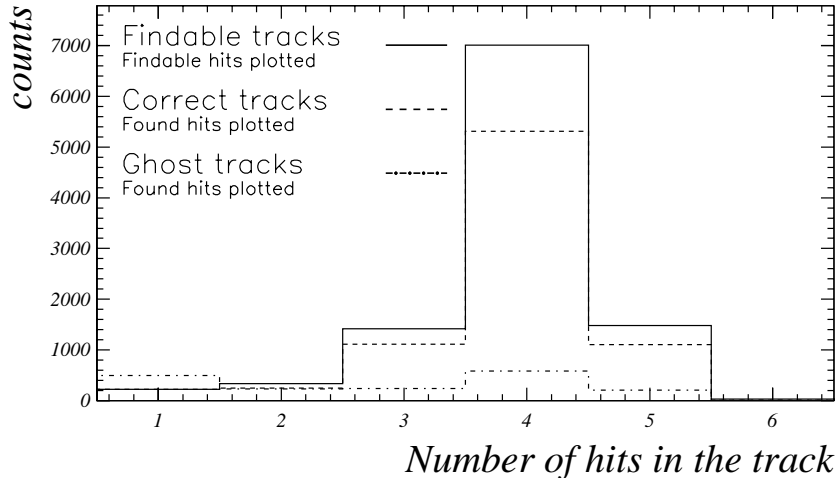


**Figure 3:** Number of hits in the SVT+SSD belonging to the findable tracks, associated to the correct tracks and ghost tracks.

In order to unfold the impact of the new tracking method and the impact of the SSD on the STAR tracking performances, several simulations have been performed with the current and the new tracking algorithms and with a vertex detector including or not the SSD. The results of these simulations are summarized in the tables 1 and 2 for five Hijing events.

In the simulations performed with the new tracking method presented in table 2, the previous definition of a findable track (at least one hit in the vertex detector is required) has been applied. On the other side, one should keep in mind that the current tracking method in the vertex detector requires 3 hits to build a segment. Consequently, in the table 1 a findable track is defined as a track in the TPC which has 3 hits in the SVT and at least 3 hits in the SVT+SSD. A fraction of these tracks is then lost due to tracking inefficiency in the vertex detector and merging inefficiency when combining SVT and TPC tracks. A correct track is then defined as a TPC track correctly associated to a track successfully reconstructed in the vertex detector.

Concerning the primary tracks, the impact of the SSD can be already quantified by looking at the results obtained with the current tracking. The number of correct tracks reconstructed increases by 200 (as the number of findable tracks) which reflects the recovering of the SVT geometrical inefficiency (primary tracks with a missing hit in one of the SVT layers). The number of ghost tracks increases but to a quite acceptable level. The impact of the new tracking method on the reconstruction of primary tracks can be determined by looking at the results on table 2 obtained with the SSD included. The number of correct tracks increases a bit in correlation with

a rise of the number of ghost tracks. From the same table, one can conclude that the new tracking method, without further improvements, is not suited for the SVT without the SSD.

**The addition of the SSD in the vertex detector allows to reconstruct of the order of 1300 primary tracks in STAR, corresponding to a relative gain of 20% compared to a vertex detector with only 3 layers**

Concerning secondary tracks, as already mentioned in the previous subsection, the current tracking method leads to poor results when the SSD is included. In table 1 one can observe that no gain is obtained in the number of correct tracks while the contamination from ghost tracks reaches 50%. Let us quantify the tracking performances for secondary tracks with the new tracking algorithm (table 2). Short-life particle decaying within the SVT and producing hits only in the outermost layers of the vertex detector are considered by the new track finder and explains the strong increase of findable tracks with respect to the numbers estimated for the current tracking. Applying the new tracking to the SVT without the SSD leads to an improved number of correct tracks but with a higher number of ghost tracks. As for primaries, the new tracking (in its current level of development) is not suited for a vertex detector in STAR without the SSD. The new tracking does not lead to better performances for such a geometry.

Only the new tracking method allows to benefit from the addition of the SSD. The number of correct tracks accordingly increases to 200 with a ghost track probability of 30%. These numbers should be compared to 50 reconstructed tracks in the SVT with a ghost probability of 35%. Adopting a conservative point of view with respect the uncertainties on these numbers, a gain of at least 3.5 is obtained in the number of correct tracks.

**The addition of the SSD in the vertex detector combined with the new track finder leads to 200 secondary tracks reconstructed in STAR, corresponding to an increase by a factor of 3.5 compared to a vertex detector with only 3 layers**

	SVT	SVT+SSD
Primary tracks		
Findable	1544	1743
Correct	1156	1366
Ghost	103	158
Secondary tracks		
Findable	189	252
Correct	55	71
Ghost	16	31

Table 1 : Number of findable tracks, correct tracks and ghost tracks obtained with the **current** tracking method with (right column) and without the SSD (left column)

	SVT	SVT+SSD
Primary tracks		
Findable	1760	1778
Correct	833	1399
Ghost	237	263
Secondary tracks		
Findable	282	333
Correct	78	202
Ghost	50	90

Table 2 : Number of findable tracks, correct tracks and ghost tracks obtained with the **new** tracking method with (right column) and without the SSD (left column)

### 1.1.3 Improvement of the track finder and future plans

Several simple ideas can be explored in order to further improve the performances of this new tracking method. The energy loss measured in each layer of the vertex detector is currently ignored in this algorithm. Rejection criteria could be set by comparing the energy loss recorded in the TPC to the one measured in the SVT+SSD layers.

We are also considering the implementation of hit sharing in the tracking algorithm, i.e. the possibility for a hit to be associated to several tracks. In the current version, hits in the SVT and the SSD are either associated to a unique track or not used at all. Each time a wrong hit is associated to a given track, it induces not only a ghost track but also it compromises the chances to find the track it belongs to. By allowing hit sharing the tracking efficiency is expected to improve.

In a symmetric way, we are investigating the possibility for connecting a TPC track to more than one hit in a given layer of the SVT+SSD. The decision on the final hit-to-track association will be delayed until the SVT layers are completely scanned and more information on the track is available. Moreover, leaving open the option of connecting a given TPC segment to nearby tracks in the vertex detector will preserve the two-track separation in the SVT and SSD expected to be higher than in the TPC. The sample of track pairs with very small relative momenta will consequently be improved allowing to perform a quality analysis of identical particle interferometry.

In the near future we are planning to take advantage of the efforts already made in STAR to implement a tracking strategy based on the Kalman filtering [4] which can be seen as the ultimate development of our new tracking method. This track following method has been successfully applied in high-energy experiments and it presents several advantages :

- track finding and track reconstruction are done simultaneously.
- wrong hit can be rejected during the progressive track finding.
- requiring the propagation of small matrices only, the method is rather fast.
- the method is quite successful in connecting segments of tracks from one detector to another one.

### 1.1.4 Low transverse momentum particles

The dynamics of the low-momentum degrees of freedom is strongly related to collective behavior and condensate phenomena characterizing the change in the structure of strongly interacting matter.

Low momentum particles are quite difficult to find using track following methods due to significant amount of energy loss and large contribution of the multiple scattering in the layers of the vertex detector. For low transverse momentum tracks

which do not reach the TPC, we are planning to develop a global tracking method following the tracking of higher transverse momentum particles. Several methods can be considered like neural network algorithm [3, 5] or grouping algorithm [6]. A good efficiency in finding low  $p_t$  particles relies on very efficient track finding of higher momentum tracks in order to strongly reduce the hit density in the SVT and SSD layers and consequently to limit the probability of wrong associations of hits produced by low energy particles. Neural network method has been applied in ALICE with tracking efficiency higher than 75% for pions with transverse momentum down to 60 MeV/c.

The addition of an extra space-point from the SSD layer should improve the momentum resolution of low  $p_t$  tracks in the vertex detector. For primary tracks one can expect an improvement of the quality of the curvature fit while for secondary tracks it allows to replace a circular track calculation from a set of three points by a real track fit. Performances in term of momentum resolution for the SVT and the SVT with the SSD are summarized in the Fig. 4. Simulations were performed on 10 Hijing events considering pions with  $p_t < 200 \text{ MeV}/c$ . Above this value, the tracking efficiency in the TPC is quite high and consequently provides a much better momentum measurement. Fig. 4 indicates that the primary track momentum resolution improves typically from 18 % to 14 % when adding the SSD.

One should note a deterioration of the resolution at very low  $p_t$  due to an increasing energy loss of the particles trough the successive layers and a larger contribution of the multiple scattering. Corrections for energy loss of the track calculation should improve the momentum resolution [2].

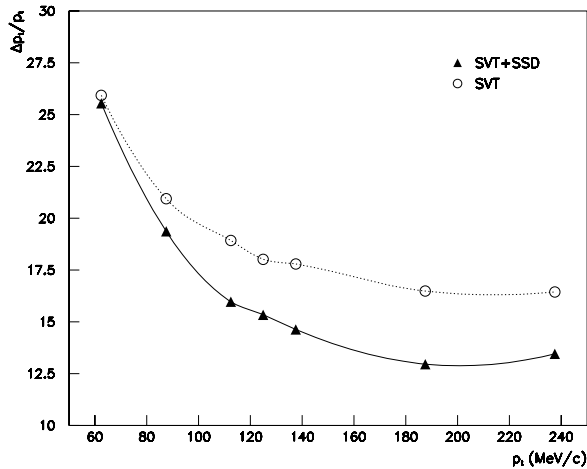


**Figure 4:** Momentum resolution for pions in the SVT+SSD as a function of the transverse momentum for primary tracks.

## 1.1.5 Impact of the SSD on the TPC

### TPC momentum resolution

Analytical calculations have been performed by V.Rykov in order to evaluate the impact of the vertex detector on the TPC momentum resolution. Fig. 5 shows that the addition of the SSD layer does not degrade significantly the TPC momentum resolution. One should note that in these calculations, the SVT and the SSD were considered as passive material. The use of information from the SVT+SSD (especially on the vertex position) would lead to better results.

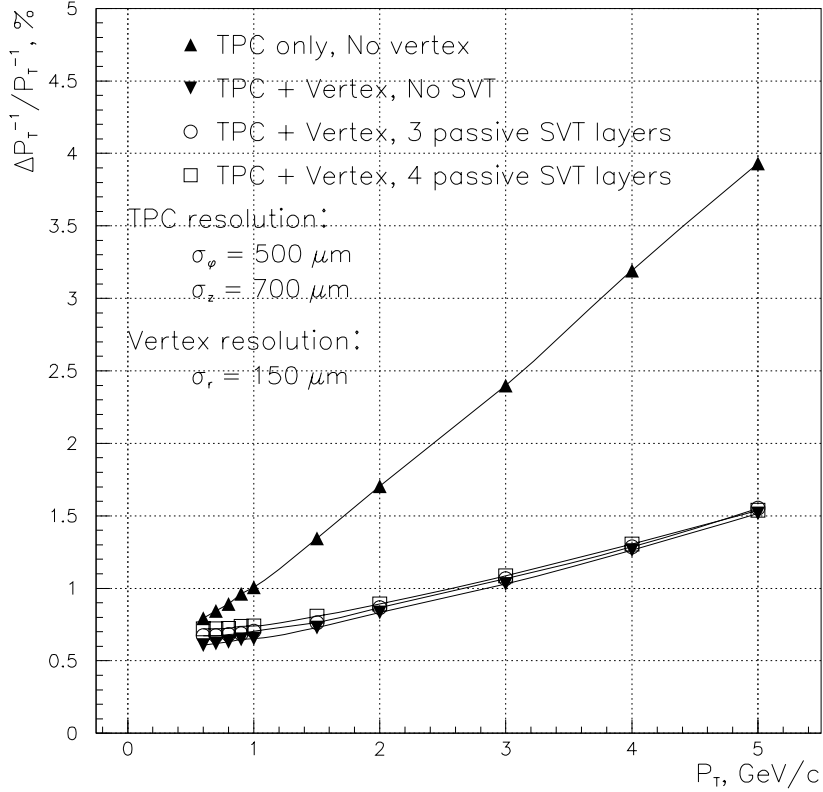


**Figure 5:** Impact of the SSD layer on the TPC momentum resolution

### Yield of TPC tracks induced by the SSD

Among the tracks recorded in the TPC, three categories can be distinguished : primary tracks coming from the interaction point, secondary tracks produced by short-lived particle decays and secondary tracks resulting from interactions within the different encountered materials. GEANT simulations have been done in order to evaluate the yield of charged particles produced by the SSD and leaving hits in the TPC.

To be relevant, this evaluation has to be compared to other sources of tracks coming from produced particles, labeled as follow :

- primaries :coming from the main vertex.
- decays : which spontaneously decay and interact in gas or low density materials.
- pipe : in the beam pipe
- TPC : in dense material of the TPC and the TPC endcaps.
- FTPC : in the FTPC dense material.
- cones : in the SVT+SSD supporting cones.
- SVT : in the SVT material.
- SSD : in the SSD material.

The relative yields of the different contributions are represented in Fig. 6. 1% of the TPC tracks is coming from interactions in the SSD. From this result, one can conclude that the impact of the SSD is marginal when compared to the other sources of tracks.

A similar study regarding the produced hits in the TPC leads to a contribution from the SSD of 0.8 % which can be compared to a contribution of 2.9 % from the beam pipe.

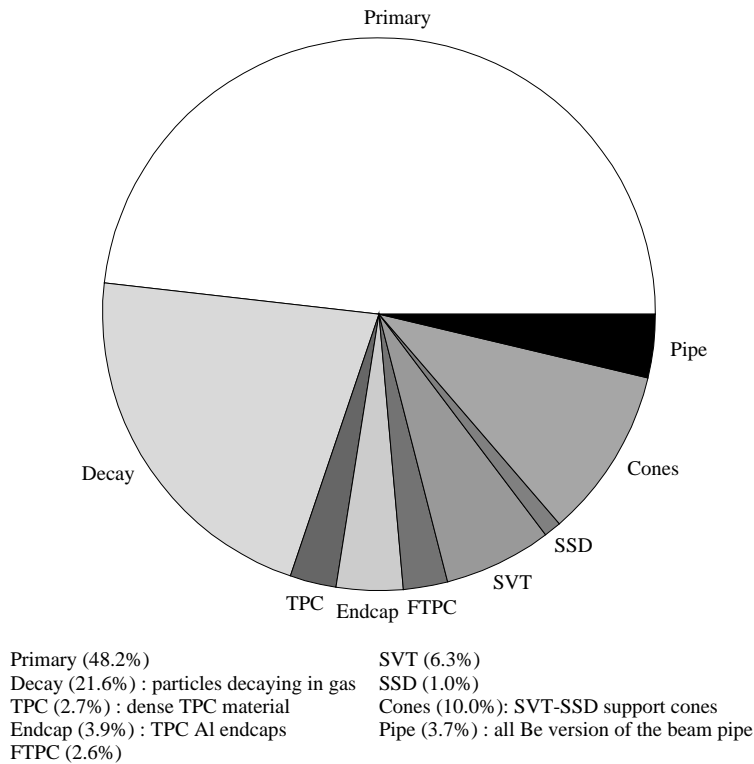


**Figure 6:** Sources of tracks which leave at least one hit in the TPC.

## 1.2 Strangeness as observable of QGP

The difficult problem of studying the properties of very short lived dense hadronic matter and detecting reliably the formation of possibly new phases of matter such as quark-gluon plasma, existing only  $0.5 \cdot 10^{-22}$ sec, has not been completely resolved today. We would like to refine the capability of the STAR detector such that certain longer lived strange particles can be detected with greater efficiency and precision, creating a more effective diagnostic tool of the dense state created in nuclear collisions at 100 A GeV center of mass energy.

Strangeness has been predicted already 15 years ago to be abundantly produced should the deconfined QGP phase be formed (for early references see [7, 8]). Further study has confirmed that it is not reannihilated in rapid decomposition of the dense matter state and that the pattern of strange particle production is specific for the state of matter formed, its evolution and hadronization process. Because there are many different strange particles, we have a very rich field of observables with which it is possible to explore diverse properties of the particle source. Theoretical calculations [10, 11] show that glue-gluon fusion reactions in the QGP would provide a sufficiently fast and thus far an unique mechanism leading to an understanding of strangeness enhancement in terms of basic p-QCD processes.

Today, it has been seen in SPS experiments up to 200 A GeV that overall particles containing strangeness are indeed produced more abundantly in relativistic nuclear collisions. Through the diligent work of the NA35/NA49 collaboration, which has developed a complex '4 $\pi$ '-detectors, a strangeness production excess of about factor a two over expected yields based on simple scaling of  $N-N$  reactions has been today established[12]. Equally significantly, the work of WA85/94/97 collaborations [13, 14, 15] as well as that of NA35/49 [16] for the ratio  $\bar{\Lambda}/\bar{p}$ , shows that the abundance of strange antibaryons is rather unusual in that production pattern of these particles appears to arise in manner expected from the evaporation from the deconfined QGP phase[9]. For example, the remarkable observation that the yield of strange antibaryons  $\bar{\Lambda} + \bar{\Sigma}$  exceeds the yield of antipartons[16] is quite unexpected for a reaction picture involving confined particles. On the other hand it is a rather natural consequence for particles evaporated from deconfined QGP phase in which strange and non-strange quarks have reached chemical equilibrium[7]. Unfortunately, this spectacular result of the NA35 collaboration, is marred by lack of precision, one can still argue that the surprise is comprised in few standard deviations, and thus could still go away. It is our hope that the fully developed STAR tracking will allow to see such anomalous effects at the level of precision which will allow to perform detailed comparison with theoretical models, establishing the production mechanisms and thus the formation of deconfined phase.

As implied in above qualitative discussion, there are two generic strangeness observables which allow further diagnosis of the physical state produced in relativistic heavy ion interactions:

- absolute yield of strangeness: Once produced in hot and dense hadronic matter, *e.g.*, the QGP phase, strangeness/charm is not reannihilated in the evolution of the deconfined state towards freeze-out, because in the expansion and/or cooling process the rate of production/annihilation rapidly diminishes and becomes negligible. Therefore the massive flavor yield is characteristic of the initial state, most extreme conditions, including the approach to chemical equilibrium of gluons in the deconfined phase.
- phase space occupancy  $\gamma_i$ [17]:  $\gamma_i$  describes how close the flavor yield per unit of volume ( $i = s, c$ ) comes to the chemical equilibrium expected;  $\gamma_i$  impacts strongly the distribution of flavor among final state hadronic particles.

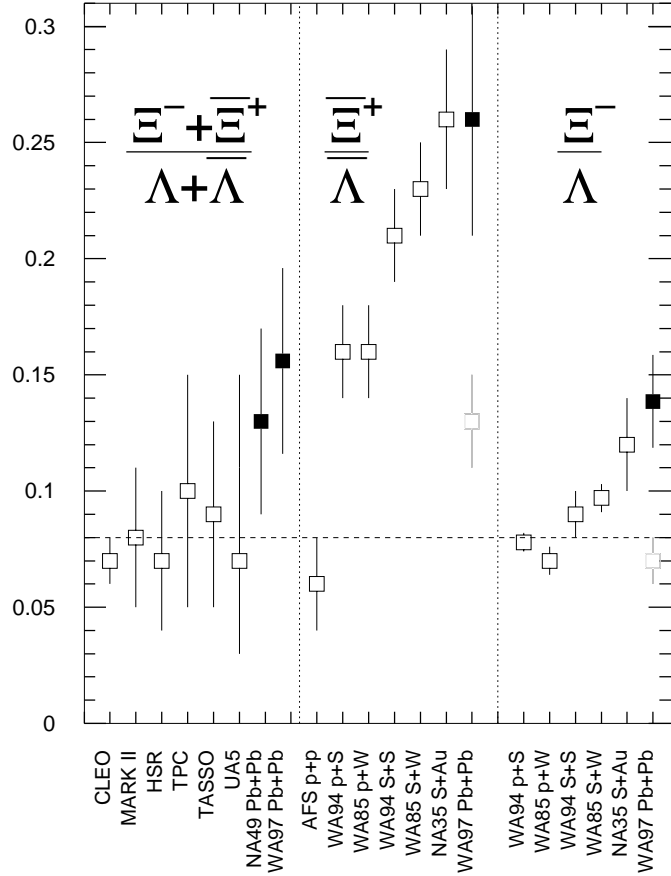


**Figure 7:** Sample of World results (as ‘function’ of experiment name) for yields involving ratio of strange to non-strange quarks in baryons. Dark squares: recent Pb–Pb results.

This rise of  $\gamma_s \rightarrow 1$ , which in the collision occurs rapidly as function of time, and leads to a large freeze-out value seen in experiment, as observed in nuclear collisions at 160–200 A GeV, is believed to be at the origin of the significantly enhanced abundance of multistrange particles. In Fig. 7 we display a world sample of and note a persistent and visible trend to enhance the ratio of cascades (ssq) compared to lambdas (sqq) with increase of the projectile-target system size. The data is drawn from diverse contributions to the Strangeness in Quark Matter conferences (see Refs. [18, 19, 20] and updates presented at QM97 in Tsukuba).

The relative total abundance of strangeness is most related to the initial condition, the ‘hotter’ the initial state is, the greater the production rate, and thus the final state relative yield, to be measured with respect to baryon number or global particle multiplicity (entropy). The phase space occupancy of strangeness  $\gamma_s$  depends aside of the initial production rate, on the final state dilution characterized by dynamics of the expansion and the freeze-out temperature. We believe that we will be able to use observed features of strange mesons, baryon and antibaryon production to see the formation of the deconfined state and to study some QCD properties and parameters. Experience with the analysis at SPS energies confirms that validity of this method to the study of the deconfined phase, though the precision of the SPS results so far has not sufficed to convince everyone that indeed a QGP phase has been formed. However, the strange particle production results obtained at 160–200 A GeV are found to be well consistent with the QGP formation hypothesis.

### Reconstruction of short-lived particles

The vertex detector is the key detector for strange particle ( $\Lambda$ ,  $\Xi$  and  $K_s^0$ ) identification. The SSD increases the hardware efficiency of the vertex detector. Indeed, the SVT detector geometry induces 6% of dead area per layer and the arrangement of the SSD detector is such that these inactive zones are nearly fully recovered.

The total reconstruction efficiency of short-lived particles combines the branching ratio (the probability of decaying in charged secondary particles, e.g.  $\Lambda \rightarrow \pi^- + p$ ), the secondary tracking efficiency and the efficiency of finding the secondary vertex.

The secondary tracking efficiencies can be deduced from tables 1 and 2. The current algorithm for the SVT+TPC leads to an efficiency of 30 % (55/189). It includes the efficiency of reconstructing tracks in both the SVT and the TPC which are correctly matched. For the SVT+SSD+TPC setup, the new track finder predicts an efficiency of 60 % (202/333). It includes the efficiency of reconstructing a track in the TPC and successfully extending it to the SVT+SSD layers.

Table 3 details the overall  $\Lambda$  reconstruction for the SVT+TPC and the combined SVT+SSD+TPC. The addition of the SSD leads to an increase by a factor 4 of the reconstructed  $\Lambda$ . Similar estimations have been done for  $\Xi$  and  $K_s^0$  leading to respectively an increase by 8 and 4 of the number of reconstructed short-lived particles.

The strong increase of the reconstruction efficiency leads to a better identification of strange particles and opens a new possibility of the measurement of various correlations of these short-lived particles (see section 1.3.8).

	SVT+TPC	SVT+SSD+TPC
Branching ratio	0.64	0.64
Secondary tracking efficiency	$0.3^2 = 0.09$	$0.6^2 = 0.36$
Vertex finding efficiency	0.67	0.67
<b>Total reconstruction efficiency</b>	<b>0.038</b>	<b>0.154</b>

Table 3: Lambda reconstruction efficiency for SVT+TPC and SVT+SSD+TPC

## 1.3 Light-particle correlations at STAR

### 1.3.1 Introduction

The correlation function of light particles with nearby velocities is sensitive to the relative space-time distances between the emission points due to the effects of Bose-Einstein or Fermi-Dirac statistics (in the case of identical particles) [21, 22] and the strong and Coulomb final state interactions [24]-[27].

In particular, the shape of the correlation function of two charged particles (identical or non-identical) emitted at large relative distances in their c.m.s. is mainly determined by the Coulomb interaction and is increasingly sensitive to this distance with increasing particle masses and charges, i.e. with decreasing Bohr radius of the particle pair.

The features of emitting sources can be investigated in the framework of an approach which includes the dynamics of the emission process as well as the effects of quantum statistics (QS) and final state interactions (FSI). Different mechanisms are considered in theoretical models: string and color rope formation, hydrodynamical expansion, resonance production, rescattering, mean field effects etc., and finally the deconfinement transition and the creation of quark-gluon plasma (QGP). The identical-particle interferometry yields important information on the relative space-time distances between the emission points of the particles of given type. Under certain conditions this relative information can be transformed into the absolute one, such as the decoupling proper time in the case of an expansion process. On the other hand, the correlations of non-identical particles appear to be directly sensitive to the space-time asymmetries (particularly the delays) in particle emission and thus can serve as a new source of the important complementary information to the standard interferometry measurements.

In fact, it can be shown [27] that the directional analysis of the correlations of two non-identical particles, in contrast to the identical ones, allows to measure the differences in the mean emission times of various particle species, including their signs ( see Fig.8 ).

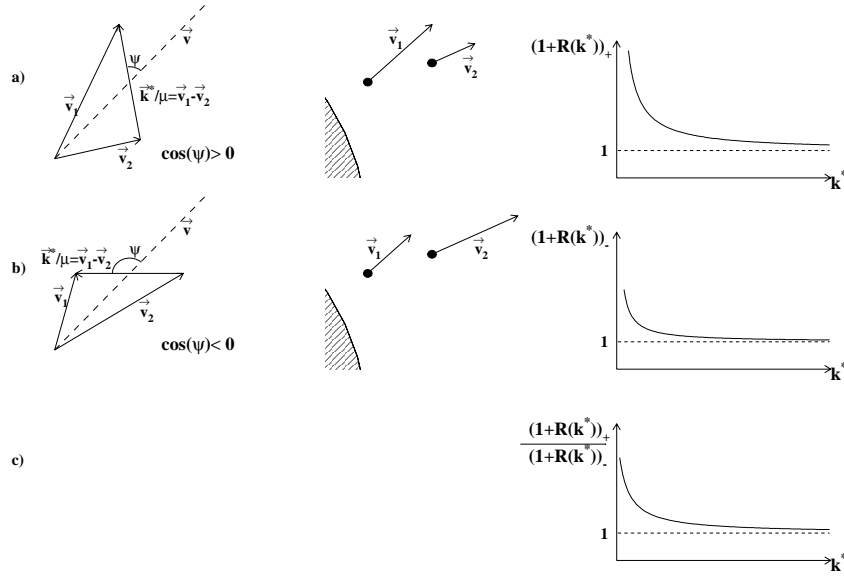


**Figure 8:** To determine which sort of particles was produced earlier and which later we can study the correlation functions of two non-identical particles separately for the angles less and greater than  $90^\circ$  between the relative velocity  $\vec{k}^*/\mu$  ( $\vec{k}^* = \vec{p}_1^* = -\vec{p}_2^*$  and  $\mu$  is the reduced mass of the two particles) and the total pair velocity  $\vec{v}$  (see text).

The sign of the mean time difference  $\langle t \rangle$  can be determined provided the sign of the scalar product  $\mathbf{k}^* \cdot \mathbf{v}$  is fixed. A straightforward way to determine  $\langle t \rangle$  is to measure the correlation functions  $R_+(\mathbf{k}^* \cdot \mathbf{v} \geq 0)$  and  $R_-(\mathbf{k}^* \cdot \mathbf{v} < 0)$ . Depending on  $\langle t \rangle$ , their ratio  $R_+/R_-$  should show a peak or a dip in the region of small  $k^*$  and approach 1 at  $k^* \rightarrow \infty$ .

As the sign of the scalar product  $\mathbf{k}^* \cdot \mathbf{v}$  is practically equal to that of the difference of particle velocities  $v_1 - v_2$  (this equality is always valid for particles of equal masses), the sensitivity of the correlation functions  $R_+$  and  $R_-$  to the sign of the difference of particle emission times has a simple explanation in terms of the classical trajectory approach (see, e.g., [28]). The interaction between the particles in the case of an earlier emission of the faster particle will be different compared with the case of its later emission (the interaction time being longer in the latter case leading to a stronger correlation).

This method opens a new possibility to determine, in a model independent way, which sort of particles ( $K^+, K^-, \pi^+, \pi^-, p, \dots$ ) was emitted earlier and which later at very short time scales of several fm/c or higher. In particular, this effect could be useful to indicate the formation of QGP. Note that usually kaons are expected to be emitted earlier than pions due to their larger mean free path. In the case of strangeness distillation from the mixed hadronic and QGP phase a delay is expected between the emission of strange and antistrange particles.

Concerning the methodical problems, the correlation function of non-identical particles, contrary to the case of identical pairs, is practically not influenced by the two-track resolution. The influence of the momentum resolution is expected to be similar as in the case of identical particle interferometry.

### 1.3.2 Detector performances

The correlation measurements are influenced by the characteristics of the experimental device. Due to the large *acceptance* as well as good *particle identification*, *momentum resolution* and *two-track separation* the STAR detector is well suited for correlation studies. The addition of the SSD will still improve the STAR capabilities to perform interferometry measurements.

- The number of low momentum pairs will strongly increase due to the rise of the hardware efficiency and the improved tracking efficiency. This improvement will be particularly significant for unlike particle pairs registered with very different momenta in the laboratory frame.
- The improved momentum resolution of the SVT/SSD combination in a stand-alone mode will allow studies of the interferometry effects for very low momentum particles, particularly serving a possibility for the observation of the multi-boson condensation effects.
- The two-track resolution of the silicon layer is comparable to the one of the SVT [2] which is an order of magnitude better than the TPC resolution. The large track length due to the SSD will allow to reach a much better overall two-track resolution and two-particle momentum resolution.
- The particle identification performance at low momenta, will be improved due to the additional dE/dx measurement provided by the SSD.
- The contribution of the SSD will be particularly important for the strange particle correlations due to the enhanced efficiency of their detection (see section 1.3.8).

### 1.3.3 Simulations

Our simulations were performed using the String Model for Ultrarelativistic Hadronic Interactions VENUS (version 5.21) [29, 30], a new approach providing a link between the string model and thermal approaches.

The model provides space-time and momentum space characteristics of the freeze-out points of different particle species, which can be used as a reasonable approxima-

tion accounting for the presently known basic features of the multiparticle emission process, including the fast longitudinal motion of the particle sources and resonance production. Besides, it allows to expand the space-time extent of the production region or introduce the shifts in emission times of various particle species and thus to test the possibility to observe such phenomena in the STAR experiment.

Our correlation analysis is based on the generation of Pb-Pb reactions at  $\sqrt{s} = 200 \cdot A$  GeV followed by the calculation of the correlation function for the selected pairs of identical or non-identical particles. The events were generated without the phase of the particle rescattering and droplet formation which normally lead to an increase of the space-time characteristics of particle emission. Instead, we introduce the scale factor changing these characteristics in a controlled way. It allows us to study the sensitivity of the STAR detector to particular correlation effects.

The correlation functions were calculated using the momentum vectors of the selected particles in the CMS. For each pair of identical or non-identical particles the relative coordinates of the emission points and the relative momenta were calculated, and the corresponding weight was attributed including the effects of quantum statistics (for identical particles) as well as the final state (strong and Coulomb) interactions. In this way we have taken into account not only the effects of the relative motion of particles but also the velocity of the pair in the CMS.

The correlation effects are studied here for three particle species: pions, kaons, protons and for some combinations of them. Correlations of identical and non-identical particles are taken into account separately. For each particle pair emission two extreme classes of the space-time characteristics are considered. First, a direct output of the Venus (string-phase) generation is considered. It gives rather underestimated sizes of the emission region. Second, these values are multiplied by the scale factor  $\alpha$ . The results presented here were obtained for  $\alpha = 3.0$ . The mean direct value of the particle emission radius is about 5 fm and the time about 4 fm/c in the CMS. The scaled values are of the order of 15 fm.

To analyze the influence of the detector resolution on the correlation functions we have applied the Gaussian smearing of particle momentum components on the base of estimated experimental resolution. This approach does not take into account the double-track resolution and the directional dependence of the resolution in different momentum components. Keeping it in mind we consider only the correlation function in  $Q_{inv}$  where the directional dependences are not of primary importance. This preliminary estimation of the detector resolution can be simply improved using the momentum values resulting from the tracking algorithms [31].

All detected particles are divided into three classes. First one includes the particles registered by all the detection chain SVT+SSD+TPC, ( $0.05 < P_t < 2.50$ ) GeV/c. Most of particles of this class are registered by the TPC and the precision of measured momenta is determined in this case by the TPC resolution. In our simulations we have assumed that the momenta of all the particles with  $P_t > 0.2$  GeV/c were measured with the resolution  $(\Delta(1/P_t)/(1/P_t)) = 0.9\%$ .

The class of particles with the smallest  $P_t$  values ( $0.05 < P_t < 0.20$ )  $GeV/c$  is for several reasons especially interesting. However a good particle identification and precise momentum determination are very difficult in this region. The momentum resolution is determined by the SVT or SVT+SSD resolution capabilities. This class is treated separately in our analysis.

Two sub-cases of particle detection are considered separately. In the first, the momentum resolution corresponds to that of the SVT+SSD ( $\Delta(1/P_t)/(1/P_t) = 10\%$ ). In the second case the particle detection by the SVT alone is considered and the resolution value is set to 15%. The amount of particles which belong to this class is determined by the  $p_t$  distribution and illustrated in the Fig.9 for pions, kaons and protons. In all the cases considered here the particle rapidity is limited to the interval ( $-1 < Y < 1$ ).

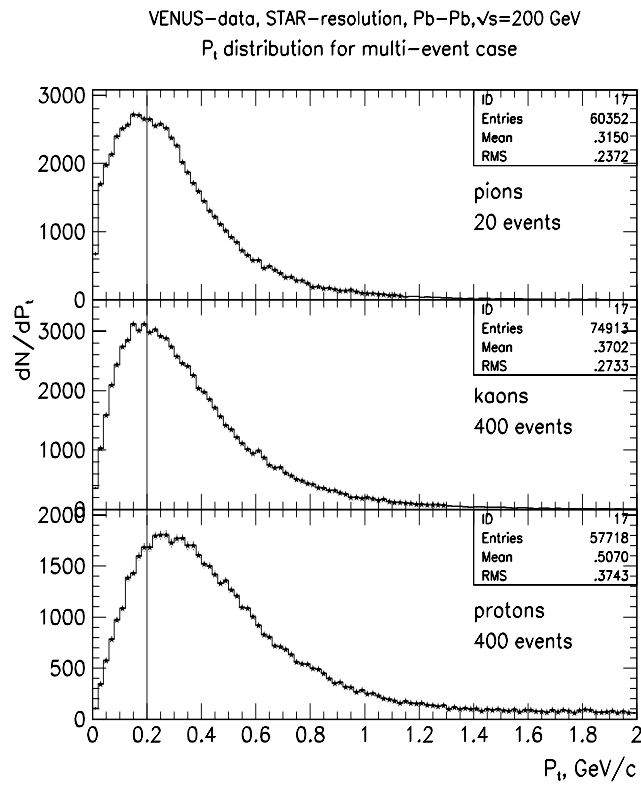


**Figure 9:** Transverse momentum ( $p_t$ ) distributions for pions, kaons and protons predicted by VENUS.

### 1.3.4 Identical-pion correlations

The correlation function for the pairs of positive pions registered by the SVT+SSD+TPC detection system is presented in the Fig.10a. In this - and in the subsequent figures - some characteristic curves demonstrate different features important for the correlation analysis. The correlation effect inferring from the quantum statistics alone is indicated by the full squares. As the quantum-statistical correlations of the charged particles are always accompanied by the effects of Coulomb interaction the stars show the correlation function corrected by the so called "Gamow factor". The form of that factor is also shown in the figure. The result of the complete calculation including the description of the strong and Coulomb final state interactions and quantum statistics effects is presented by the full circles. It should be stressed that usually this form of correlation function is expected to be observed experimentally. The open circles present the results of the complete calculations taking into account the resolution of the STAR detector as described above. Note also that the presented two-pion correlation functions were constructed for a single generated event.

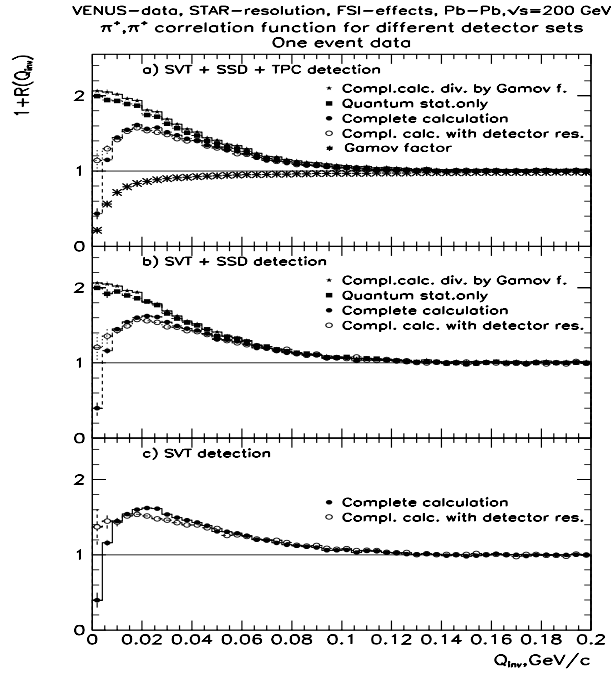


**Figure 10:** Simulated one-event correlation function for two identical charged pions without (full circles) and with (open circles) the effect of experimental resolution. The parts a), b), c) corresponds to different configuration of the detection system considered as explained in the figure. See text for the description of the other displayed curves.

In the case of pions and for relatively small sizes of the emission region the Gamow correction only slightly overestimates the expected form of the correlation function

resulting from quantum statistics. This overestimation, being of the order of the ratio of the relative distance between the emission points in the two-pion rest frame to the Bohr radius of the two-pion system, is small due to a large value (388 fm) of the latter. The correlation function which can be observed (complete calculation - full or open circles) differs strongly, however, from that expected by Bose-Einstein statistics alone. The effects of experimental resolution diminish slightly the maximum and are most important for the smallest values of the four-momentum differences.

Fig.10b presents the same features but for slow pions with the values of  $p_t$  limited to the region of the SVT and SSD detection ( $0.05 < p_t < 0.20$ ) $GeV/c$ . The similar form of the correlation functions in Figs. 10a and 10b indicates that the sizes of the emission region of slow pions do not differ significantly (in the VENUS simulation) from those emitted in the whole  $p_t$  interval. Also the single-event statistics of pion pairs seems to be sufficient for the interferometry analysis. The resolution effects for slow pions are, however, slightly stronger.

The correlation functions corresponding to the pion detection by the SVT only are presented in the Fig.10c. The influence of the detector resolution is strongest here (see open circles) making almost invisible the minimum at the smallest values of  $Q_{inv}$  which should appear due to the Coulomb repulsion effects (full circles).

The analogous set of results have been obtained for the space-time distributions of emitted pions multiplied by the scale factor  $\alpha = 3.0$  (Fig.11). In this case the mean value of the CMS size of pion emission region is about 17fm. It can be considered as an extreme value of the pion source dimensions. The correlation effect seen in the Fig.11a is limited to the significantly narrower interval of  $Q_{inv}$ . The Gamow correction is clearly not applicable here. The experimental resolution diminishes considerably the observed correlation maximum.

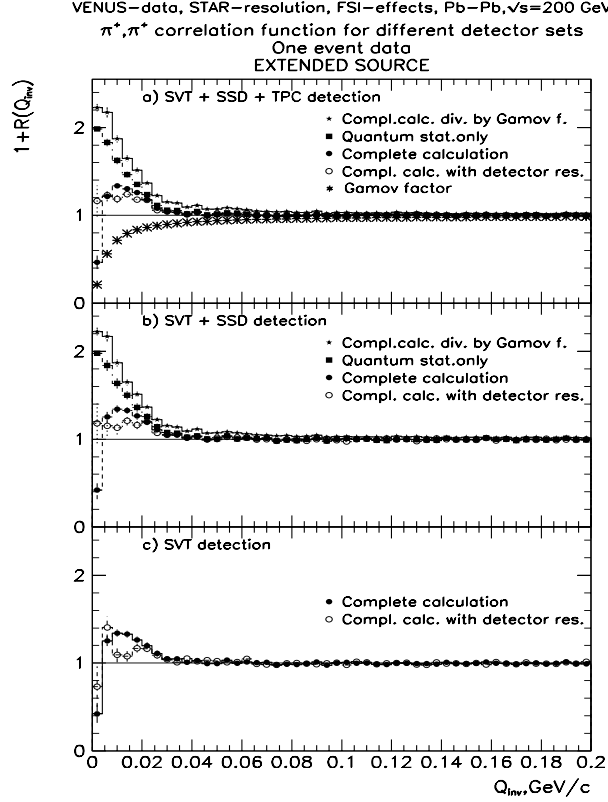


**Figure 11:** Same as Fig.10 but for the enlarged space-time emission characteristics by the scale coefficient:  $\alpha = 3.0$ .

Figs.11b and 11c provide estimate of the STAR detector capabilities to analyze the correlation effects for slow pions. In both cases the form of the correlation function is strongly affected by the resolution effects. It seems that the distortions observed in the case of detection by the SVT alone can hardly be corrected for a significant influence of the systematic errors. This result thus indicates a possible limit of the one-event pion interferometry analysis with the STAR detector.

### 1.3.5 Correlations of identical kaons

The sizes of kaon emission region, as generated using the VENUS model, are not essentially different from those of pions. The quantum statistical effect is therefore similar. However, the shape of the correlation function obtained with the complete calculations is quite different, mainly due to the different Coulomb final state interaction. Since the two-kaon Bohr radius is by a factor of 3.5 smaller than the two-pion one, the Coulomb suppression region at small  $Q_{inv}$  is increased by about the same factor. For the same reason the Gamow factor cannot be used to correct the observed correlation functions.

The analysis of correlation effects for kaons has been made in the same way as for pions. In Fig.12 the analogous correlation functions obtained with the scale factor  $\alpha = 1.0$  are presented. The Gamow factor correction overestimates the correlation effects due to quantum statistics in the whole range of  $Q_{inv}$  displayed in the figure. The influence of the detector resolution is more pronounced than for pions which is related to a wider Coulomb suppression region in the former case. In the case of limited transverse momenta (Fig.12b and 12c) the shape of correlation functions is more strongly affected by the resolution effects. For the detection by the SVT alone the Coulomb dip at low  $Q_{inv}$  in the correlation function, is almost completely filled in due to the resolution effects.

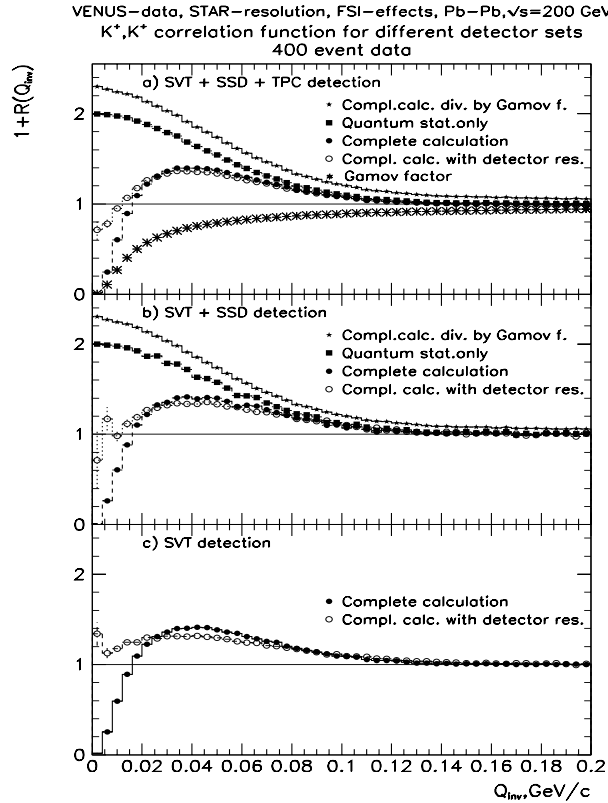


**Figure 12:** Simulated correlation function for two identical charged kaons without (full circles) and with (open circles) the effect of experimental resolution. The parts a), b), c) correspond to different configurations of the detection system considered as explained in the figure. See text for the description of the curves displayed in the figure.

For the scale factor  $\alpha = 3.0$  (Fig.13) the narrow effect of Bose statistics is practically cancelled by the effect of Coulomb interaction. The Gamow correction fails completely. The influence of the detector resolution is important even in the case of

particles registered by the whole detection system. For the small kaon momenta the correlation effect is hardly visible in the case of SVT+SSD detection and practically disappears if only the SVT is used.

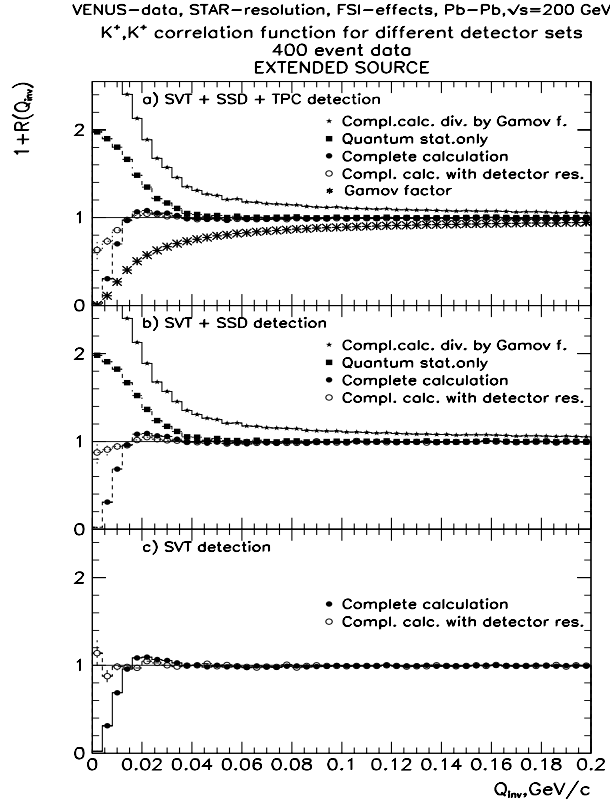


**Figure 13:** Same as Fig.12 but for the enlarged space-time emission characteristics by the scale factor:  $\alpha = 3.0$ .

### 1.3.6 Two-proton correlations

Correlations of two-fermions, represented here by two protons, are shown in Fig.14. The characteristic features are analyzed in the same way as for pions and kaons. The quantum-statistical correlation effect is negative in this case, the corresponding correlation function reaching the value of 0.5 at  $Q_{inv} = 0$ . The Gamow correction is, of course, not applicable as the Bohr radius for the system of two protons is relatively small, about 57 fm, and the correlation effect for small effective sizes is mainly determined by the strong interaction.

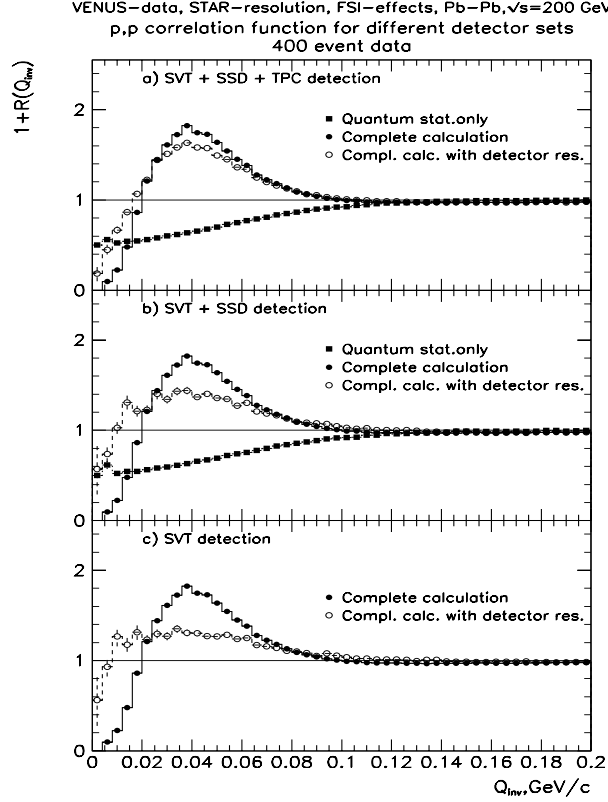


**Figure 14:** Simulated correlation function for two protons without (full circles) and with (open circles) the effect of experimental resolution. The parts a), b), c) correspond to different configurations of the detection system considered as explained in the figure. See text for the description of other displayed curves.

For the value of the scale factor,  $\alpha = 1.0$ , the correlation effect for the complete calculation has the form of a broad peak with the maximum at about 40 MeV. It is the joint result of positive correlations due to the strong interaction and negative ones resulting from Coulomb and quantum-statistical effects. The influence of experimental resolution is rather large changing strongly the shape of the correlation function due to even wider Coulomb suppression region than in the two-pion case and the presence of the strong interaction peak.

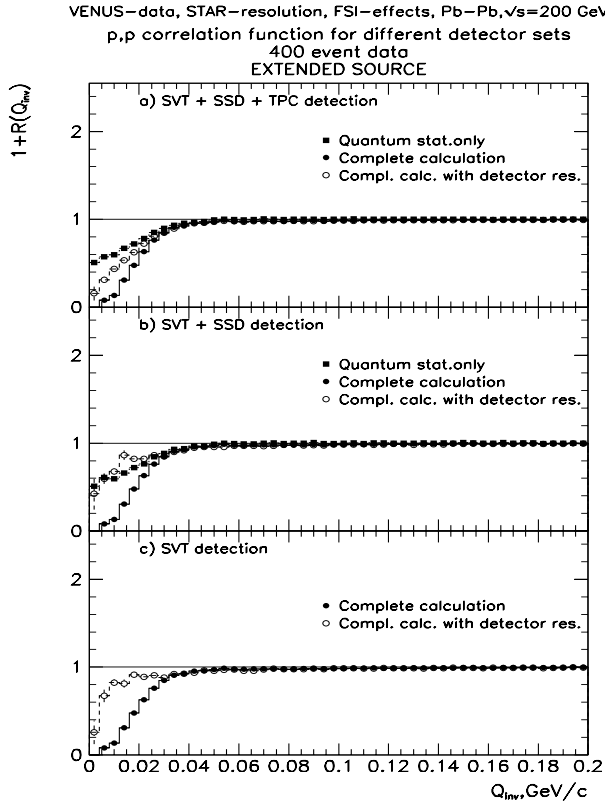


**Figure 15:** Same as Fig.14 but for the enlarged space-time emission characteristics by the scale coefficient:  $\alpha = 3.0$ .

In the case of  $\alpha = 3.0$  (Fig.15) the form of the complete correlation function changes completely. The peak converts into dip for the smallest  $Q_{inv}$  values. It demonstrates the great sensibility of the two-proton correlation function to the space-time characteristics of the proton emission region. However, the influence of experimental resolution fill up the narrow effect of negative correlations. The relatively small number of emitted protons precludes the possibility to analyze the proton-proton correlations in single events.

### 1.3.7 Non-identical particle correlations

As mentioned above, the non-identical particle correlations carry information about the sequence of particle emission. In order to verify it, we consider here  $K^+K^-$  pairs and introduce various shifts in their emission times:  $\langle \Delta t \rangle = 10, 0, -5 fm$  (see the corresponding rows in Fig. 16). The first column in Fig. 16 shows the emission time distributions for positive and negative kaons. The second column presents the correlation functions for two different orientations of the vector of relative momentum with respect to the direction of the CMS kaon-pair velocity. The third column

displays the ratio of the correlation functions from the second column. Despite the small differences in the form of correlation functions, their ratio shows the clear effect scaling with  $\langle \Delta t \rangle$  (including the sign) and thus indicating the sensitivity to the order of particle emission on the level of a few fm/c.

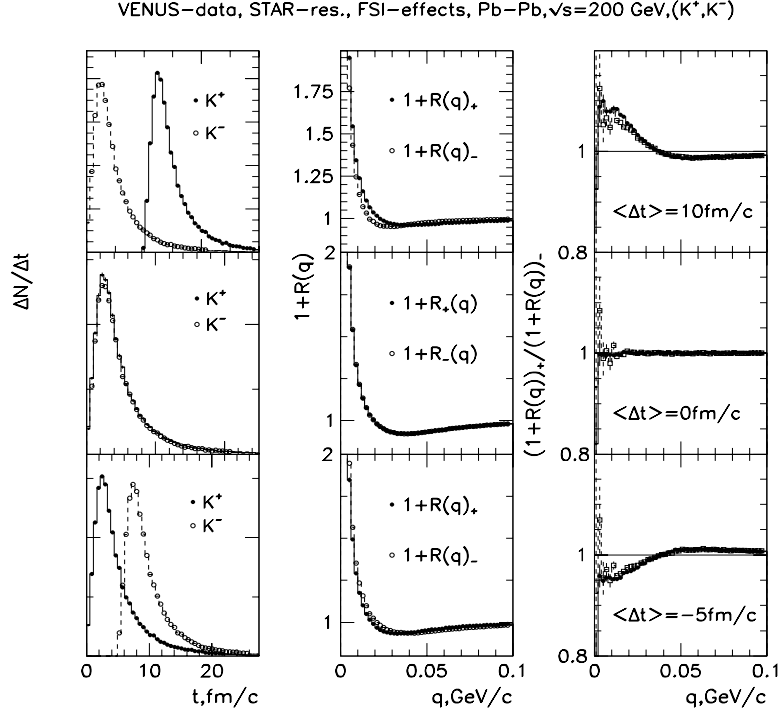


**Figure 16:** Left: distribution of  $K^+$  and  $K^-$  emission times (simulated by VENUS) with  $\langle \Delta t \rangle = +10, 0$  and  $-5$  fm/c introduced ad hoc. Middle and right corresponding correlation functions  $R_+$  and  $R_-$  and their ratios.

The possibility to observe the sequence of particle emission with the STAR for three detector configurations are demonstrated in Fig.17. In the case of the total detection chain: SVT+SSD+TPC ( $0.05 \text{ GeV}/c < p_t < 2.5 \text{ GeV}/c$ ) the sequence of particle emission can be observed. In the cases without the TPC ( $p_t < 0.2 \text{ GeV}/c$ ) the effect is strongly affected by the resolution what precludes practically from extraction of the physical information in the case of large space-time intervals of the particle emission. Here we approach clearly the limits of the detector possibilities.

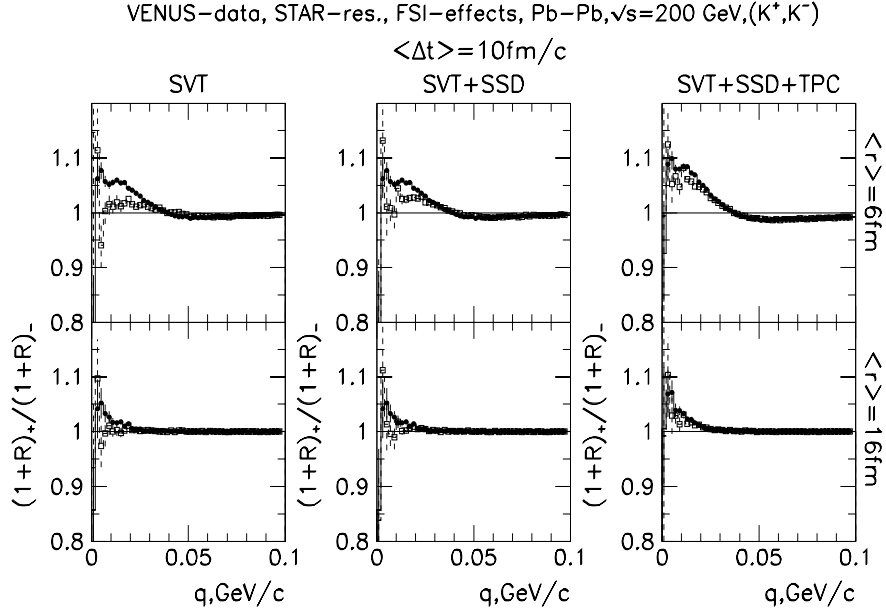


**Figure 17:** Up: ratios of  $R_+$  and  $R_-$  correlation functions for ( $K^+, K^-$ ) pairs with time difference between  $K^+$  and  $K^-$  emission equal  $+10 \text{ fm}/c$  (simulated with VENUS) for SVT, SVT+SSD and SVT+SSD+TPC resolutions respectively. Space-time freeze-out coordinates:  $\langle r \rangle \sim 6 \text{ fm}$  and  $\langle t \rangle \sim 6 \text{ fm}/c$ . Bottom: same as above, but with modified space-time freeze-out coordinates:  $\langle r \rangle \sim 17 \text{ fm}$  and  $\langle t \rangle \sim 17 \text{ fm}/c$ .

### 1.3.8 Correlations of short-lived particles

Neutral kaon interferometry is possible in STAR due to the short-lived particle reconstruction capabilities of the vertex detector. The original SVT simulations showed that on average 2.5  $K_s^0$  (2.5 pairs) will be reconstructed per event. With the reconstruction efficiency enhancement obtained with the SSD, around 9  $K_s^0$  (more than 30 pairs) should be expected. This corresponds to a strong increase, by a factor of 10, of the pair detection rate and consequently a decrease by the same magnitude of the running time necessary to collect a  $K_s^0$  pair sample statistically significant.

It is demonstrated that the strong improvement of the  $\Lambda$  reconstruction efficiency obtained by the addition of the SSD opens the possibility of measuring  $\Lambda$  pairs in an event. Before the inclusion of the SSD, the SVT efficiency leads to about 0.5 reconstructed  $\Lambda$  per event. In the preceding section we show that the SSD will enhance the  $\Lambda$  yield per event by about a factor five. The number of reconstructed  $\Lambda$  pairs is then comparable to the number of  $K^0$ -pairs

### 1.3.9 Conclusions

The analysis of the light-particle correlations provides very sensitive test of the quality of the resolution of any multiparticle detection system. In the case of the STAR detector the high precision of the TPC is, in general, sufficient to determine the form of one-dimensional correlation function for different particle species. The problem emerges if one selects the region of small  $p_t$ , and especially if the sizes of particle emission region appear to be large. In this case the correlation effect, which is narrow and negative for like-sign charged particles, is modified by the effects of limited resolution. Keeping in mind that the region of small  $p_t$  and smallest relative momenta is the most interesting as a potential source of the information about the new phenomena (like QGP phase transition, strangeness distillation or Bose-Einstein condensation), it seems very desirable to improve the detection capabilities. The addition of the SSD significantly improves the momentum resolution of the SVT/SSD combination in a stand-alone mode.

Correlations of short-lived particles can be measured at STAR due to the tracking capabilities of the vertex detectors. The addition of the SSD will significantly improves the quality of interferometry analysis of kaons and open a completely new possibility of measuring  $\Lambda$  pairs in an event.

### 1.4 Search for exotic forms of strange matter with STAR

The STAR detector [32] is aimed at analyzing different signals, characteristic of the quark-gluon plasma (QGP) formation, from observables measured in the mid rapidity region. As such it is not devised, in first place, to study extreme forms of objects strongly charged in strangeness like *Strangelets* or *Memo's*. Furthermore, the search for this exotic strange matter has not been successful up to now even with quite dedicated instruments [33] so expressing the difficulty of the task. Beside, the mid rapidity region is not ideal for discovering this exotic matter because the baryonic chemical potential  $\mu_B$  is expected to be close to zero and will hinder the distillation process governing the strangelet formation. RHIC will, however, provide much higher temperature, energy density, and longer lifetime for the expected plasma formation than any values reached up to now. Furthermore, recent theoretical speculations [34] suggest that  $\mu_B$  should be different from zero and should allow the distillation process to take place. The reason for possible exotic strange matter formation is due to 1) fluctuations in the stopping power providing finite value of  $\mu_B$  in a small fraction of all events. 2) fluctuations of the net-baryon and net-strangeness content between different rapidity bins within any one event. Furthermore, the increasing number of  $s\bar{s}$  quark pairs should, to some extend, counter balance the low initial baryonic chemical potential. This might create preferentially light objects which should be easier to detect. 3) strange (anti)baryon enhancement due to collective effects like chiral phase transition. Then, coalescence may generate Memo production.

Among its attractive features STAR is able to deal with large multiplicities of

particles in an open geometry. As a result, it is legitimate to wonder whether this detector may permit the measurement of exotic forms of strange matter emitted at very low rate. This would offer a complementary approach to those of the experiments specifically addressing this quest on other experimental sites. Notice, by the way, that no experiments dedicated to exotic strangeness are presently proposed at RHIC. Hence, it is worth speculating on the detection ability of exotic strange objects with STAR. We have addressed this question by running some calculations and simulations to estimate the sensitivity of STAR to the detection of strange objects of different lifetimes : stable or long-lived ( $\tau \geq 10^{-7} s$ ), short-lived ( $10^{-11} s \leq \tau \leq 10^{-7} s$ ) and unstable. As for strangelets and Memo's the detection sensitivity is by very far the decisive quantity, we have focused the present simulation on it and not on all the detailed improvements brought by the SSD layer added up to the SVT. The most effective contribution of this latter is, in the present context, to the tracking and to the primary(secondary) vertex reconstruction. Of course, these aspects contribute to the sensitivity but by factors while the basic sensitivity is a matter of orders of magnitude.

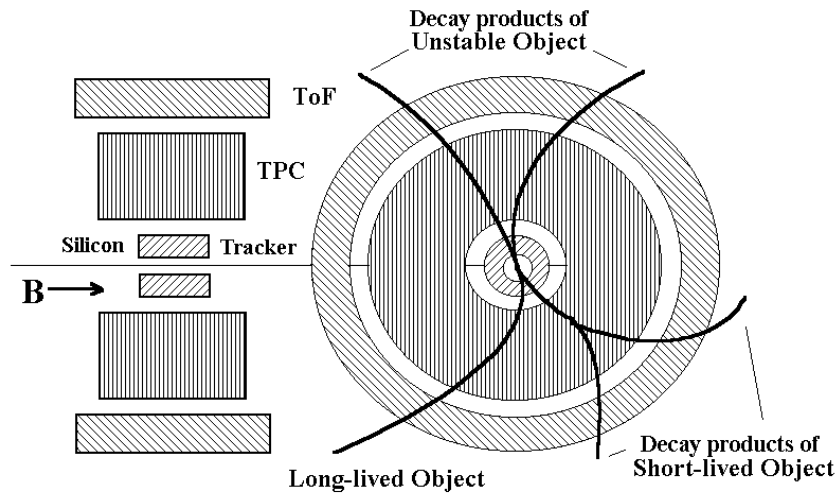


**Figure 18:** Longitudinal and transverse sketches of the central part of the STAR detector. Typical track and vertex patterns of objects of different lifetimes are shown.

As sketched in Fig.18, the footprint of a stable or long-lived object will be a single track across the whole detector volume. As a result the TPC should provide the leading information while the SVT confirms that the measured objects originate indeed from the primary vertex. A short-lived object will decay in flight and should be recognized from track and secondary vertex reconstruction as well as specific decay patterns with the SVT and the TPC. Secondary vertices from unstable-object decay being indiscernible from the primary vertex, the identification should be based on the correlation of decay products. Here again the information extracted from the SVT will be of decisive importance.

## 1.4.1 Detection ability of exotic strange object in STAR

### 1.4.1.1 Long-lived objects

Firstly, assumptions have to be made about the characteristics of the objects under investigation. For this we rely here upon the very recent work of Schaffner et al [35]. This work, although primarily applicable to AGS energy, is one of the very few documented theoretical studies specifically oriented toward the detection of exotic strange objects at large heavy-ion colliders. It is suggested in this work that such extreme forms of strange matter should preferentially extend from the triple magic strangelet ( $6u6d6s$ ) to baryonic masses as high as 16 and with negative charge  $Z$ . The most promising candidates could be  $A_B = 10(Z = -4)$ ,  $12(-6)$  and  $16(-6)$ . However, simple coalescence estimates [35, 36] yield production probabilities of strange clusters of the order of  $10^{3-A_B-|S|}$ . Then large baryonic masses and strangeness values  $S$  reduce rapidly the production probability. As a result, in this study, we have considered the case of an object with  $A_B = 7$  and  $Z = -1$ . However, it should be kept in mind that other assumptions on  $A$  and  $Z$ , relatively close to this latter, will yield quite modest differences in sensitivity. It is also pretty comparable to the assumption  $A=6$  frequently made in several recent works [37].

As this object is assumed to have a lifetime  $\tau \geq 10^{-7}s$ , it will traverse the whole detector. As a result the TPC appears as the most important component to identify and analyze the track of an exotic object and to evaluate the corresponding STAR sensitivity. The implicit relevance of the SVT + SSD ensemble in the tracking extension downward to the primary vertex is not examined here. In Fig. 19 is shown the differential energy loss  $(1/\rho)(dE/dx)$  as a function of the linear momentum per charge unit  $p/Z$ , calculated from the Bethe and Bloch formula, for the  $A_B = 7, Z = -1$  object as well as for other negatively charged particles or clusters, in the case of the STAR TPC. With a current energy resolution of about 7% [36], this object should be resolved from all other products over a large domain of  $p/Z$ . The ToF should, in principle, improve significantly the resolution [36]. However, in the case of very rare events, the background and the non gaussian- distribution tails make its use quite delicate to extract a signal [3, 38]. Although 7% energy-resolution would normally be quite a performing figure, in the present case, it does not guarantee that current "intruding" particles of multiplicity much larger than that of strangelets or Memo's may contribute and distort the distribution of these latter. Indeed, the number of intruders far in the tail of their distribution (several  $\sigma$ 's) on which the searched signal is sitting may be appreciably altered. This effect has been discussed in some detail previously [3, 38, 39].

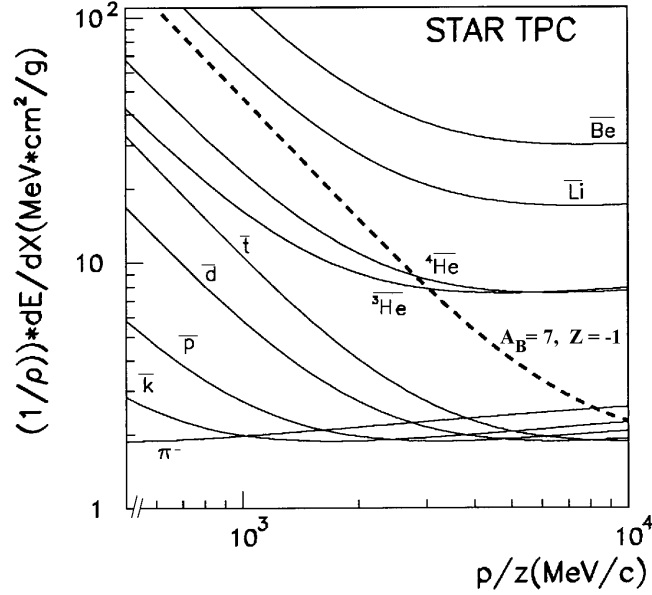


**Figure 19:** Mass stopping power as a function of  $p/Z$  in the TPC of the STAR detector (running 90 %  $Ar$  and 10 %  $CH_4$  for various anti particles and for an object( $A_B = 7, Z = -1$ ))

Thus, it is necessary to evaluate the multiplicities of every possible species  $i$  of intruders. They have been obtained from quantum statistical calculation including a phase transition [40] and from Ref. [3] and [32]. They are reported in the table 4 for  $5 \times 10^7 Au + Au$  events which is the expected number of events analyzed over about 5 years at STAR. From these multiplicities one may calculate, with 99% confidence level, the maximum number ( $n_{max}$ ) of intruders of each species into the exotic object distribution. It is obtained by multiplying the particle multiplicity by the probability of intrusion [38, 39]. The  $n_{max}$  values are shown in Fig. 20 as a function of  $p/Z$ . The total number of intruders is taken as  $N_{max} = \sum_i n_{max}$ . In order to identify a strangelet or a Memo characterized by  $A_B = 7$  and  $Z = -1$ , a minimum number  $N_{min}$  of those has to be produced at such rate that  $N_{min} - N_{max}$  is significantly positive.

Particle	$\pi^-$	$K^-$	$\bar{p}$	$\bar{d}$	$\bar{t}$	${}^3\bar{H}e$	${}^4\bar{H}e$
STAR	$5 \times 10^{10}$	$1.5 \times 10^{10}$	$5 \times 10^9$	$7.5 \times 10^6$	$1.9 \times 10^4$	$1.9 \times 10^4$	65

Table 4: Multiplicities of particles calculated for  $5 \times 10^7 Au + Au$  events.

The difference  $N_{min} - N_{max}$  is plotted in Fig. 21 as a function of  $p/Z$  for different multiplicity assumptions on the production rate of the exotic object. One sees that a long-lived object like  $A_B = 7$  and  $Z = -1$ , emitted at the rate of about one event every  $10^5$  events should be observable [41]. As already stated, this sensitivity is not strongly dependent on the assumed characteristics of the object, but it is very

dependent on the intruding particle multiplicities. A change of one order of magnitude in them might either render the study extremely difficult or establish fairly attractive conditions.

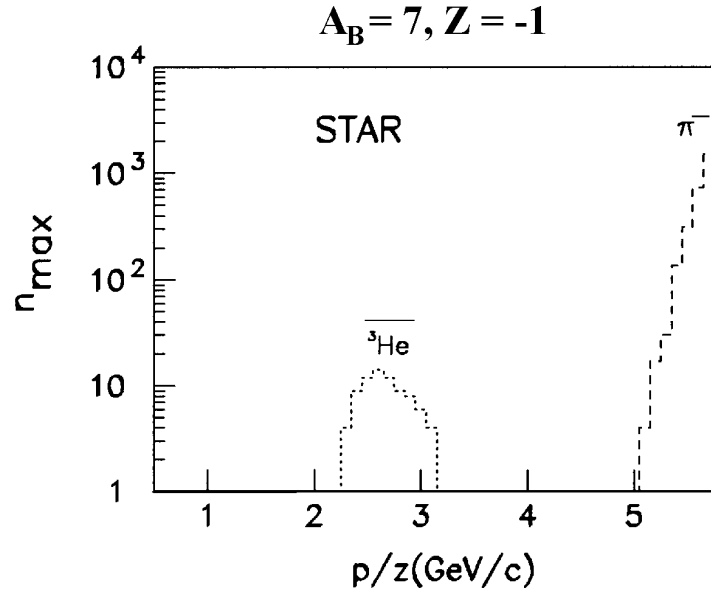


**Figure 20:** Nature and maximum number of particles detected in the TPC of STAR able to alter the long-lived strange object count-distribution as a function of  $p/Z$ .

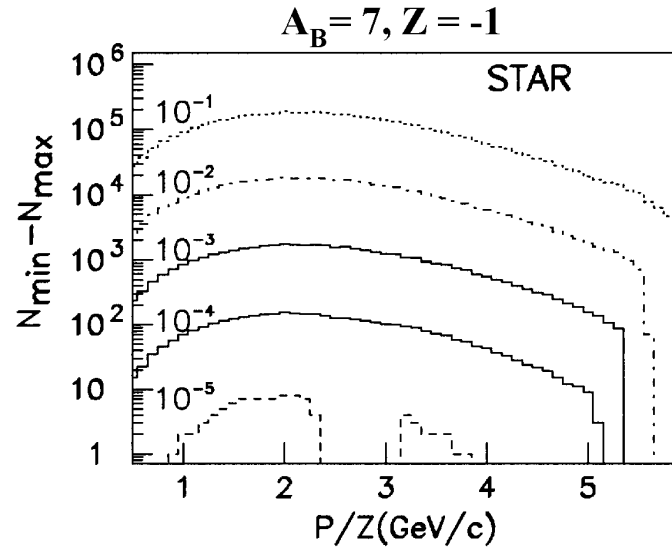


**Figure 21:** Difference between the minimum number of exotic clusters ( $A_B = 7, Z = -1$ ) and the maximum number of contaminating particles as a function of  $p/Z$  for several assumptions ( $10^{-1}$  to  $10^{-5}$ ) on the production rate of this object within  $5 \times 10^7 Au + Au$  events.

### 1.4.1.2 Short-lived objects

Short-lived exotic objects will decay in flight and their observation implies the identification of the decay pattern through track and vertex reconstruction. As a result, the SVT+SSD and the TPC are both very useful. Furthermore, the best conditions resides in the case where the secondary vertices are located in the so-called fiducial volume extending from a few millimeters away from the interaction point up to the first layer of the SVT. The optimal tracking conditions are then established. To illustrate the method, we shall consider the case of the simplest strangelet or Memo, i.e. the H-Dibaryon which can be viewed as  $2u2s2d$  or  $\Lambda^0\Lambda^0$ . In the case of metastability, where it decays via a weak interaction process, two decay channels are possible:

$$\begin{aligned}
 H^0 &\Rightarrow \Sigma^- + p \\
 &\quad \hookrightarrow n + \pi^- \\
 H^0 &\Rightarrow \Lambda^0 + p + \pi^- \\
 &\quad \hookrightarrow p + \pi^-
 \end{aligned}$$

The first mode is difficult to identify because it includes a neutron which cannot be seen in the SVT+SSD+TPC ensemble plus a very short  $\Sigma^-$  track. Thus, we consider the second mode in which the sequential decay leads to the reconstruction of two vertices connecting the tracks of one proton and one  $\pi^-$  (the  $\Lambda^0$  cannot be detected). The decay branching ratio has not been taken into account in the calculation, as it is not known.

In the calculation presented here, a mass of  $2215MeV/c^2$  has been assumed for the  $H^0$ . This latter has to be emitted within the  $-1 \leq y \leq 1$  rapidity domain while all decay products have to be emitted in the  $45^\circ \leq \Theta \leq 135^\circ$  angular acceptance. The secondary vertices have to be in the fiducial volume ( $0.5cm$  and  $6cm$  inner and outer radius, respectively). As a result, the acceptance of the detector is dependent on the lifetime of the  $H^0$ . Energy thresholds of  $300MeV$  for protons and  $80MeV$  for  $\pi^-$ 's have been taken. The acceptance of the STAR detector to H-Dibaryon's with  $\tau = 5 \times 10^{-10}s$  as a function of the rapidity  $y$  and the transverse momentum  $p_t$  is shown in Fig. 22. The integrated acceptance over the complete  $y$  and  $p_t$  domain is shown in Fig. 23 as a function of the  $H^0$  lifetime. One sees that  $\tau \approx 10^{-10}s$  is the most favorable lifetime value because it corresponds to the appropriate time for the secondary vertices well situated in the fiducial volume.

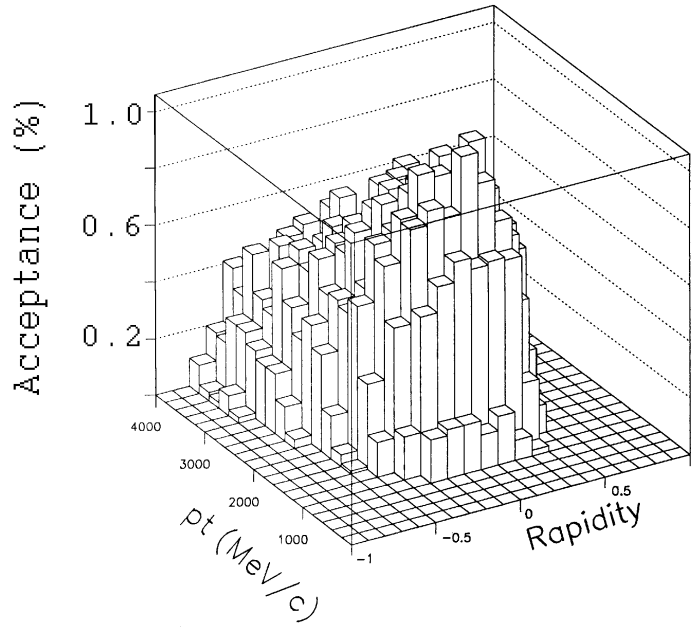


**Figure 22:** Acceptance of the STAR TPC as a function of rapidity and transverse momentum for  $H^0$ .

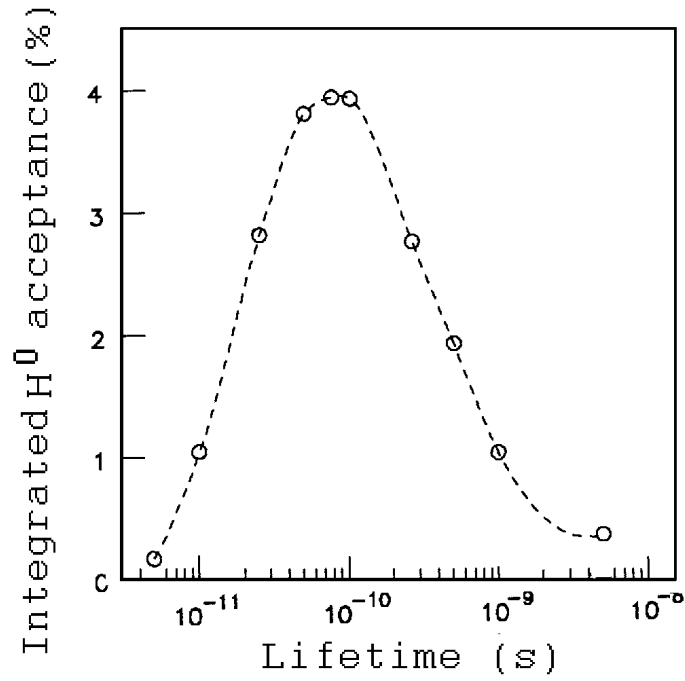


**Figure 23:** Integrated acceptance of the  $H^0$  for STAR as a function of the  $H^0$  lifetime.

The integrated acceptance multiplied by the squared efficiency  $\varepsilon_{eff}$  of  $\Lambda^0$  track and vertex reconstruction (see Table 3) yields the ratio ( $N_{reconstructed}/N_{emitted}$ ) of the number of reconstructed  $H^0$  over the number of emitted in the acceptance. The percentage of reconstructed H-Dibaryon is shown in Fig. 24. One may speculate that the H-Dibaryon may have a lifetime larger than that of the  $\Lambda^0$  which is  $\sim 2.6 \times 10^{-10}s$  since it decays via  $\Lambda^0$  emission. In such a case the percentage of reconstructed  $H^0$  should be less than about  $\sim 0.45\%$  (as compared with  $\sim 0.11\%$  without the SSD layer). In other words, about one  $H^0$  may be reconstructed among 250  $H^0$ 's (1000  $H^0$ 's without the SSD layer) emitted in the STAR detector acceptance [41].

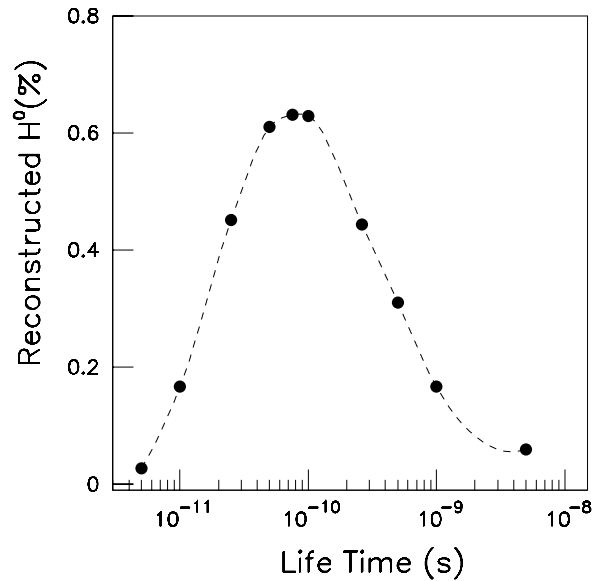


**Figure 24:** Percentage of reconstructed  $H^0$  in STAR as a function of the  $H^0$  lifetime.

#### 1.4.1.3 Unstable objects

This is the case where the exotic strange object decays via strong interaction, i.e. within less than about  $10^{-20}s$ . The secondary vertices are thus indiscernible from the primary vertex and the only possibility to identify such an object is to correlate the decay products within an event. It is certainly the most difficult case. Let us keep the case of the H-Dibaryon, decaying instantaneously into two  $\Lambda^0$ 's. Again, these two  $\Lambda^0$ 's will decay in their turn into a proton and a  $\pi^-$ . They have to be correlated, event by event, via effective mass reconstruction among several other uncorrelated

$\Lambda^0$ 's, these latter yielding quite a large background on top of which the H-Dibaryon signal is sitting.

We have assumed an effective mass ranging from 2300 up to 2500  $MeV/c^2$  for the H-Dibaryon. It has to be larger than twice that of the  $\Lambda^0$ , i.e.  $2 \times 1115 MeV/c^2$ . We suppose that the effective mass distribution is of Gaussian shape whose  $\sigma$  is considered lying between 20 and 60  $MeV/c^2$ . We have generated first a combinatoric background due to all the uncorrelated  $\Lambda^0$ 's within an event. We have assumed that two  $\Lambda^0$  are reconstructed in STAR per event. This figure results from factors corresponding to the decay branching ratio of  $\Lambda^0$ , the fiducial volume, the angular acceptance, the energy thresholds and the track and vertex reconstruction. Considering from simulations that the actual number of detected  $\Lambda^0$ 's in a  $Au + Au$  event, should be of about 2 in the acceptance of STAR, this allows for generating the background whose trend is shown in Fig. 25. On top of this background we have added a Gaussian distribution simulating the  $H^0$  signal with different multiplicities. They are reported in Fig. 25 (grey zones) for a multiplicity of  $10^{-2} H^0$  per  $\Lambda^0$ , i.e. one  $H^0$  emitted every  $10^2$  uncorrelated  $\Lambda^0$ 's, for an effective mass of 2300, 2400 and 2500  $MeV/c^2$  and a  $\sigma = 40 MeV/c^2$ .

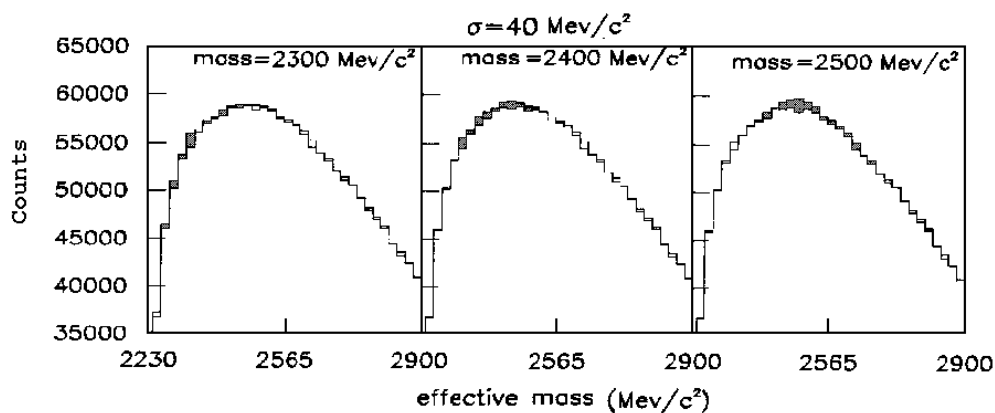


**Figure 25:** Simulated  $H^0$  signal (grey zone) plus combinatoric background for  $5 \times 10^7 Au + Au$  events shown for three different assumptions on the effective mass of  $H^0$ . The  $H^0$  distribution is supposed to be of Gaussian shape with  $\sigma = 40 MeV/c^2$ .

By subtracting the background fitted to the global distribution in the parts way off the signal, one may extract the  $H^0$  signal. Hence, one obtains a  $H^0$  effective mass distribution whose example is given in Fig. 26 for  $5 \times 10^7 Au + Au$  events, with the parameter choice indicated in the figure caption, and a  $H^0$  multiplicity of  $10^{-2}$  per  $\Lambda$  [41]. This latter figure looks as the minimum multiplicity required for a reliable identification of the  $H^0$  signal for STAR.

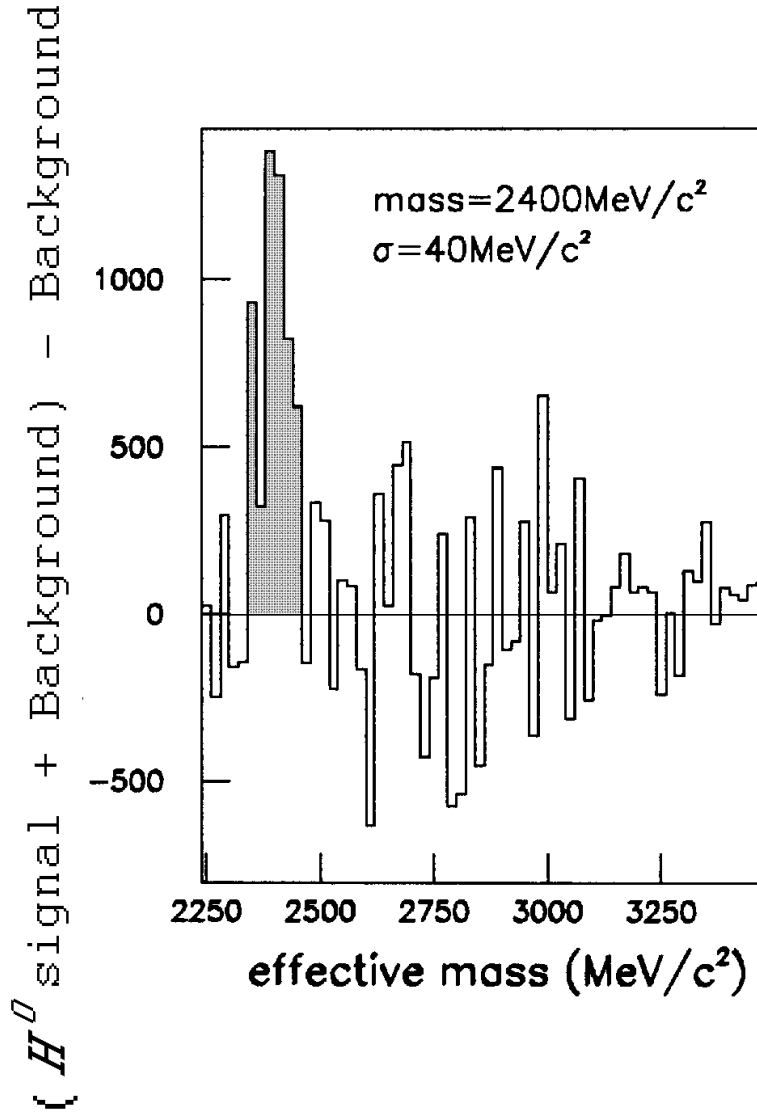


**Figure 26:**  $H^0$  effective mass distribution (grey zone) obtained after background subtraction from simulations performed with the parameter values indicated in the figure.

## 2 Performances of Silicon Microstrip detectors

### 2.1 Detector Response Simulation

Simulations of microstrip detector response have been performed in order to estimate the intrinsic position resolution, the charge matching efficiency, the fraction of ambiguous and overlapping hits with respect to the electronic noise value and the detector geometry. These calculations were based on simulation programs which include the electric field mapping, the electron-hole pair generation with local Landau fluctuations, the migration and collection of charges on strips [42].

#### 2.1.1 Intrinsic spatial resolutions

The position resolution in the direction perpendicular to the strip axis, achievable with the silicon microstrip detector has been calculated for minimum ionizing particles in function of their incidence angle with respect to the detector surface (Fig. 27). For these simulations, a detector thickness of  $300\mu m$ , a pitch of  $100\mu m$  and a signal lower threshold of 3 times the noise value have been assumed. The position resolution improves rapidly with the particle angle which is explained by the rise of the average cluster size. At  $0^\circ$  (normal incidence) the resolution is equal to the digital resolution and determined by the strip pitch. The best resolution is reached for an angle around  $25^\circ$  and becomes worse with increasing angle. The position resolution does not show a strong dependence with the noise value (assumed to be characterized by a Gaussian distribution). Only at high incidence angle the resolution is sensitive to the noise value but nevertheless a very good resolution of the order of  $10\mu m$  can be expected for a conservative noise value of  $800e^-$ . The dependence of the position resolution on the two-particle relative distance have been also investigated (Fig. 28). Both the one-particle and the two-particle resolution get worse at relative distances smaller than 4 times the strip pitch since clusters are more and more overlapping. Below 2 times the pitch the efficiency of finding two clusters falls rapidly to zero. At higher relative distances clusters are completely separated and the two-particle resolution is equal to  $\sqrt{2}$  time the one-track resolution.

In overall, for the detector geometry currently defined, excellent one-particle and two-particle resolutions can be reached respectively better than 25 and  $50\mu m$ .

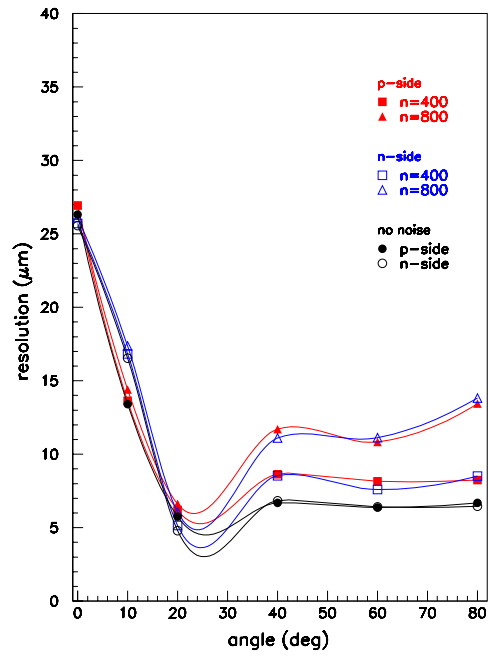


**Figure 27:** Spatial resolution versus the particle incidence angle and the electronic noise.

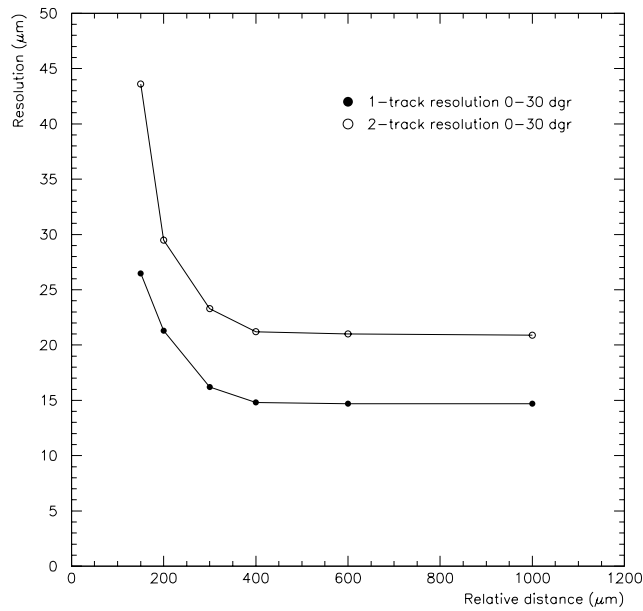


**Figure 28:** One-particle and two-particle spatial resolution versus the relative distance between the two particles.

### 2.1.2 Charge matching efficiency

Since double-sided microstrip detectors are not pure bidirectional detectors, signal from both sides of the detectors have to be correlated to deduce the hit positions in the wafer. Although simple geometrical considerations can be used to match signals for a large fraction of particles, a significant number of hits are ambiguous and lead to several different hit positions. In contrast to two single-sided strip detectors, double-sided detectors are characterized by a unique charge deposition per particle which allows to do a charge matching of signals collected on both p-side and n-side. The charge matching of signals induced by minimum ionizing particle can still be performed with the help of Landau fluctuations, but relies on a very good S/N ratio. The efficiency of the correct matching have been evaluated for different numbers of ambiguous particles and noise values (Fig. 29). For a noise value of  $400e^-$ , the matching efficiencies for pairs, triples and quadruples are better than 85%.

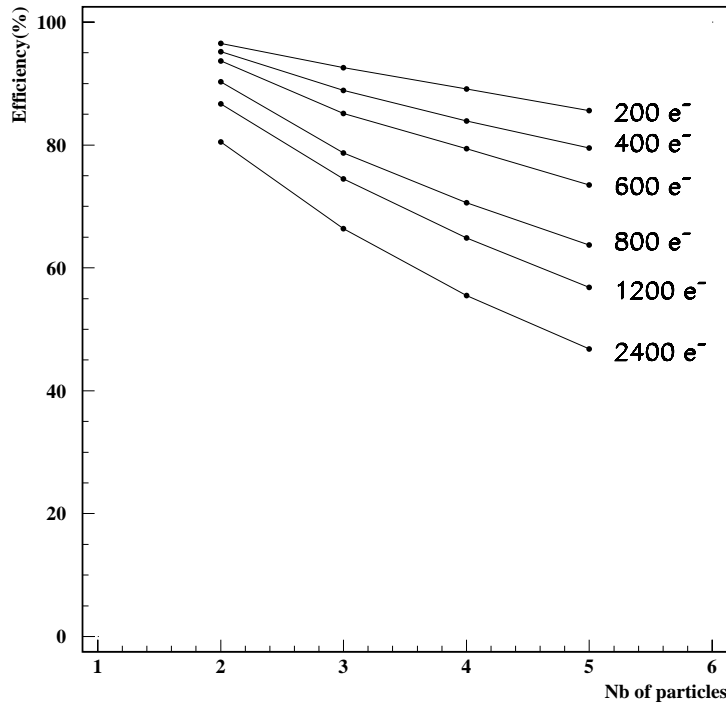


**Figure 29:** Charge matching efficiency versus the number of ambiguous particles and for different values of noise.

### 2.1.3 Number of ambiguous hits, overlapping clusters and resolved particles

The microstrips on both sides of a double-sided detector are not strictly parallel and their direction differs by the so-called stereo angle. The determination of the

stereo angle is a compromise between the spatial resolution required along both axis of the detector, the number of ambiguous hits tolerable (cf. the previous subsection) and technical problems like the location of the bounding pads for the front-end electronics. Monte-Carlo simulations have been performed in order to extract the number of ambiguous hits and reconstructed coordinates in a double-sided strip detector and estimate their dependence on the average particle multiplicity and the detector geometry. The average fraction of ambiguous hits has been found to increase strongly with the particle multiplicity (Fig. 30, upper-left). At a given multiplicity, this number also increases with the stereo angle between the strips of the two sides (at  $90^\circ$  all hits are ambiguous). Part of these ambiguous hits have charge clusters well separated and part of them are characterized by overlapping (partially and totally) clusters. The fraction of ambiguous particles which have overlapping clusters decreases with the stereo angle (Fig. 30, upper-right). In order to calculate the number of resolved particles and consequently the detector hardware efficiency, one has to fold both fractions of hits and to take into account the matching efficiency. By assuming that 50% of overlapping clusters will be lost and for a matching efficiency of 90%, the expected number of resolved particles for multiplicities of 5 and 10 and stereo angle of 35 and 100 mrad are summarized in Table 5:

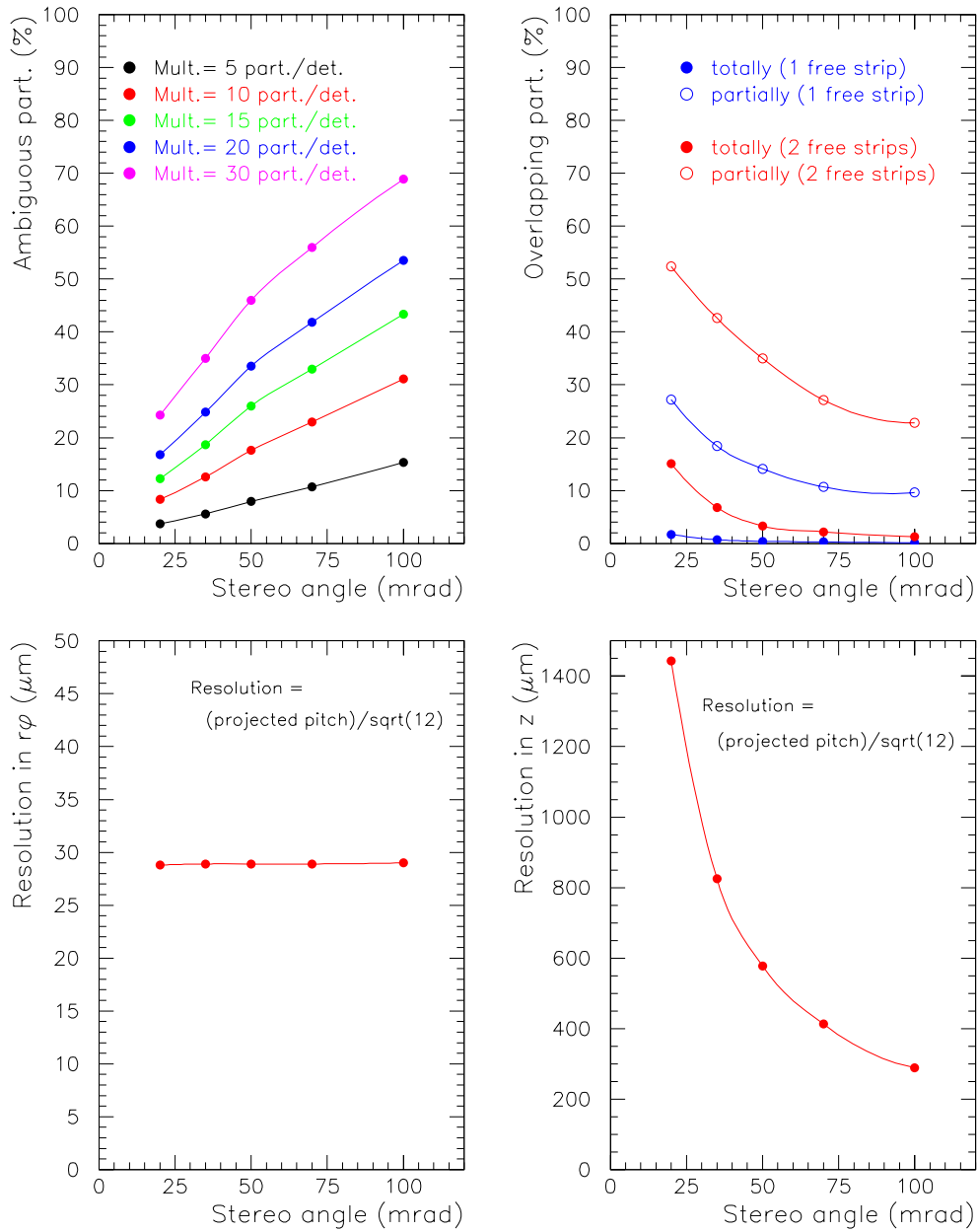
	Multiplicity	
stereo angle	5	10
35 mrad	4.93	9.66
	98.5%	96.6%
100 mrad	4.89	9.47
	97.9%	94.7%

Table 5: Expected number of resolved particles

The overall efficiency is quite good and falls slowly for larger stereo angles. However, by increasing the stereo angle from 35 to 100 mrad the position resolution in the beam direction is improved by a factor 3 (Fig. 30, lower-right) without getting worse resolution in the bending direction (Fig. 30, lower-left). On the other hand the number of strips on the edge which do not reach the readout side of the detector increases from 7 to 21. In the later case, the size of the dead area becomes intolerable and the solution proposed by the CMS collaboration [43] to reroute these strips has to be investigated further.

A detailed simulation code of the silicon microstrip detector response is currently under construction at SUBATECH which would feature the charge generation and collection on strips, cluster merging, cluster finding and cluster matching. The aim of these simulations is to give accurate estimates of the detector efficiency in order to determine the optimum value of the stereo angle. In addition, this simulation package will be further on included in the STAR software packages as a silicon microstrip detector response simulation.

### Ambiguous particles vs Stereo angle



**Figure 30:** Fraction of ambiguous hits, fraction of overlapping clusters, spatial resolutions in the bending plane and the beam direction versus the stereo angle and different particle multiplicity per detector.

## 2.2 Tests of Silicon Microstrip detectors

### 2.2.1 Introduction

We describe here some tests of silicon strip detectors performed to examine their characteristics and performances. This study enters in the framework of R&D activities devoted to the design both of the fourth layer of the STAR detector and of the two outer layers of the ALICE detector. A large part of the R&D is presently accomplished.

### 2.2.2 Single-sided versus double-sided microstrip detectors :

Two kinds of microstrip detectors have been considered: single-sided (SS) and double-sided (DS).

The major interest for choosing DS is that it allows the matching of the charge signals collected on both sides, n and p, thus reducing the ambiguities due to multiple hits. It presents, however, some drawbacks like a more difficult signal readout system.

Both SS and DS detectors have been extensively tested with electron sources and in beam. In particular DS having STAR specifications have been tested, in beam, at the SPS (CERN) quite recently.

### 2.2.3 Tested detectors :

We have tested SS of  $20 \times 20$  mm, with a pitch of  $50 \mu\text{m}$  and  $300 \mu\text{m}$  thick. They had intermediate strips (not connected but readout through capacitive coupling). These detectors were tested by pairs with the possibility of varying the stereo angle between the strips of the two units.

The tested DS was also of  $20 \times 20$  mm with a pitch of  $50 \mu\text{m}$  and  $300 \mu\text{m}$  thick. The stereo angle was of  $90^\circ$ . All these detectors were tested with a  $^{90}\text{Sr}$   $\beta_-$  radioactive source and in beams of 3 and 10 GeV pions from the PS at CERN.

Last May, DS having STAR specification (see section 3.2) and bonded to 128C chips, have been tested in a 125 GeV pion beam.

### 2.2.4 Experimental setups :

The telescope of detectors used at CERN is sketched in Fig. 31. It consists of four pairs of reference detectors ( $iX$  and  $iY$ , with  $i=1$  to 4) and pair of SS's or DS ( $5X$  and  $6Y$ ) to be tested.

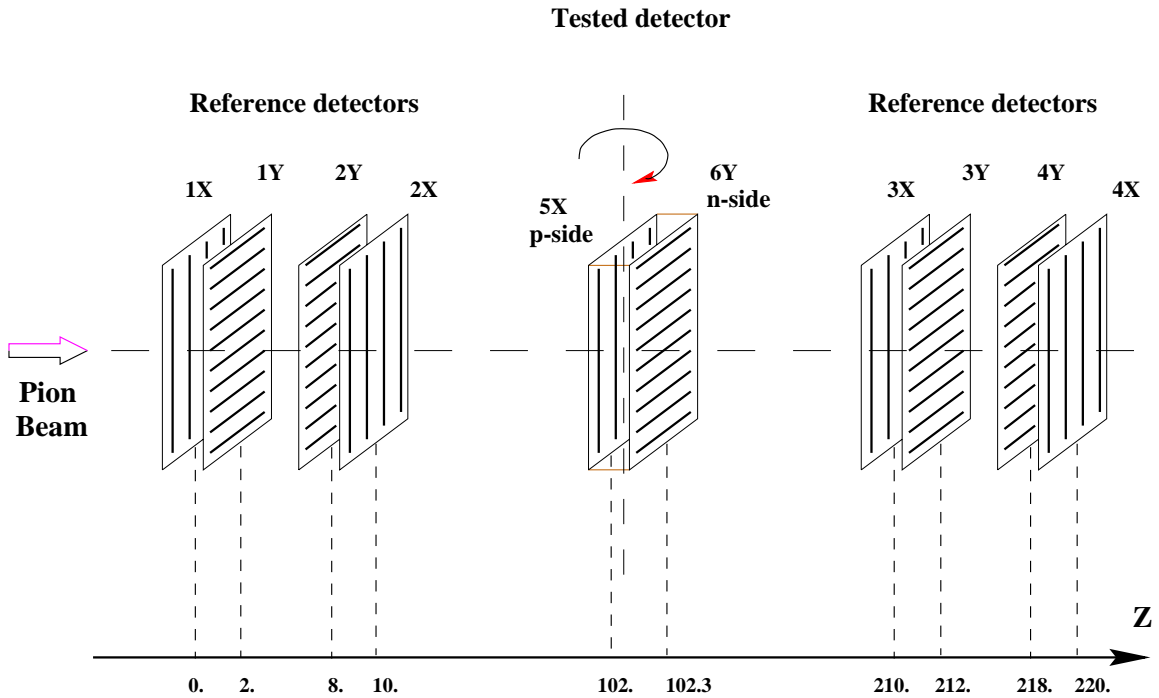


**Figure 31:** Detector telescope used with a pion beam. The relative positions of the different detectors are reported (in  $mm$ ) with respect to the 1X detector, used as the origin.

### 2.2.5 Extraction of the noise and the signal from the raw data :

The collected raw data are the sum of 3 separate contributions: the pedestal, the common mode shift and the pulse-height (signal+noise).

The pulse-height is obtained by subtracting the pedestal and the common mode shift from the raw data.

### 2.2.6 Determination of the mean track positions :

When a particle crosses a detector, it activates a number of strips, those form a “cluster”. Once the clusters are reconstructed for each detector, their centroid determines the impact position of the track in the detector.

A cluster is kept for further analysis if it satisfies selection criteria based on the user’s expertise and experience.

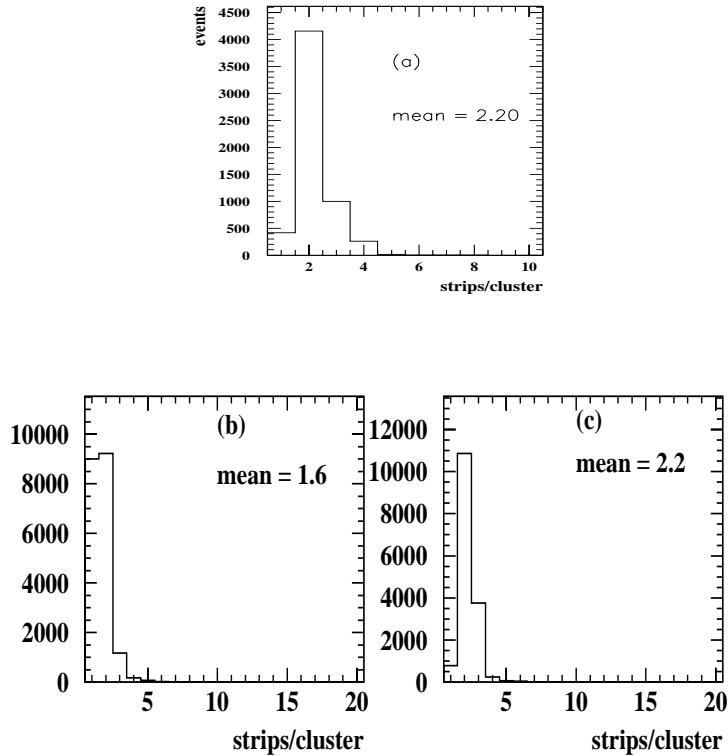
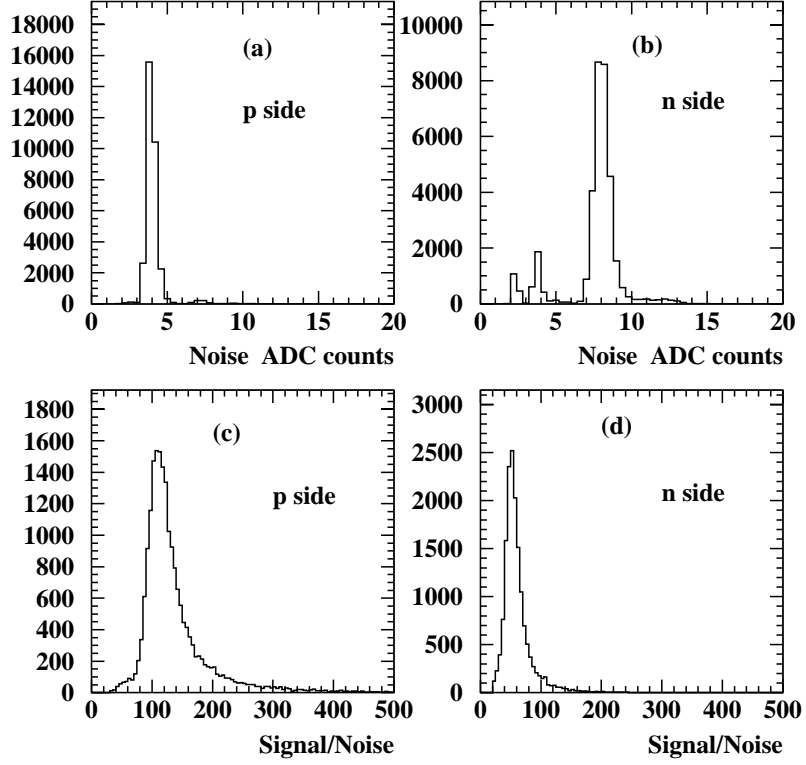


**Figure 32:** Number of strips per cluster using (a) 10 GeV pion beam for SS, (b) 3 GeV pion beam for DS-p side and (c) for the n side.

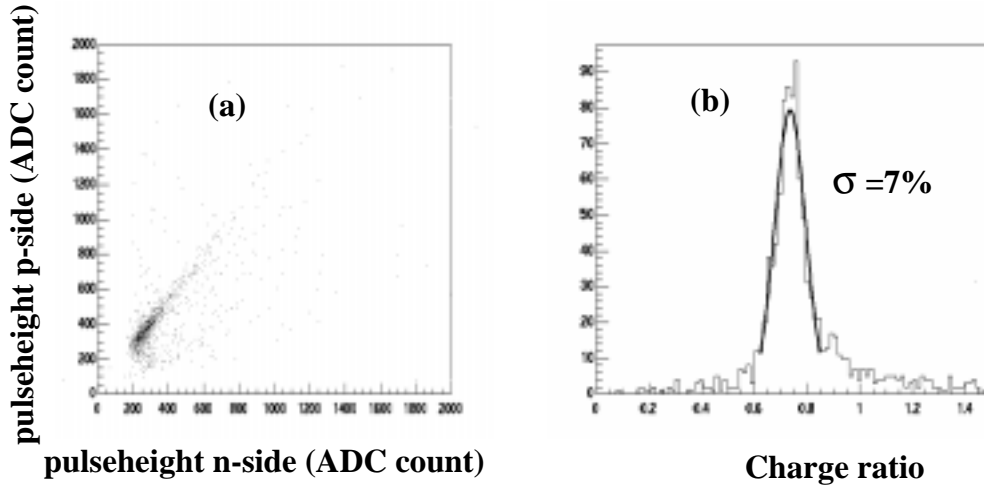
Fig. 32 shows typical distributions of the number of strips per cluster, obtained with a pion beam. The calculated centroids depend on the definition of the cluster selection criteria and are also affected by the contribution of cross-talk between the strips and other electronic components.

Fig. 33 illustrates the cluster signal/noise ratio measured for DS with a 3 GeV pion beam on both sides of the detector. Large ratios are obtained and insure a clean treatment of the data. The signal to noise ratio obtained for the n-side is almost twice as less as for the p-side. This results from the fact that the n-side exhibits a noise roughly double that of the p-side.

Indeed, charge matching has been studied with a DS detector having STAR specification and 128C readout chips. The matching of charges on both side is shown in Fig. 34 as well as the ratio of the charges collected on both sides (n/p). The deviation from the correlation is better than 7%.



**Figure 33:** Distribution of the noise and signal to noise ratio of the reconstructed clusters using a 3 GeV pion beam. (a) noise for p-side, (b) noise for n-side, (c) signal/noise for p-side and (d) signal/noise for n-side of the DS.



**Figure 34:** (a) p-side pulse height versus n-side pulse height for DS. (b) ratio of the pulse heights.

The centroid of the particle impact in the detector may be determined with the variable  $\eta$  which is defined for each pair of strips as:

$$\eta = S_L / (S_L + S_R),$$

where  $S_L$  and  $S_R$  are the signals measured respectively on the left and the right strip of a pair.

The  $\eta$  distributions obtained for a 10 GeV pion beam and electrons from a  $^{90}\text{Sr}$  source are shown in Fig. 35 for SS.

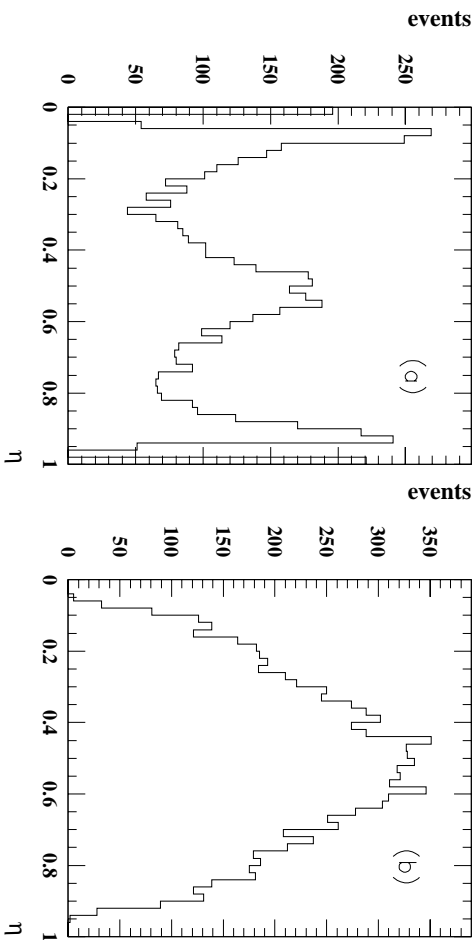


**Figure 35:** Distribution of the  $\eta$  variable (a) for a 10 GeV pion beam and (b) for electrons from a  $^{90}\text{Sr}$  source.

In the case of the pion beam (a), the distribution is characterized by two peaks around the values 0 and 1 and one peak around 0.5 . The first two maxima indicate that one strip collects the majority of the cluster charges. The peak around 0.5 results from the presence of an intermediate strip.

With the  $^{90}\text{Sr}$  source (b), one observes a broad distribution peaking around 0.5, mostly due to multiple scattering of electrons.

### 2.2.7 Spatial resolution :

The estimation of the spatial resolution for detectors requires a software alignment of all detectors with respect to an arbitrary reference detector.

First, a fictive translation of detectors is performed. Then, tracks are determined from a  $\chi^2$  minimization method taking into account the measurements from the reference detectors. Finally, detectors are virtually rotated in order to put all detectors' strips in the same orientation.

The spatial resolution is obtained from the distribution of the difference between the fitted and the measured positions, also called *residual*. The resolution  $\sigma$  is given by:

$$\sigma = \{ \sigma_{resid}^2 - \sigma_{ms}^2 \}^{1/2} ,$$

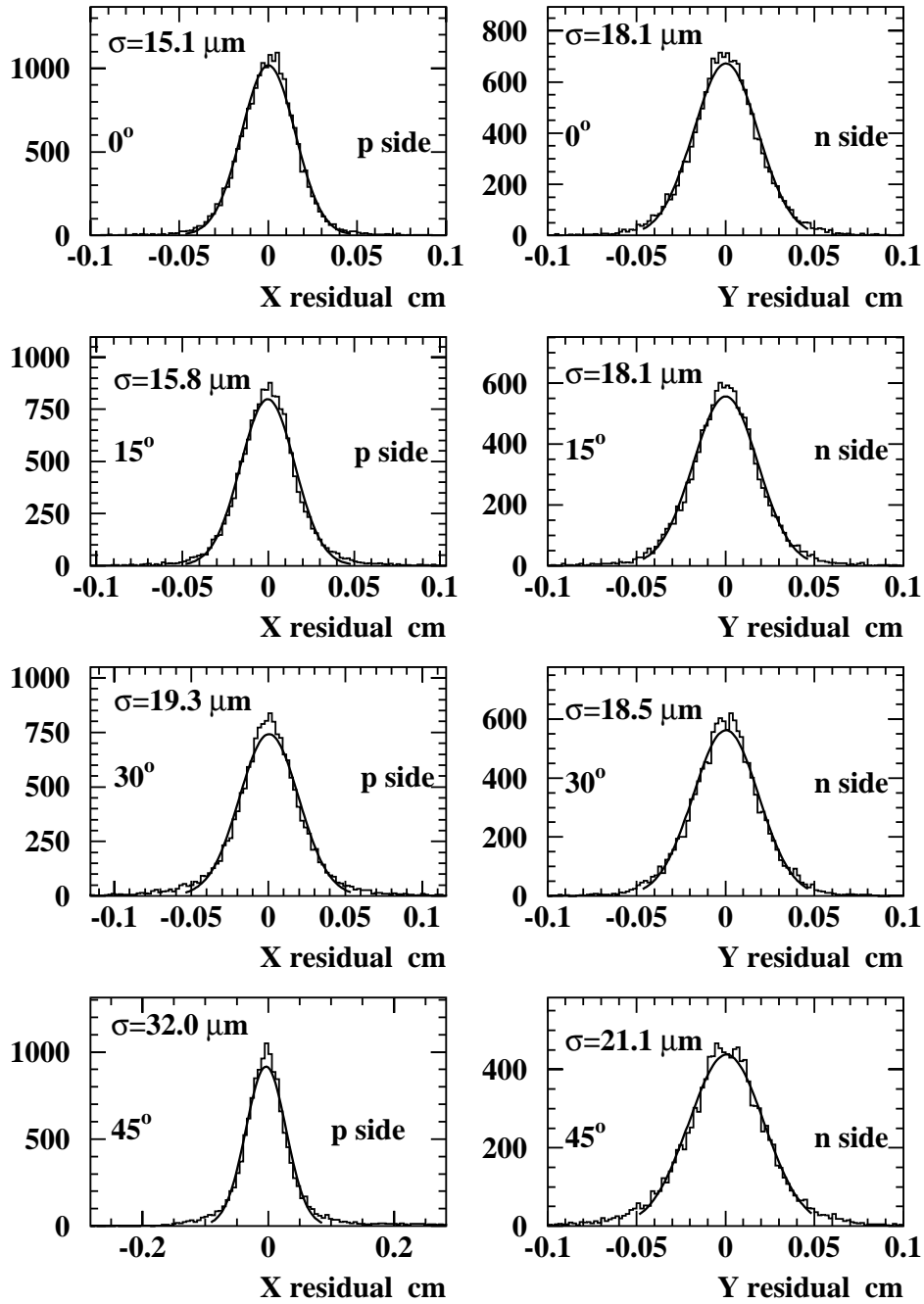
where  $\sigma_{resid}$  is the standard deviation of the Gaussian fitted to the distribution of residuals, and  $\sigma_{ms}$  is the contribution of the multiple scattering.

Fig. 36 shows the  $y$  and  $x$  residual distributions obtained for DS at different beam incident angles with a 3 GeV pion beam. They are fitted with a Gaussian function whose  $\sigma$  value is also reported.

For normal pion incidence, a satisfactory spatial resolution of about  $15\mu\text{m}$  is measured. It extends to about  $32\mu\text{m}$  at  $45^\circ$ .

The contribution of the multiple scattering to the resolution was simulated in the case of a 3 GeV pions and found to be equal to :  $\sigma_{ms}=11 \mu\text{m}$ . It contributes quadratically, with the intrinsic resolution  $\sigma$ , to the  $\sigma_{resid}$  actually measured.

Results have been obtained very recently for the DS's with STAR specification. Due to the high momentum pion beam (125 GeV), the contribution of scattering is negligible :  $\sigma_{ms}=0.3 \mu\text{m}$ . The measured resolution is  $\sigma = 25\mu\text{m}$  at  $0^\circ$  which should be compared to the expected digital resolution of  $27 \mu\text{m}$  for a  $95 \mu\text{m}$  pitch.



36: Distribution of  $x$  and  $y$  residuals of tested DS. Fitting these distributions with a Gaussian function yields the reported spatial resolutions.

### 3. Design of the Silicon Strip Detector

#### 3.1 General characteristics of the SSD (see Figs. 37, 38,39)

The design of the SSD layer is a barrel surrounding the SVT detector. It is equipped by silicon strip detectors positioned on 20 fiber carbon ladders by set of 16 modules per ladder. The centers of the detectors (facing inside) are at a radius of 230 mm from the interaction point. The pseudo-rapidity range covered by 16 modules (active zone) ranges from  $\eta=-1.2$  and  $\eta=+1.2$ . The foreseen detectors are double-sided ones, characterized by a small stereo angle (35 mrad) - see section 3.2.

The SSD mechanical design (section 3.3) is supported by the Subatech group. It has been decided, by both Subatech and STAR collaboration, that the mechanical interface between the TPC and the (SVT+SSD) will be also designed and realized by the French group. This leads up to a new design (section 3.4) of the cones supporting the vertex detector. The aim was both to reduce the amount of matter seen by the collision products and to improve stiffness.

All the electrical part (readout system, slow control, DAQ) is developed by Strasbourg (IReS-LEPSI) and Nantes (sections 3.5 and 3.6). This work follows mainly from the R&D program related to the ALICE experiment. Particularly, a new technology (Tape Automated Bonding) is investigated for the connection of the detectors to the readout electronics.

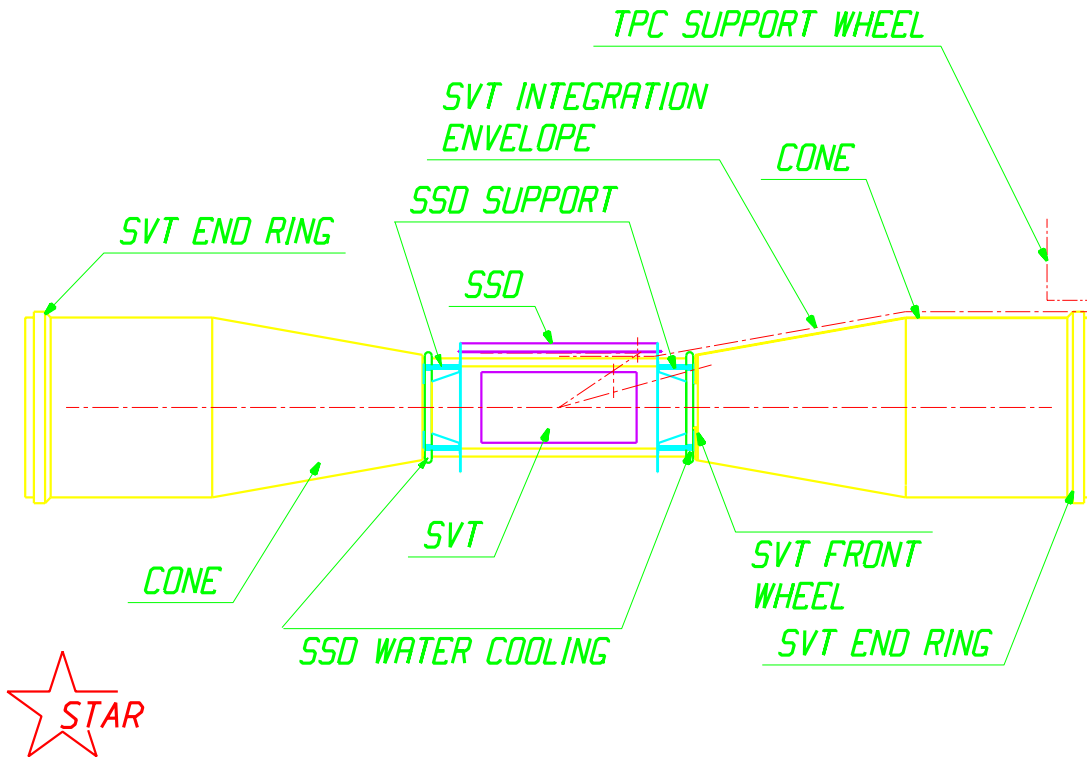


**Figure 37:** Longitudinal view of the mechanical structure.

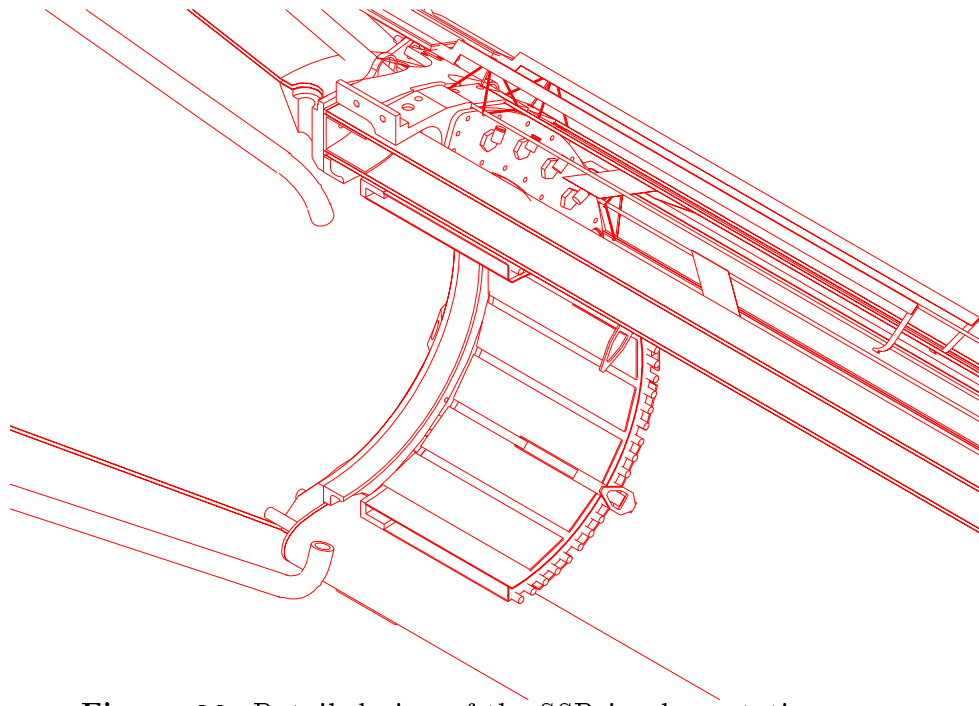


**Figure 38:** Detailed view of the SSD implementation.

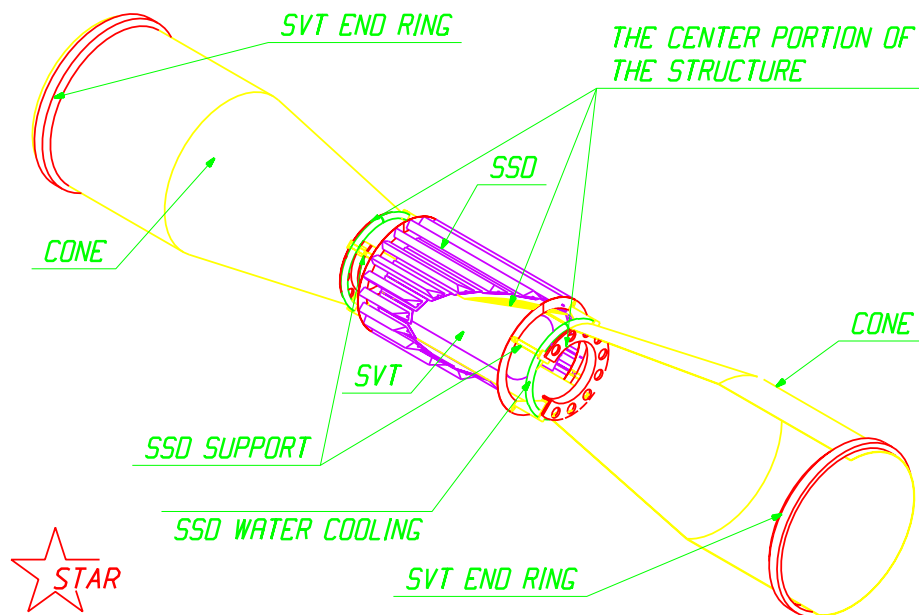


**Figure 39:** 3D-view of the mechanical structure.

### 3.2 Silicon strip detectors

Double-sided detectors are foreseen to equip the SSD layer but two single-sided detectors glued back to back can be used as well without modifications of the masks. For the same total silicon thickness, double-sided detectors provide double gain of the signal amplitudes with respect to single-sided detectors and allow also charge matching. On the other hand, the grounded readout electronics is much easier in the single-sided option than the floating electronics required in the double-sided option. The choice will be also subjected to the overall cost balance.

The general characteristics of the double-sided detectors are listed below (for more details see Appendix A) :

- Expected radiation level: about 1 krad
- Chip size: 75 x 42 mm overall
- Number of strips: 768 on each side
- Length of the strips: about 40 mm
- Bonding pads: double on each end
- Pitch: 95  $\mu\text{m}$ . No floating strips
- Stereo angle: 35 mradian i.e.  $\pm 35/2$  mradian on each side with respect to the edge
- Thickness: 300  $\mu\text{m}$

On Figs. 40 and 41 are shown the Alice/Star detector, respectively P side and N side. The pattern of the bonding pads of the detectors is identical on both sides, whatever the rotation axis is.

The specific following characteristics could be applied in the case of single sided detector option.

- Angle: 35/2 mradian with respect to the reference edge
- Thickness: 150  $\mu\text{m}$

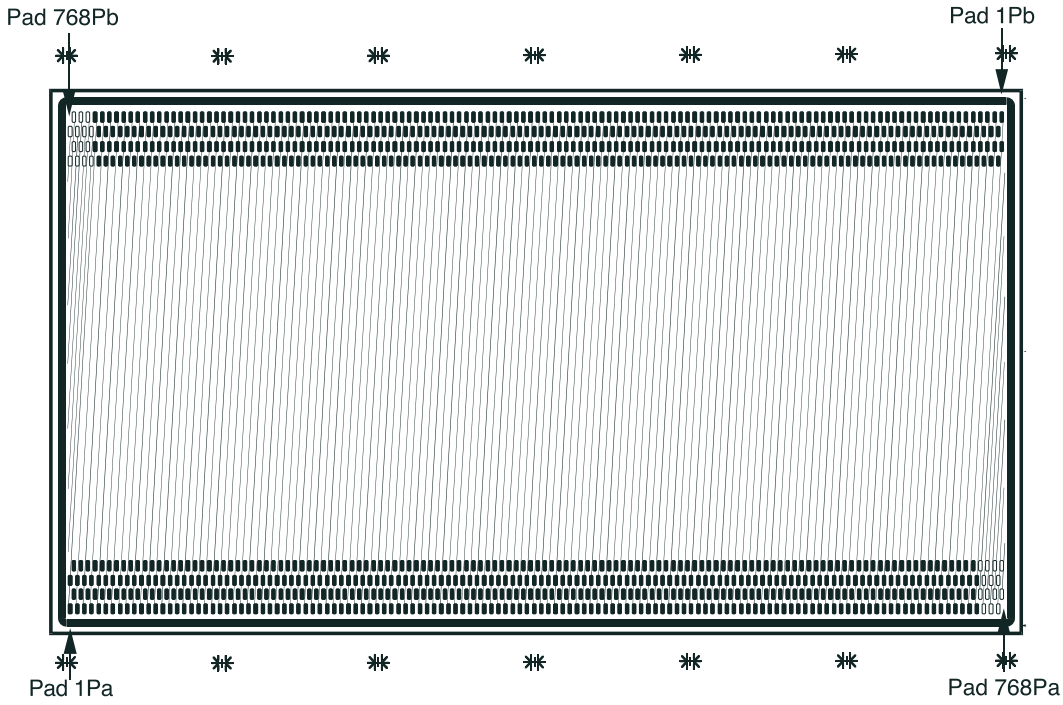


**Figure 40:** Alice/Star detector : side P seen from side P (the general shape is kept but the number of strips is reduced).

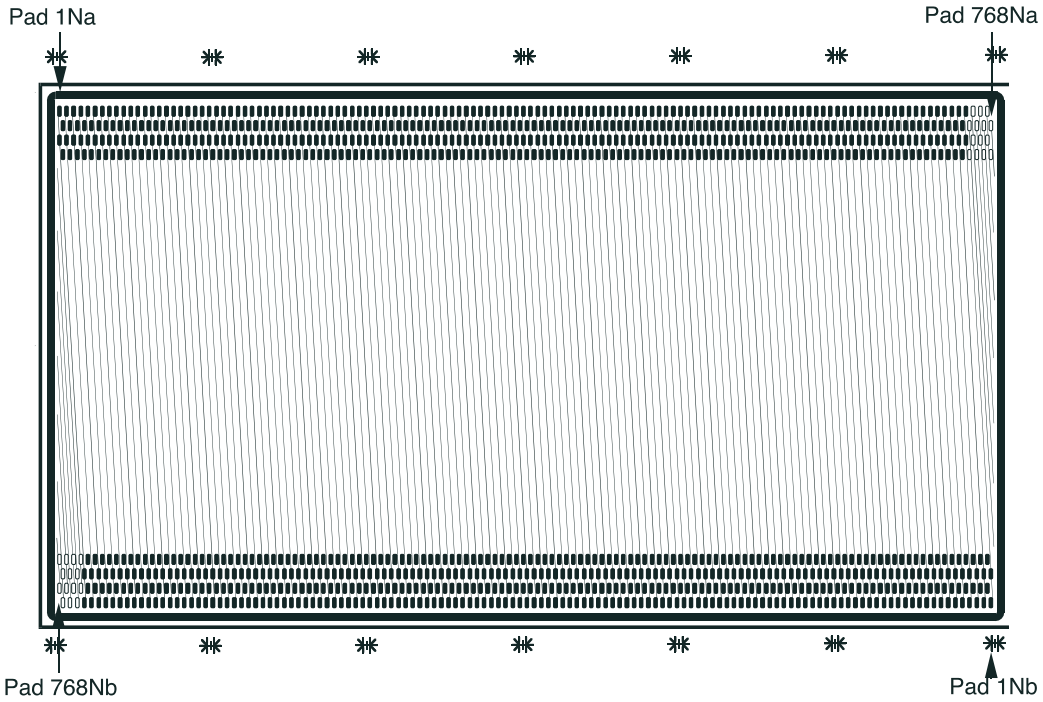


**Figure 41:** Alice/Star detector : side N seen through side P in transparency mode (the general shape is kept but the number of strips is reduced).

### 3.3 SSD mechanics

#### 3.3.1 Mechanical requirements

The mechanical requirements for SSD layer are the following:

- "Clamshell" mechanical design like SVT design.
- Maximum outer diameter  $< \varnothing 580$  mm assuming a safety margin of 170 mm for the TPC field degradation. In present design, maximum outer diameter of SSD  $< \varnothing 555$  mm.
- Minimum inner diameter  $> \varnothing 430$  mm imposed by the connecting elements between the cones.
- Low mass limit per detector layer : average 0.65%  $X_0$ .
- Stability of mechanical structure : structure has to be stable in time within 15  $\mu\text{m}$  ( $\pm 7.5 \mu\text{m}$ ).
- Mechanical defaults of silicon detectors arrays (sag, torsion, planeity) within 30  $\mu\text{m}$  ( $\pm 15 \mu\text{m}$ )
- Alignment : detector to detector within 25  $\mu\text{m}$  ( $\pm 12.5 \mu\text{m}$ )  
SSD layer to TPC within 1 mm ( $\pm 0.5$  mm).
- Electronic operating temperature :  $25^{\circ}\text{C} \pm 1^{\circ}\text{C}$ .
- Detector operating temperature :  $20^{\circ}\text{C} \pm 1^{\circ}\text{C}$ .

#### 3.3.2 Clamshell structure

- The SSD layer has a "Clamshell" structure like the SVT : this gives two half-cylinders independent parts, including 10 carbon beams each, and at each end part one "C" shaped rib of a lightweight, stiff, stable in time. The "C" shaped ribs will be the connecting components between carbon beams and support structure. The "C" shaped ribs will also integrate a water or air manifold for the SSD cooling system. Integration of the two clamshells will be achieved on a dedicated tooling. Like the SVT detector, the interface plane between the two parts is vertical. Design of the SSD clamshells will allow visual access to survey marks and permanent access for adjusting devices of SVT without any dismantling.
- Subatech will provide 4 survey marks at both ends of SSD support for optical survey.
- The material of ribs may be glass fiber composite or carbon fiber composite in order to limit radiation length.
- The total weight of SSD is estimated at 4,5 kg.

### 3.3.3 Ladder

- Silicon Strip Detectors are glued in arrays of 16 wafers on space frame carbon beams. The SSD barrel features 20 Carbon Beams, so each array of silicon wafers covers a phi angle of  $18^\circ$ . Arrays of silicon wafers are located at  $R = 230$  mm from the interaction point. Carbon beams are located outside of the silicon arrays in order to minimize interaction between matter and incoming particles before detection.
- The Subatech group expects to use space frame beams designed and built at St Petersburg (Russia) by G. Feofilov and the MEZON company for Internal Tracker System (ITS) of ALICE experiment. Prototypes are already produced and tested, but they use a "low" modulus of elasticity carbon fiber ( $E = 162$  GPa for composite) instead of a "high" modulus of elasticity as required ( $E = 310$  GPa for composite).  
Length of a beam is 950 mm, it features an equilateral triangular cross-section of 40 mm base (height 35 mm), weight (without silicon detectors, electronic chips and cooling devices) is 21 g. The weight of a fully equipped carbon beam is estimated at 180 g.  
The carbon beam can also be made by a French company, prototypes are on the way.
- The raw material used for space frame beams will be carbon composite material made from a "high" modulus of elasticity carbon fiber ( $E = 540$  GPa for carbon fiber,  $E = 310$  GPa for cured composite) and an epoxy matrix. Deflection of a 950 mm long beam including 16 silicon detectors load will be  $< 25\mu m$  with ends clamped.
- If air cooling is chosen, this will lead some modifications in the mechanical design of carbon beams which will no more have an equilateral triangular cross-section but an isoscele triangular cross-section, with a base 75 mm wide and a height of 35 mm.
- Schedule :  
A pre-production batch (3 units) was delivered from St Petersburg in march 1998, 22 units (including 2 spare units) may be available 14 months after order. Choice between the russian option or the French one will be made during summer 1998.
- Price is quoted roughly at 8 kF for a ladder.

### 3.3.4 Mechanical assembly

- The integration of silicon wafers, electronics, cabling, on a carbon beam will be achieved at Subatech with a dedicated tooling (granite material) in a semi-clean (class 100.000) room at  $20^{\circ}\text{C} \pm 1^{\circ}\text{C}$ , and humidity within 50%-60%.

The granite tooling will define a plane, a lateral location and a longitudinal position for the 16 silicon wafers of an array. The accuracy of wafer location will depend only on tolerances of machining of the granite tooling, and will be independent of geometric defaults of the carbon beam, so it will be possible to use carbon beams with large geometric tolerances, the straightness of the carbon beam may be within 1 mm.

- After setting up at the right location, silicon wafers will be bonded on the beams, via 3 or 4 small rods (pins), with an "elastic" epoxy adhesive, in order to accommodate the difference between coefficients of thermal expansion of silicon ( $+4.7 \cdot 10^{-6}$ ) and of carbon composite ( $-0.4 \cdot 10^{-6}$ ).
- Schedule:  
Design is expected to begin in September 1998 and tooling will be available roughly 9 months after the beginning of design.

## 3.4 Mechanical interface between TPC and SVT (see Fig. 44)

### 3.4.1 Requirements

- Maximum deflexion, under full loading, of the (SVT+SSD) support at the small ends of the cones  $< 2.5$  mm
- Maximum deformation under full loading of a circular cross-section at large ends  $< 1$  mm
- Total length : 4614 mm
- Distance between cones is  $1114.40 \text{ mm} \pm 0.1 \text{ mm}$
- All metallic components will use non magnetic materials.

### 3.4.2 Design

- The Subatech group use a new design for the (SVT+SSD) support. The aims were to reduce the amount of matter seen by incoming particles and to improve stiffness of the support structure. These requirements can be achieved by using a sandwich structure which increases inertia and reduce weight.
- The (SVT+SSD) support features two 1750 mm long cones, linked by two connecting rods and has a sandwich structure, 4.3 mm thick, with honeycomb Nomex (hexagonal cells size 3.2, density  $29 \text{ kg/m}^3$ ) as the core material and 0.4 mm thick skins (4 angle plied layers of high modulus carbon fibers) instead of the 1.52 mm thick monolithic carbon fiber composite used in the former design.

The sandwich (SVT+SSD) support performs at  $\eta=2.0$  a radiation length of 3.2 %  $X_0$  instead of 5.63 % for the former monolithic carbon fiber design.

The connecting components between the two cones are 2 rods with an elliptic cross-section (95.8 x 45 mm external, I.R. 178.5 mm, O.R. 223.5 mm), and a sandwich structure (0.4 + 3.5 + 0.4)mm like (SVT+SSD) support. Like cones, core is honeycomb Nomex with rectangular cells, size 4.8, density 29 kg/m<sup>3</sup>. These 2 rods perform a reduced total mass (607 g instead of 1164 g) for the same global stiffness than the 4 former cylindrical Be rods.

Carbon fiber composite used for skins of cones and connecting rods performs a modulus of elasticity of 310 GPa after curing.

$X_0$  max is 1.8 % for an elliptic sandwich rod, 3.5% for a cylindrical Be rod. Mean value of  $X_0$  is 0.762 % for one elliptic sandwich rod, 0.851 % for two cylindrical Be rod, both covering a  $\pm 15^\circ$  phi angular area (see Fig. 42).

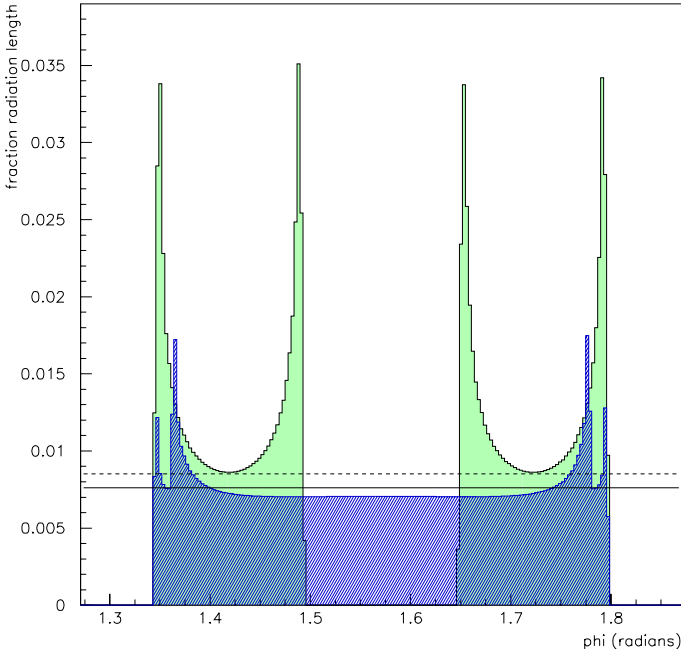


**Figure 42:** Comparison between two elliptical cross-section tubes (hatched) and four tubes (filled) for the connecting rods.

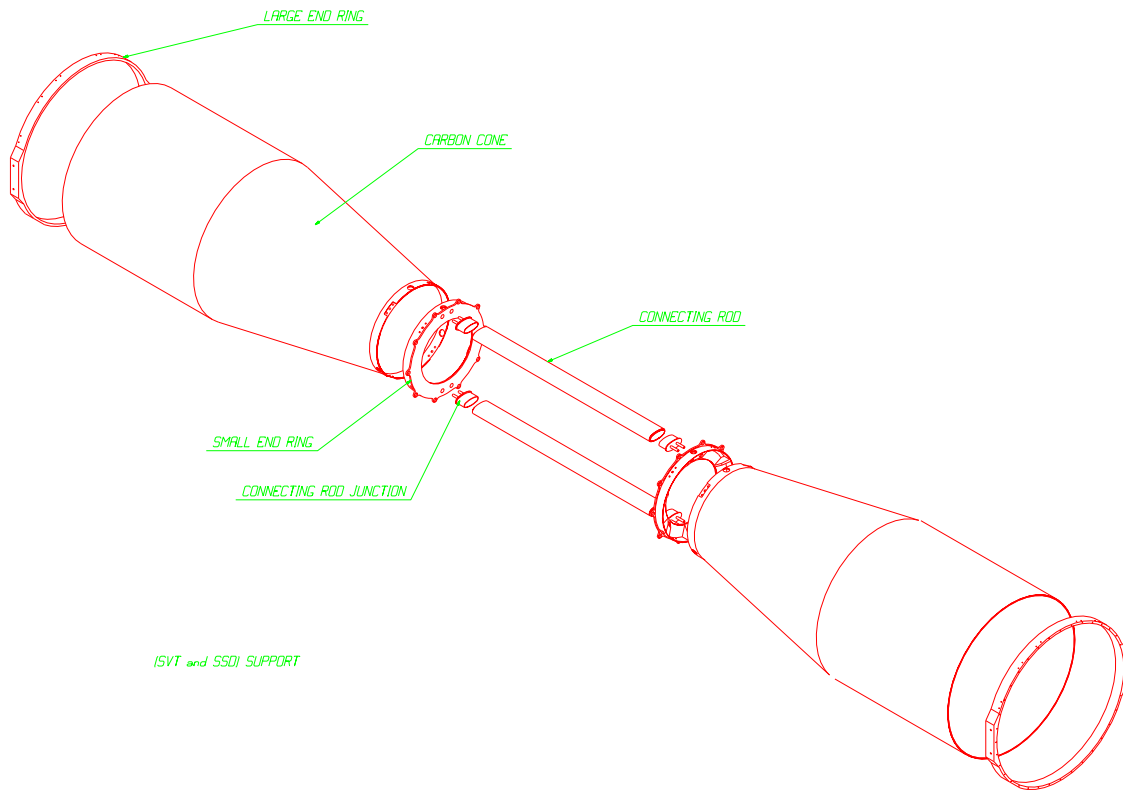
Mean value for elliptical cross-section tubes :	0.762 % $X_0$
Mean value for tubes : averaged over the same angular zone than the carbon fiber tubes	0.851 % $X_0$
Mean value for tubes : averaged over the active zone of beryllium tubes	1.263 % $X_0$

Table 6: Fraction of radiation length for tubes

- The (SVT+SSD) support (see Fig. 43) features 2 machined rings of aluminium alloy located at the small diameters of the cones in order to achieve a good initial positioning for the SVT and for the SSD. During assembly, these two small rings will be first clamped (bonded) to the connecting rods on a dedicated tooling in order to achieve good coaxiality and parallelism between these 4 components (within 0.2 mm).  
The small end rings also supports the beam pipe while main supports of the beam pipe are 7700 mm apart at the flanges location. Connecting parts between beam pipe and small diameter of the cones will allow sliding of the beam pipe. The temperature of the beam pipe at bake-out is 150 °C.
- At large ends, there are aluminium alloy rings which act as stiffener and inter-connect components between (SVT+SSD) support, TPC and rails.
- All components were made separately by different companies. Assembly is expected in July-August 1998 by Subatech group on a dedicated tooling in order to perform good coaxiality between the 2 cones. All components will be assembled with an epoxy adhesive at room temperature.  
Final integration at BNL of the support cones will be achieved with participation of Subatech group.
- Results of simulations for the carbon sandwich design, with a 3D finite elements application (SYSTUS):  
Maximum deflexion, under full loading, at middle of connecting rods within 0.9 - 1.0 mm  
Maximum deflexion, under full loading, at the small ends of the support within 0.60 - 0.70 mm  
Maximum deformation, under full loading, of a circular cross-section within 0.60 - 0.70 mm
- Schedule : Start of design, September 1997. Orders to companies, February 1998. Delivery of cones and connecting rods, June 1998. Assembly at Subatech workshop, July-August 1998. Delivery to BNL expected in October 1998.

Components	Previous design	Actual design
Single cone	15.6 kg	7.1 kg
Support (2 cones + connecting rods + rings)	36.0 kg	23.0 kg
Support + SVT + SSD	61.0 kg	48.0 kg
Support + SVT + SSD + cables	181.0 kg	168.0 kg

Table 7: Comparative weights between the previous and actual designs



**Figure 43:** Disassembled view of the cones, rings and connecting rods.

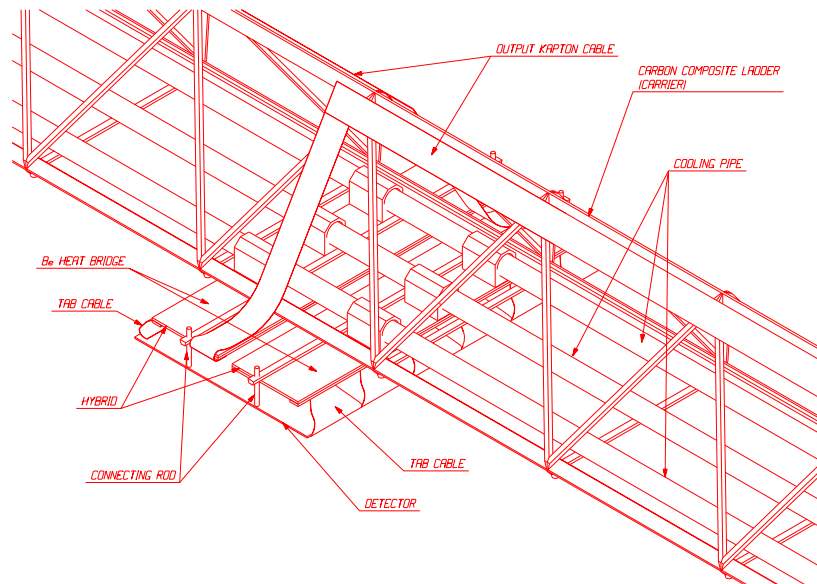


**Figure 44:** FEE/detector module integrated on a ladder (water cooling design).

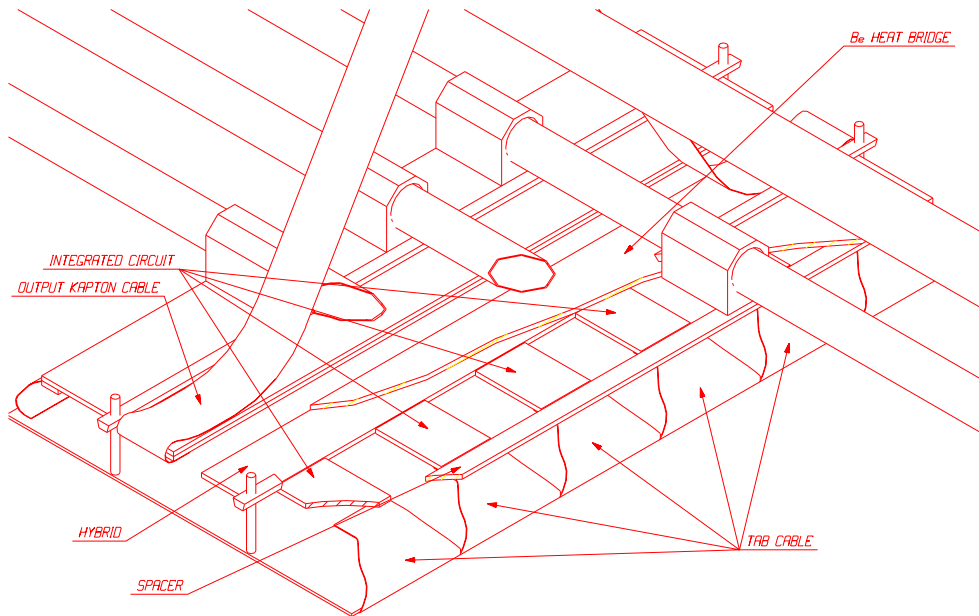


**Figure 45:** Detailed view of the FEE/detector module.

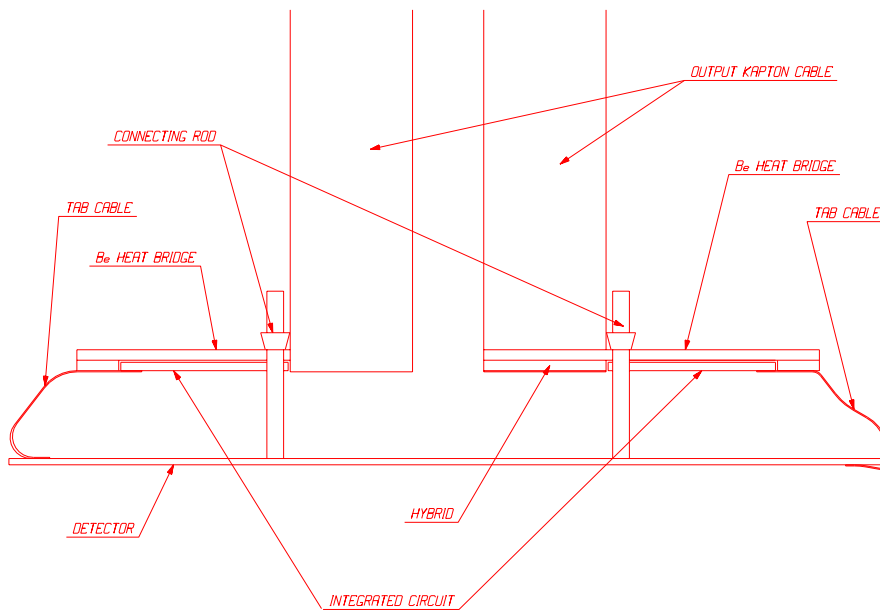


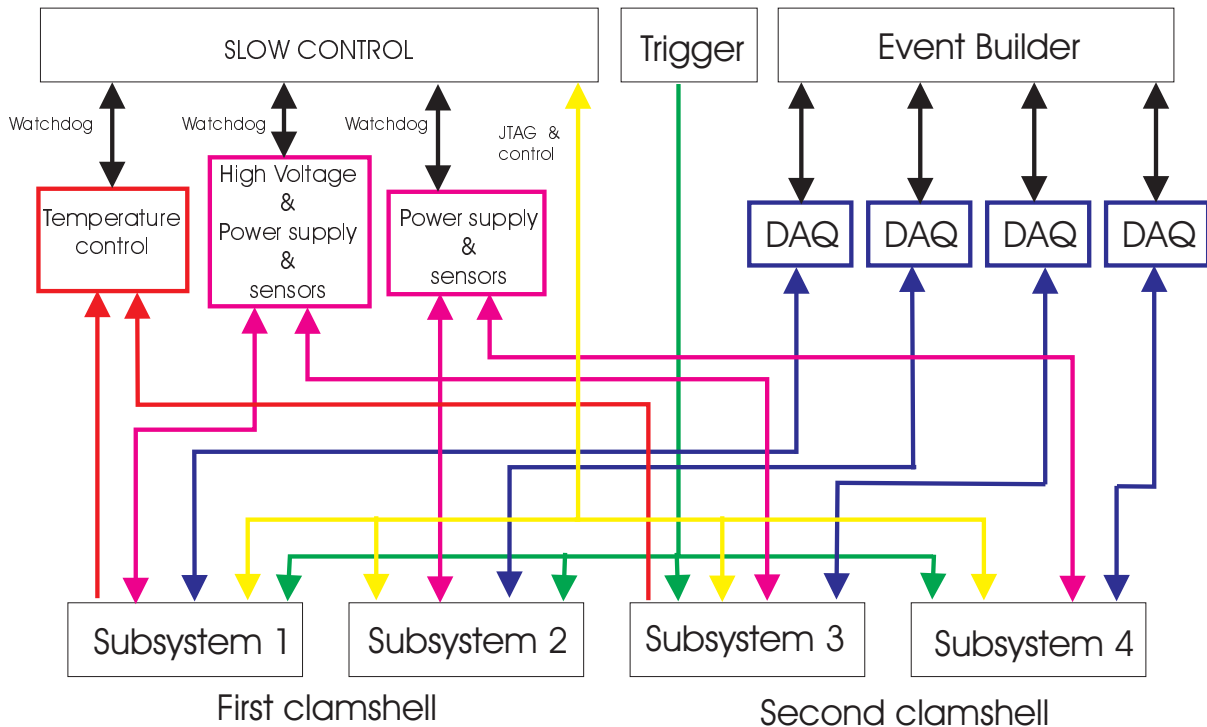
**Figure 46:** Side view of the FEE/detector module.

## 3.5 Readout system

### 3.5.1 Description of the readout system

The global system managing the SSD can be shared in three main parts (see Figs. 47,50):

- the "slow control" system which controls the power supply and the high voltage of the barrel, and performs the JTAG protocol for the initialization and the testing of the front end electronics.
- the "readout control" system which transfers and generates all the signals necessary to the ADC boards and the front end electronics.
- the "readout" system which controls the digital data transfer through an optical fiber to the counting house where the zero suppression and data compression are performed.



### Overview of the electrical system

Figure 47: Schematic view of the electronic system.

The electronic system works in 3 modes :

- Initialization Mode
- Test Mode
- Readout Mode.

In the "Initialization Mode", only the slow control is involved with the "JTAG&Control" bus. This mode is used to program all the different blocks inside the front end electronics like DACs for the biasing parameters. This mode has to be selected, at least once, before doing the two others.

In Test mode, digital tests and analog tests can be performed. Digital tests are boundary scan of the internal register of the chip. Analog tests are performed by programming the amplitude of the input pulse and the tested channel. In the analog test the slow control and the DAQ are involved.

The Readout Mode is the mode used when the system is waiting for the trigger signal. Due to the shaping time of the front end electronics the trigger signal should come before 2.  $\mu$ s. Once this signal is sent, all the analog data held in the front end electronics are transferred to the ADC, digitized and then transferred to the DAQ system, where the zero suppression and the data compression is made.

Physically, the readout system is shared in four parts, two per clamshell, one on P side (or low voltage side) and one on N side (or high voltage side). Each part has its own power supply, slow control system, readout control board, fast digital data transmission system and data compression system.

### 3.5.2 The Front End Electronics

The front end electronics is mounted on a hybrid supporting the front end chips. The foreseen chip, ALICE 128C has been designed to lower the power consumption and to remove all external components. It requires therefore a control protocol for its operation and its tuning.

The ALICE 128C chip is developed by LEPSI in Strasbourg for the two layers of silicon microstrip detectors of the ALICE ITS (Inner Tracking System). Each of the 128 channels of this integrated circuit preamplifiers, shapes and holds (when the hold pulse is sent) the signal coming from the detector.

Once the 128 signals are held, they are multiplexed to one output through 128 intermediate buffers and one output buffer. The selected output channel is defined by a token which moves under control of the readout clock. The token output allows daisy-chaining of several chips, without additional components. The 6 chips per side of the detector and the 16 sides per ladder will be daisy-chained. This provides a multiplexing ratio of 12228:1.

To save power consumption all the buffers are switched off during the sample & hold phase. When the circuit is readout the output buffer and 4 intermediate buffers are switched on. This will lead us to a power consumption of 4.1 watts for 16 sides or half a ladder and a total power consumption of 164 watts for the whole front end electronics (see Appendix B).

The electrical characteristics of the chip extracted from simulations are the following:

- input dynamics:  $\pm 300\,000$  electrons
- gain: 50 mV/MIP
- shaping time: adjustable from 1.4  $\mu$ s to 1.8  $\mu$ s
- noise: ENC  $\leq 400$  e<sup>-</sup> for an input capacitance of 8 pF
- power supply:  $\pm 2$  V
- output buffer: rise time 20 ns on 100 ohms with 20 pF in parallel
- nominal readout clock frequency: 10 MHz
- digital I/O on standard CMOS  $\pm 2$  V levels
- LVDS standard (Low Voltage Digital Signal) is used for fast timing signals (Read-Clock, Hold and Test) for speed and crosstalk.

The bonding pads characteristics are:

- pitch of 44  $\mu$ m in staggered row for the input reading pads
- standard pitch for the rest of the other pads.

New features has been added to the circuit for automated testability and tuning. It uses the IEEE standard JTAG control protocol and allows analog as well as digital tests. Analog tests are made by controlling various parts of the chip:

- programmable internal test input signal generator for online testing
- input pattern test register
- output pattern register
- output buffer which can be switched off
- internal DAC registers to program the biasing current, the feedback resistors and different other part of the circuit.

Digital tests are made by performing the following operations:

- boundary scan
- read/write of all digital registers
- by-passing of the TDI-TDO JTAG stream at start up
- by-passing of the read token at start up
- controlling the output buffer on/off switch.

Control requirements:

Specific control requirements listed below correspond to the operating modes of the front end chips. The control routines are theoretically only needed for hardware tests or for setting the parameters after power up. JTAG control clock speed is typically 100 kHz.

- Setting and tuning mode: This is the standard JTAG operation control mode. and drives all DACs for biasing currents, voltages, feedbacks for gain and shaping time and different other analog parts of the circuit.  
This process requires a bit stream of 90 clock pulses for each chip and a total of 11,350 clock pulses for  $16 \times 6 = 96$  chips.
- Analog tests: This process requires a bit stream of 256 or 523 clock pulses respectively for standard token readout or for a predefined channel readout for each chip and a total of about 20,000 or 50,000 clock pulses for  $16 \times 6 = 96$  chips (half a ladder).
- Digital tests: The control streams can be linked either through the slow control general link or use an upstream channel of the data acquisition. The control routine runs as an application program over or beside the data acquisition general feature.

### 3.5.3 Hybrids circuit

The hybrid circuit which supports the front end electronics will be fabricated using standard hybrid technology. The substrate will be made in beryllium or carbon composite with an insulation layer, in order to minimize the radiation length and to offer a good heat transfer to the cooling tubes.

Signals are routed in one direction by the TAB cables (see section 3.5.4.1) and in the other direction by a little piece of BeO glued on the substrate. A way to process thick layer technology directly on the beryllium substrate is investigated.

### 3.5.4 Detector and FEE module

The detector and the front end electronics will be first assembled before the integration on the carbon ladder (see Figs. 45 and 46). It is foreseen to test every module after the assembly with a laser diode.

#### 3.5.4.1 Connection between the silicon strip detector and the front end electronics

The link between the detector and the FEE is foreseen to be a microcable using TAB (Tape Automated Bonding) technology.

The tape is made of one kapton layer (polyimide  $70\ \mu\text{m}$  thick) and one layer of copper ( $20\ \mu\text{m}$  thick). The same sort of tape with aluminium strip would be better, but it seems it is not a standard process in the industry.

To avoid the  $44\ \mu\text{m}$  pitch of the FEE input pads, which is not standards at the tape manufacturers, the tape designer proposed an alternative solution (see Fig. 48).

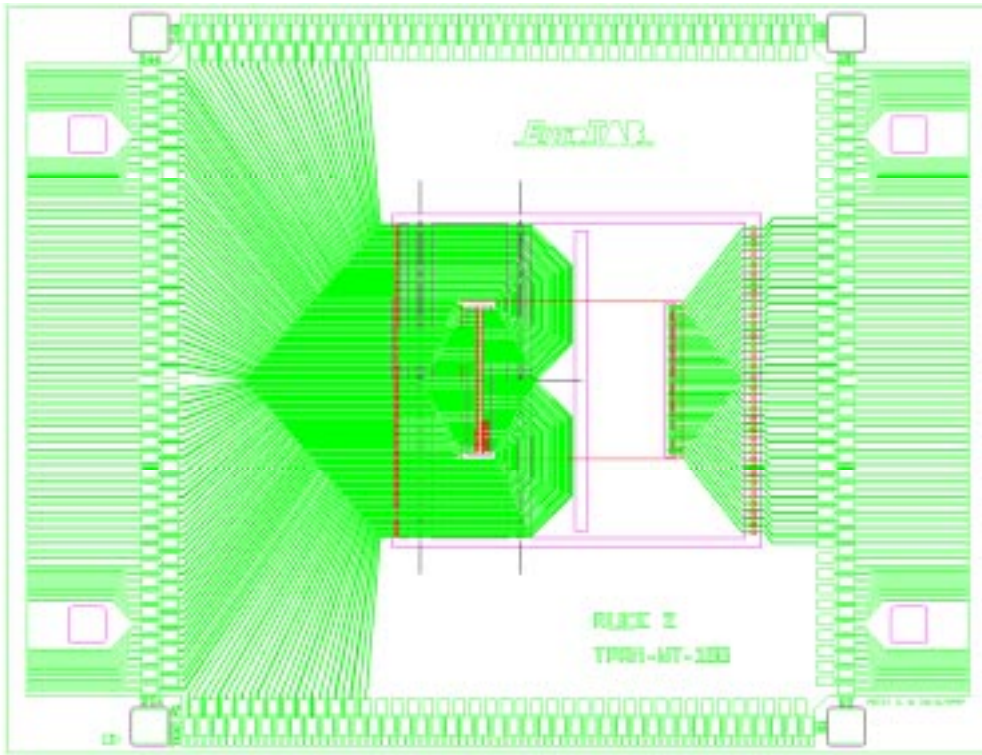


**Figure 48:** TAB cable foreseen for the detector to FEE connection.

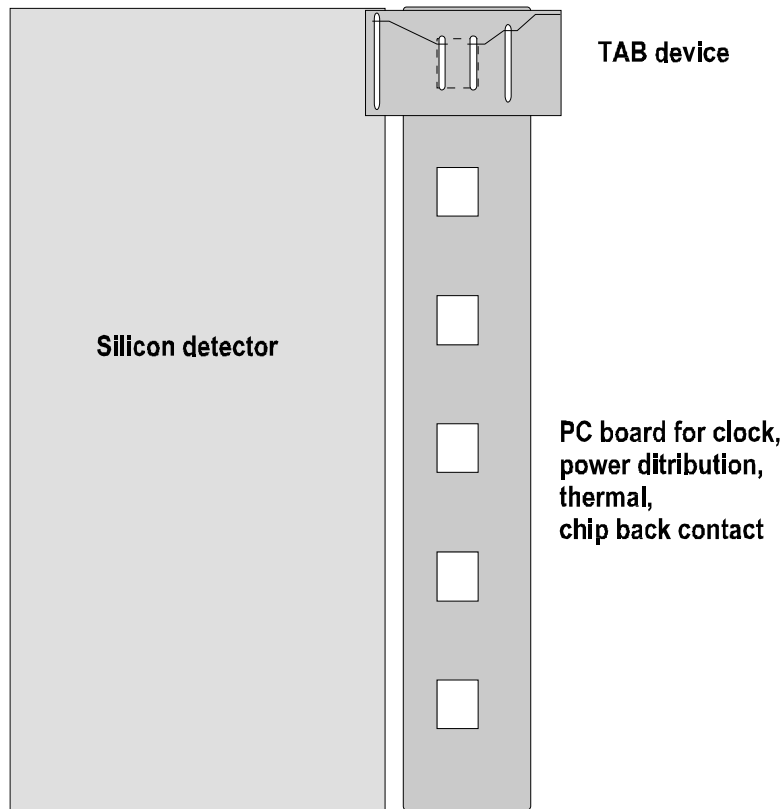


**Figure 49:** Example of solution for the connection

There is one of these tape per FEE chip, so 6 per hybrid (see Fig. 49).

### 3.5.4.2 Connections between FE electronics and the rest of the system

Those cables are soldered to the hybrid circuits and to the ADC & Readout Control board to insure a good reliability. The material used for the conductors is foreseen to be aluminium.

This cable routes the power and biasing signals, JTAG signals, and Control and readout signals (cf Appendix C). It consists of 19 lines and results of a width of roughly 5 mm.

### 3.5.5 ADC&control board (see Fig. 50)

The purpose of this board is to interface the front-end electronics with the rest of the system (slow control, power supply and DAQ). It has three main features:

- power supply and high voltage transfer (for the N side readout) to the detectors,
- control, a decoder reads the "Address&control" bus and generates all the signals necessary to drive correctly the front end electronics (clock, reset, test signal, token ...),

- conversion of the analog signal coming from the front end electronics and data transfer to the DAQ.

For the rest of the signals coming in and going out (JTAG, Hold, ...) of this board, this one remains transparent and insures only the transfer of them from outside to the front end electronics.

The power consumption of this board is evaluated as following:

- control (FPGA : Altera EPM7032LC44-6): 120 mW
- analog to digital converter (AD875 or AD876): 160 mW
- buffer and line drivers and optocoupler : < 1 W

The total consumption will not exceed 2 W, which gives a power consumption of all the "ADC&control" boards of 80 W, which is not critical regarding their foreseen locations on the water manifold.

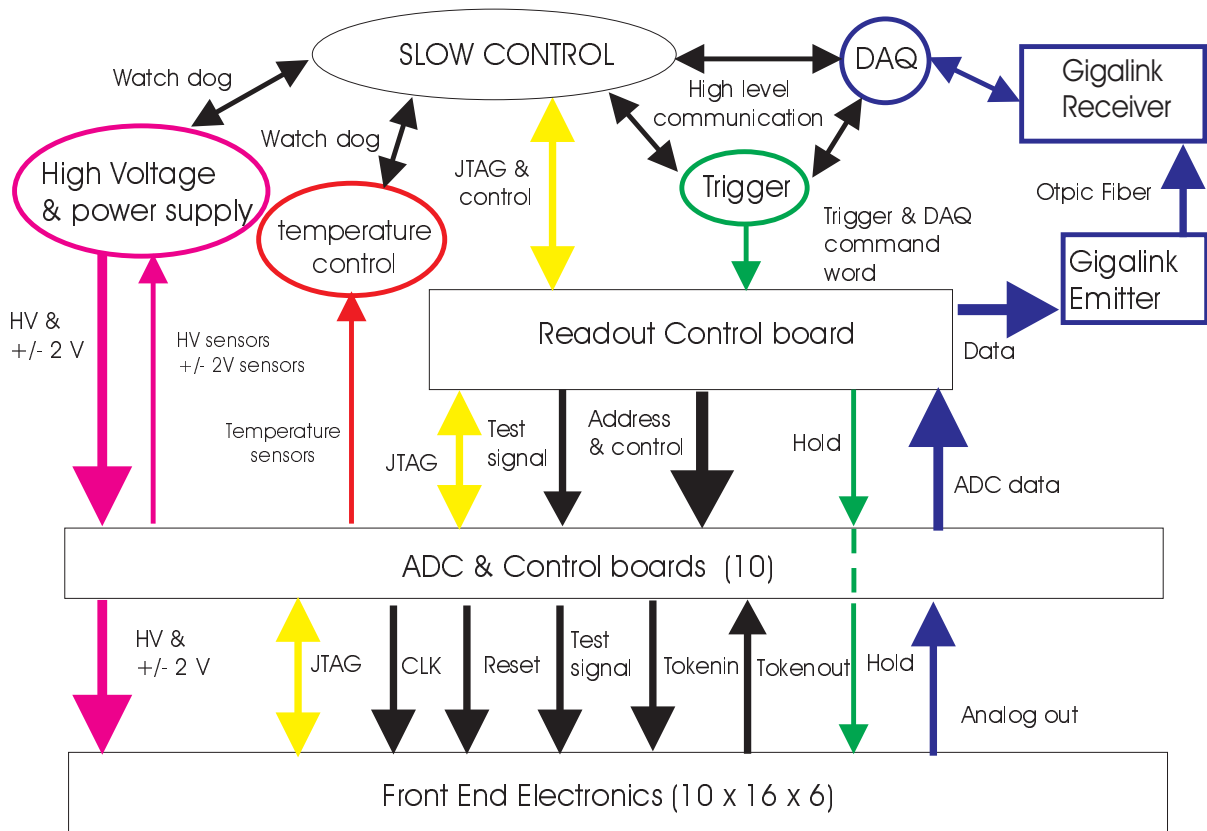
### 3.5.6 Readout control board (see Fig. 50)

This board is the interface between the ADC& control board and the external system: Slow Control, DAQ, Trigger. This board works in the three modes required by the global SSD system (cf. section 3.3). There will be 4 of this kind, one per half end vertex barrel. They will be located on the TPC wheels.

To manage and control the three modes of the readout system, the readout control card needs to be connected to the following buses and signals :

- "JTAG&control" bus is composed by the JTAG bus, an address bus to select one ladder from the others, and several other signals like reset and test command,
- "Control" signal is used to force the "Readout&Control" board in readout mode,
- "Trigger" signal is used to generate the Hold signal in readout mode,
- "JTAG" bus is a prolongation of a part of the "JTAG&control" bus,
- "Test signal" is a pulse needed for the analog test of the front end electronics. It triggers the pulse injected into the preamplifiers with an amplitude defined by JTAG programming
- "Address&control" bus is 4 bits bus. It performs the addressing of the ladders, the reset of the electronics, the general readout clock, and the setup of the electronics in the test mode,
- "Hold" signal which is the trigger signal in the Readout mode, can be performed as well in the test mode.
- "ADC data" bus to perform the readout scheme by writing 0 when necessary (see 3.5.7.1 Readout via the Gigalink).

All the functionality of this board is performed by a FPGA (EPM 7096LC68-7)



## Subsystem

**Figure 50:** sub-system of the readout system for the one-half clamshell.

### 3.5.7 DAQ

#### 3.5.7.1 Readout via the GigaLink

The number of channel given by the SSD to the Data Acquisition system is 491520. It is divided in four sectors (two clamshells, high and low voltage of the silicon detectors). The front-end electronics of each sector (seen by the Gigalink) is composed with ten ADCs and one multiplexer on a Readout&Control board. One board has to handle 122880 channels. Each board is connected to a gigalink via an optical interface.

On the other side of the optical fiber is a DAQ-TPC receiver board located in a VME 9U crate. Those DAQ-TPC receiver board will be standard ones, without any peculiar hardware modification for the SSD. The DAQ-TPC receiver board is composed of 3 mezzanines hosting 6 STAR ASICs each.

The STAR ASIC [44] was originally developed to read time multiplexed detectors like Time Projection Chambers or Silicon Drift Detectors. Contrary to those detectors, the SSD is not made of time multiplexed elements, but with a total of 491520 channels, the SSD has a rather high number of cells. In order to keep the number of STAR ASICs low for the SSD, the time multiplexing feature of the ASIC will be used to multiplex the SSD channels. Without these option a prohibitive number of DAQ receiver card (more than 100) would be necessary. The proposed design requires only 4 of those cards.

In order to have a balanced load on the ASICs, it is proposed to logically bind one ADC to one STAR ASIC letting unused 8 STAR ASICs on the TPC receiver board.

The STAR ASICs can handle a new data every  $154\text{ ns}$ . On the detector side, the ADC are able to sustain a frequency of  $5\text{ Mhz}$ , providing a new data every  $200\text{ ns}$ . The gigalink will therefore be used at  $900\text{ Mhz}$  (90 millions 10 bits data word per second) to match the speed of the ADC.

After 5 values a '0' is inserted in order to feed the last ASIC of the first mezzanine. After 5 more ADC values, 7 '0' will fill the last ASIC of the second mezzanine and the 6 ASICs of the third one.

Each ADC has to generate 12288 values at  $5\text{ Mhz}$ . The total amount of time required to read out the SSD is  $2.5\text{ ms}$ . This is well below the  $5\text{ ms}$  limit set by the TPC. If the  $5\text{ Mhz}$  clock inside the SVT is a problem, an option to reduce the ADC speed up to  $4\text{ Mhz}$  still exists, increasing the read out time to about  $3.1\text{ ms}$ .

As an error detection scheme is foreseen between the ADC and the multiplexor board, the error reports may be coded as a data value for the last ASIC.

### 3.5.7.2 Data processing with the STAR ASIC

Used in TPC mode, the STAR ASIC is intended to be connected to 64 detector channels, each channel is read from 4 to 1024 times per event. For the SSD, 192 time steps are required.

Just after receiving a data, the STAR ASIC subtracts an offset or "pedestal" from the data, applies a translation function to it and after a thresholding step eventually passes the result to a FIFO for the readout. Those steps were defined from the requirement of the STAR TPC and SVT.

As pedestal subtraction value depend both on the detector number and the current time bin, this computation can be made with the STAR ASIC for the data coming from the SSD with the scheme described above.

Contrary to the pedestal subtraction, the look up translation function that compresses the 10 bit ADC data to an 8 bit value depends only on the detector number. The ASIC can handle a maximum of 256 such translations functions. It is then proposed to use only one translation function for all channels. Further studies are needed

to evaluate the potential losses from this constraint. It is also foreseen to sort out the detectors and FEE in order to match their gains. If the result of this pairing allows it, more than one compression function per ASIC could also be used.

The cluster finding algorithm built in the STAR ASIC can recognize clusters with a length of only one time step. Zero suppression of the SSD data can be done this way. In TPC mode, the ASIC can compile 31 lists of clusters for each of the 64 detectors channels. For the SSD it means 1984 over threshold values. It corresponds to a maximum of about 16 % occupancy, well above the expected 2 % occupancy expected for an  $Au + Au$  collision at  $200 \text{ GeV}/u$ . The data volume on each mezzanine is about 6 kbyte considering a 32 bit address word and an 8 bit value. The total SSD data volume is about 50 kbyte per event.

As the SSD does not participate to the trigger decision, its TPC receiver board should respond to the trigger token like others receiver boards connected to detectors uninvolved with the trigger.

### 3.5.8 Readout timing

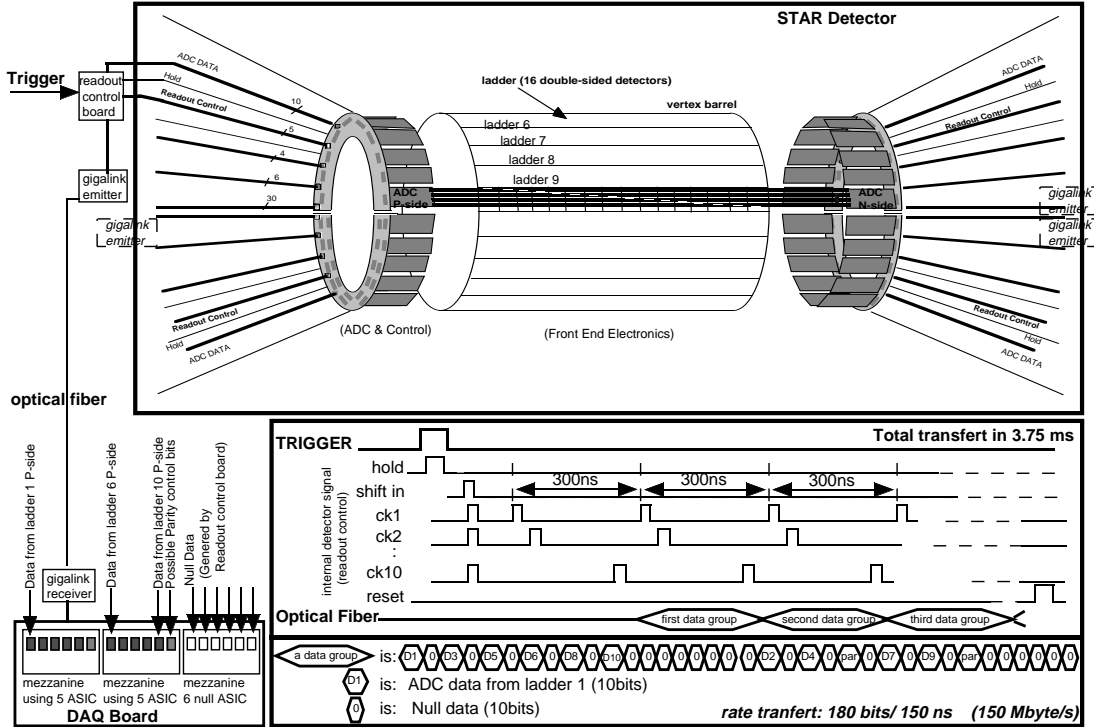


Figure 51: Readout transfer schema.

The readout strategy of the SSD is the following: (see Fig. 51)

- the Hold signal, generated by the Trigger signal, commands the front-end electronics to store the signal coming from the detector,
- the token signal (or shift in) is generated and sent to the front-end electronics,
- the ADC board starts to convert the stored signal, and sends the data to readout&control board,
- 10 ADC board are multiplexed together, that corresponds to one half clamshell,
- each ADC board has its own address, so the “Address&control” bus will control, via a decoder, the conversion at “Address” and the transfer of the data at “Address + 2”

The total time, for one ADC board, between two conversions is  $200ns$  and the data rate through the data bus is about  $1\ data/20\ ns$ . So the whole front-end electronics and the ADCs will work at  $5\ MHz$ , which is one third the nominal value.

The total readout time will be  $16 \times 768 \times 10 \times 20ns \leq 2.5\ ms$ , which is below the maximum time imposed by STAR.

### 3.6 Slow control

During standard operation, the slow control is in charge of the monitoring of “slow” variables and parameters i.e. essentially temperature and power supplies (low and high voltage). Specific control functions are needed for the front end electronics. Each of the front end chip includes a JTAG controller for initializing, setting, monitoring, testing, calibrating, investigating and fail mode operation (switching off of faulty chips).

#### 3.6.1 Specifications

The slow control must be able to be operated in the stand alone mode for testing and tuning purpose. This means that it must contain its own facilities as on line help files, diagnosis tools, initializing processes, alarm processes, logging facilities, a data base for settings, reference measurements, alarm levels, user interface with display windowing management.

A PC running LabView under Windows NT should achieve the job. A rackable version is investigated with PCI hardware interfaces or VME bus interfaces. 8 bit measurements will provide a sufficient accuracy for temperature and power supplies. A bandpass under  $100\ kbit/s$  is more than enough to scan whole detector layer within seconds. At present, one considers an electrical structure of 40 floating half ladders, 20 half ladders being at ground level and 20 at high voltage (depleting voltage). All the control parameters are splitted according to this structure. DAQ, control data and power supplies follow the same paths.

### **3.6.2 Communication**

The stand alone slow control needs communication with the DAQ in order to monitor the acquisition especially in test and tuning mode. It needs also communication with the main STAR control in order to down load and to upload the current parameters and settings and to provide the needed parameters to the experiment control room.

These two links don't require any specific speed characteristic. A bandpass between 10 and 100 kbit/s is enough for this purpose which is achieved by any serial link.

### **3.6.3 Power supply**

40 power supplies clusters, located on the platform, feed the low voltage power for the 40 half ladders electronics and their associated Readout and control boards. Each cluster involves +/- 2V for the front end electronics, +/- 2V for the ADC & control board, for the readout control and for the data drivers. Thus, 20 half ladders and their associated electronic boards are strapped to the ground level whereas the 20 remaining ones are fixed at the depleting voltage by means of 20 high voltage power supplies. The monitoring of the low voltage power supplies is performed by means of sense wires which feed the FEE voltages taken on the ADC & control boards towards the platform equipments.

### **3.6.4 High voltage monitoring**

The current being very low, the monitoring of the high voltage power supplies is performed in the power supply crates which are located on the platform.

### **3.6.5 Temperature control**

The monitoring of the temperature is preferably achieved on the FEE hybrid itself or on the input and output cooling pipes. The first option makes use of one temperature sensor for each hybrid, all the sensors of a half ladder being daisy chained in order to provide one measurement for each half ladder. Using the temperature increase between input and output pipes provides the same number of measurements. The measurement of the cooling fluid pressure and speed is in discussion.

### **3.6.6 FEE control and test**

The FEE is controlled by means of the JTAG lines and protocol. At start-up, all the chips are idle and each of them must be activated during an initializing process. All the operation parameters are set. The chip parameters have been stated earlier in 3.5.2. The test and tuning of the whole detector layer is achieved by looping into several steps which are: setting parameters, generating input test pulses by means of an internal variable charge generator, making acquisition in this test mode, analyzing

the acquisition data and setting new improved parameters. As far as a minimum functionality is available, each FEE chip can also be switched off in the idle state if needed.

### **3.6.7 Opto isolation**

Opto isolation is a standard feature for all the links between the control processor and interfaces and the ladders with their associated electronics. It has to meet about 100 V of electrical voltage difference.

### **3.6.8 Alternative option**

The design of a dedicated control chip is in discussion. This chip would be a down scaled Alice 128C FEE chip with the same output pin out and the same JTAG controller. It would include an analog multiplexer and at least one ADC in order to sense temperature and voltages in situ on the FEE hybrid, the readout being achieved by the same JTAG wires as the standard FEE chip. At the moment of writing this document, this later option remains in discussion.

## **3.7. Front End Electronics Cooling Systems**

The cooling goal is to dissipate the heat produced by the FEE (Alice 128C) outside the barrel with no temperature perturbation for the Silicon Drift layer and to assure a temperature lower than 25<sup>0</sup>C of the electronics.

The power consumption of the FEE is estimated to 164 W.

- 8.2 W for a ladder
- 0.513 W for a detector module (12 ALICE 128C chips)

There are two major solutions to perform the front end electronic cooling:

- water cooling
- air cooling

### 3.7.1 Water Cooling

The constraints of the problem are :

- power to dissipate : 8.2 W/ladder
- gradient of water temperature : 1°C
- radiation length to be minimum
- thermal transfer to be maximum
- cooling system under atmospheric pressure

The first and second points give a constraint on the water speed and the cross section of the tube. Points three and four give a constraint on the tube shape and point five gives a constraint on the pressure drop (limit for STAR : 14000 Pa or 2 Psi).

At a first time, a test was made with round tube (inner diameter 2.2 mm and 1 m length). The power was produced with SMD resistors (9.39 W) and the pressure drop was 14000 Pa. The power dissipated by cooling is 7.24 W (77 % of the power produced) and the gradient of water temperature is 1.06 °C in average. The mean value of the radiation length of the water is 0.014% of  $X_0$ .

It is expected to use Be (with an insulating kapton tape) or BeO both as hybrid board substrate (instead of  $Al_2O_3$ ) and as a heat bridge. SUBATECH will request quotations for these two materials and do some thermic simulations.

In order to avoid a temperature gradient on heat bridges, the single  $\varnothing$  5 mm tube will be replaced by a system of 6 parallel small beryllium tubes, 0.01 mm thick walls, with a rectangular cross-section and a thickness of roughly .5mm for the water line.

Each rectangular tube will be located below a FEE chip, so the use of 6 small section tubes allows to avoid the implementation of an additional heat-bridge, because cooling is applied where heat is dissipated. The solution will lead to a lower and more uniform distribution of material on the detector surface and consequently on the radiation length (the goal is 0.65 %  $X_0$ ).

There are alternative solutions for heat bridges :

- Be (216 W/m.K isotropic thermal conductivity),  $X_0 = 353$  mm, conductive material.
- BeO (380 W/m.K isotropic thermal conductivity),  $X_0 = 157$  mm, electric insulator (see 3.5.3).

The Nusselt number (ratio heat flux exchanged by convection over heat flux exchanged by conduction) depends on the shape of the tube. For a round tube the Nusselt number value is 3.6 . If we want to optimize the heat transfer we have to maximize the Nusselt number and take a rectangular cross section tube with a small ratio width (a) over thickness (b). We choose two options for the rectangular cross

section : one case with  $a=75$  mm and another one with  $a=10$  mm. The Nusselt number value is around 7 with these dimensions.

We plot for different values of thickness the dissipated power with a pressure drop of 14000 Pa (see Fig. 52). We can conclude that it is possible to cool down the electronics with a thin rectangular tube. For example : with a tube of 1 cm width and 0.5 mm thickness the power dissipated is 10 W for a water speed of  $0.46 \text{ m}\cdot\text{s}^{-1}$ .

But it may be not the best way, in particular due to the radiation length introduced in the detector by tubes and water. Moreover the design required lightweight material like Be, which is not easy to implement and also expensive.

So a way to cool down the FEE with air instead of water has been investigated.

### 3.7.2 Air Cooling

The main constraints of the problem are :

- Power to dissipate : 8.2 W/ladder
- Chips must be in contact with air
- Air flow must be guided from the entrance to the exit

There are different options to perform air cooling :

- The first one considers a detector module like a pipe. A detector module is composed of one silicon strip detector, two hybrid supports for the FEE and TAB cables. This geometry can be easily compared to a pipe where we can pulse dry and clean air (see Fig. 53). The air flow is directly in contact with the 12 chips and we optimize heat transfer. Air from outside of the barrel can be supplied in each detector module by a pipe on one side of modules. The output heated air can be collected in an other pipe on the other side of modules. In this case we control perfectly the air flow with no perturbation for inner detectors. **Moreover we can control the air flow to adjust the electronic temperature below  $25^{\circ}\text{C}$ .**
- The second one consists to integrate the air tube in the mechanical structure of the ladder. Alice 128C chips must be on the outer side of the hybrid support (in view of the TPC). We can use the ladder, covered with a kapton sheet, as air cooling pipe (see Fig. 54)

## **Air cooling tests (first option)**

We performed tests with a scale model of a detector module to determine the appropriate air flow to cool the chips. Each Alice 128C is replaced by SMD resistor. Chips and air temperatures are measured by thermocouples. The air flow is measured by a ball flow-meter.

Results are presented on Fig. 55 for 0.550 W power dissipated with no cooling and air flow cooling. Temperatures can be stabilized at 24.5°C with an air flow of 7 liter/mn. This value of flow corresponds to 112 liter/mn for one ladder and 2240 liter/mn for the SSD barrel. In this case the air temperature gradient is 1.5°C in average which corresponds to an absorbed power of 206 mW (around 40 % of the power dissipated by the FEE). This result is preliminary and very encouraging.

A test on a full scale ladder has been done. The power dissipated by the air flow was about 70 % of the total 8.48 W power produced by the electronics. This result is close to the results obtained with the water cooling system.

## **Conclusion on the Air Cooling**

- good cooling efficiency (close to the water system)
- Few material, (the 10 % of the SSD radiation length due to the water cooling is removed)
- no water leak constraints
- simplified design and implementation (pipe can be used as mechanical structure for modules)
- cheaper than water cooling

At this point we have to study the best way to integrate air tube in the mechanical structure to minimize radiation length. The remaining issue with the air cooling system is to find a size for the air tubes suited to the SVT envelope.

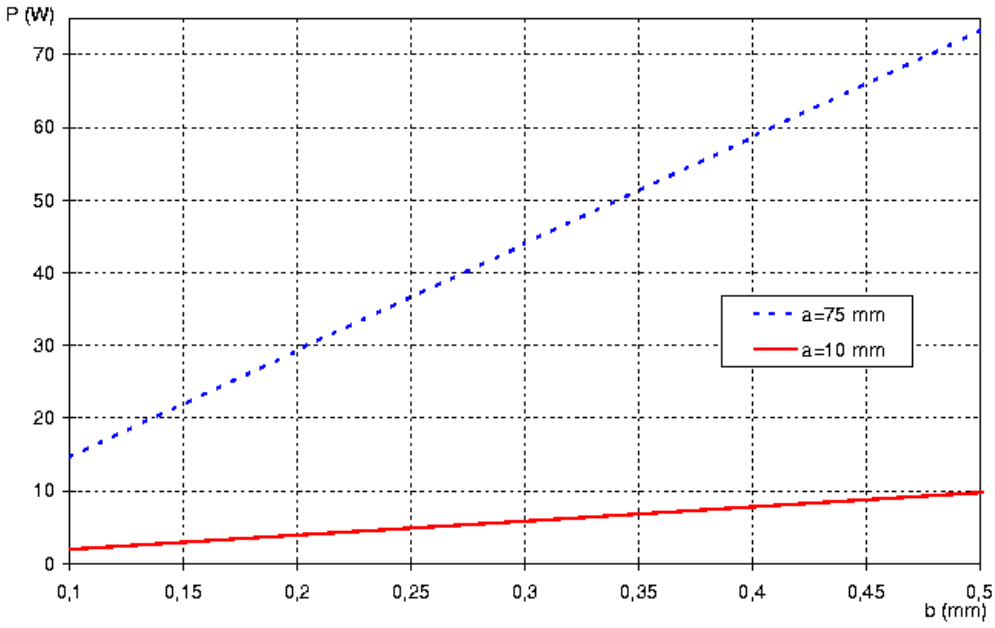


**Figure 52:** calculated power dissipated by water as a function of water thickness for two width of tube.

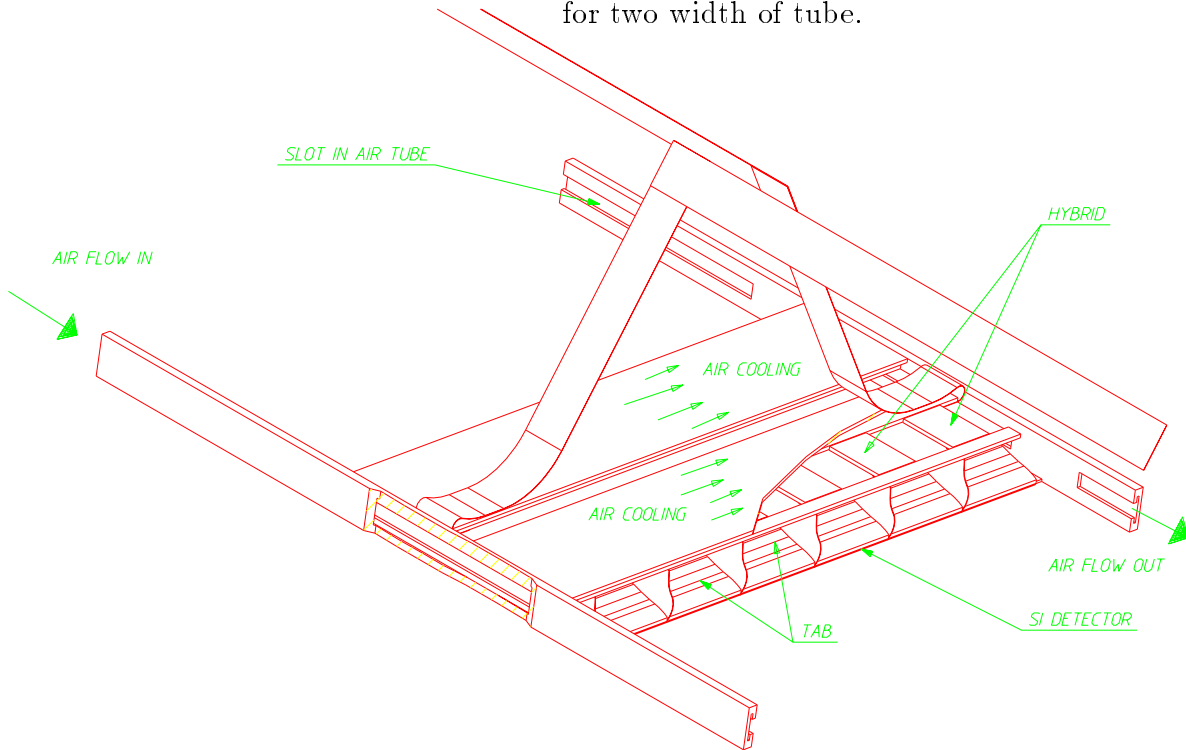


**Figure 53:** Detector module view with air cooling tube (first option).

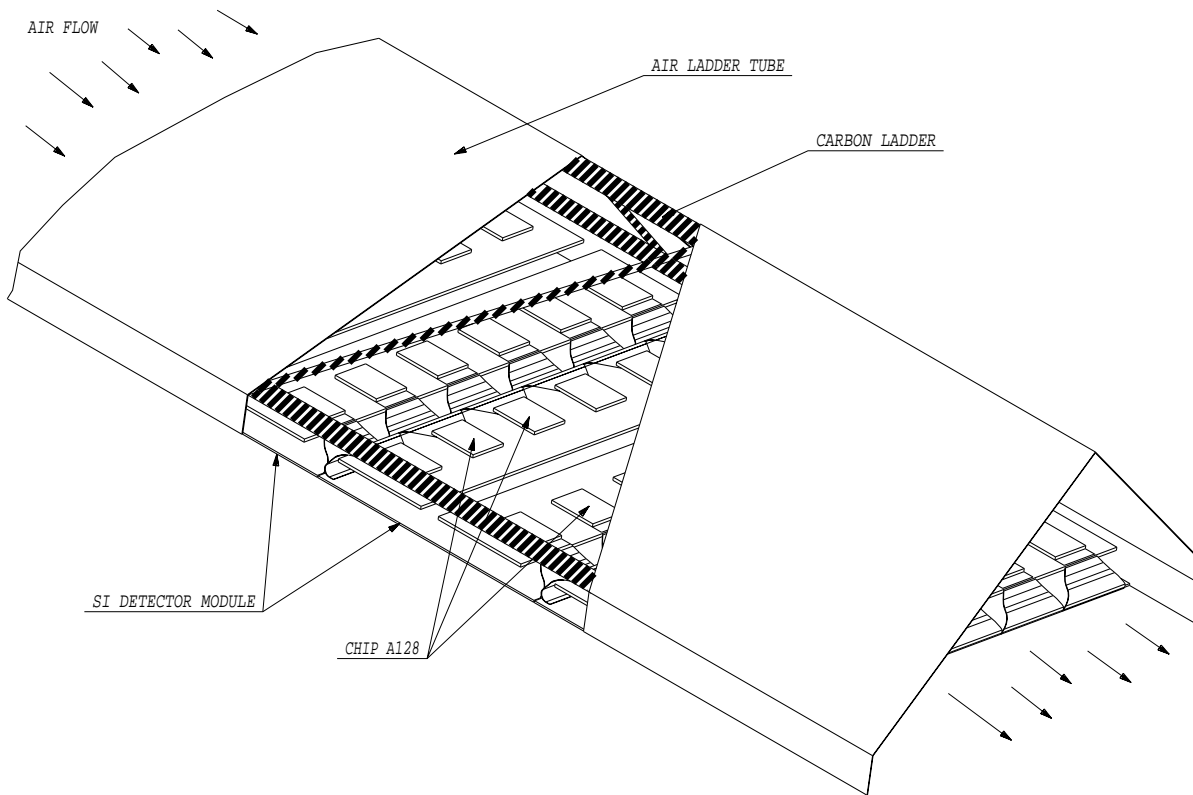


**Figure 54:** Detector module view with air cooling (second option).

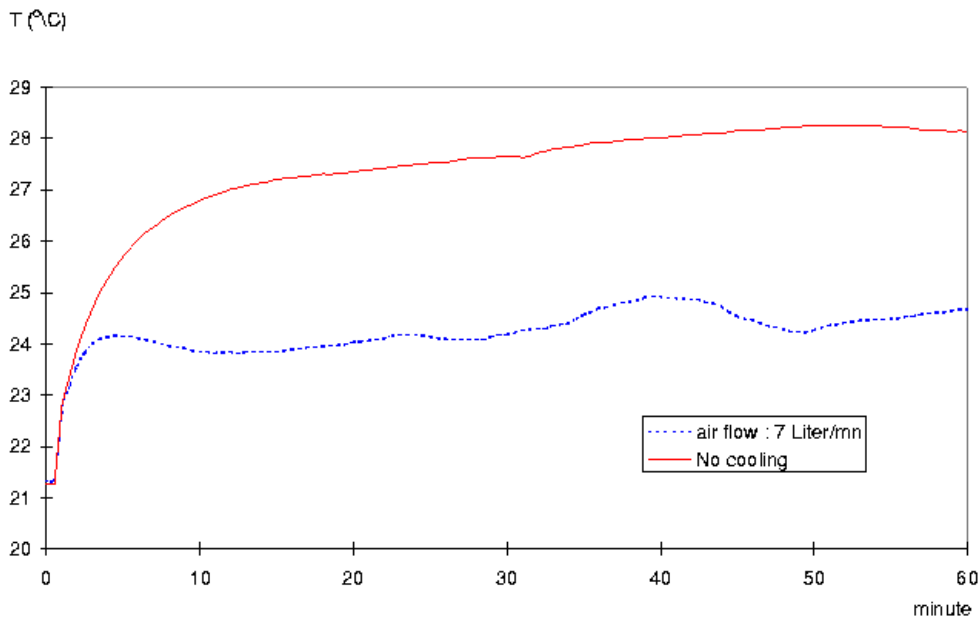


**Figure 55:** Chip temperatures as a function of time with no cooling and with an air flow of 7 liters per minute

## 4. Integration issues

### 4.1 Total power dissipation

#### 4.1.1 Evaluation of the SSD barrel power dissipation

The power consumption of the barrel is estimated to :

- 164 W for front end electronics (see Appendix B)
- 80 W for the ADC&control board (see 3.5.5 ADC&control board)

This leads to a total power dissipation of the barrel of roughly 250 W.

### 4.2 Timing

#### 4.2.1 TPC timing requirement

Timing delay for the readout has been asked by the TPC to the SVT in order to wait for the end of the signal drift and the data sampling. So the SSD will follow this requirement also : 100  $\mu s$  of delay before starting the readout.

#### 4.2.2 SSD trigger requirement

Due to the shaping time range of the SSD front end electronics from 1.4  $\mu s$  to 1.8  $\mu s$ , a trigger time not higher than 1.8  $\mu s$  is required by the SSD. In case of a trigger time lower than 1.4  $\mu s$ , a delay can be implemented in the Readout Control board.

### 4.3 TPC high voltage

The drift field in the TPC, depending on the gas used, could be as high as  $\sim 400V/cm$ , which would require a central potential of  $-80kV$ . In such a case, Corona discharge could arise in the gap between the Inner Field Cage (IFC) voltage degrader and the SVT-SSD integration envelope at ground potential.

The Inner Field Cage (IFC) is located at  $R_{IFC} = 466.80mm$ , its center at  $z = 0$  is at potential  $-80kV$ .

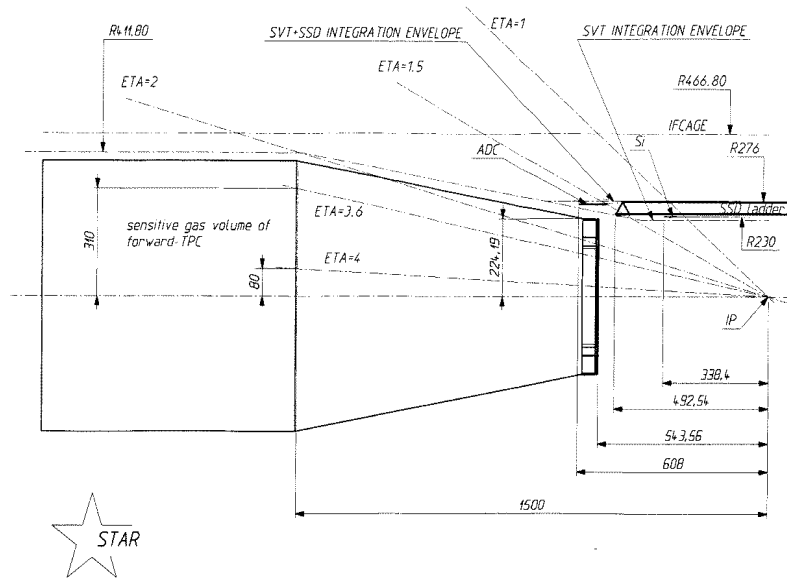


**Figure 56:** Layout of the SVT-SSD with the integration envelope.

The Silicon Strip Detectors are glued in arrays of 16 wafers on space frame beams called “carriers”. The whole SSD barrel (in a clamshell design) features 20 Carbon fiber beams (Fig. 57).



**Figure 57:** The 20 ladders of the SSD support structure.

This structure is enclosed in a thin aluminized kapton window (SVT-SSD integration envelope) seating on the 20 tips of the prismatic Carbon fiber support structure at an average radius of  $R_{SSD} = 276mm$ , extending to  $z = \pm 608mm$ . From those points to  $z = \pm 1500mm$ , the SVT-SSD integration envelope has a conical shape and ends with a cylindrical part with  $R = 411,80mm$  (Fig. 58). Dry air is circulating between the IFC and the SVT-SSD integration envelope. Hence the gap between the

IFC and the integration envelope varies from  $\Delta R(z=0) = 190.80mm$  at the central part, to  $\Delta R(z \geq 1500) = 55mm$ .



**Figure 58:** The SSD integration envelope.

The integration envelope is at ground potential, whereas the IFC potential ( $80kV$ ) is degraded from the center to both grounded end sides with a gradient of  $\sim 400V/cm$ . Electric field irregularities arise on the integration envelope slope changes ( $z = \pm 608mm$  and  $z = \pm 1500mm$ ) where the transverse gradient is  $\frac{\delta V}{\delta r} = \frac{56kV}{190} \simeq 2.9kV/cm$  and  $\frac{\delta V}{\delta r} = \frac{20kV}{55} \simeq 3.6kV/cm$ , respectively. Furthermore, field singularities might arise on the 20 tips of the prismatic SSD integration envelope. Fig. 59 shows an example of a carrier rod with the grounded integration envelope tangent to it.

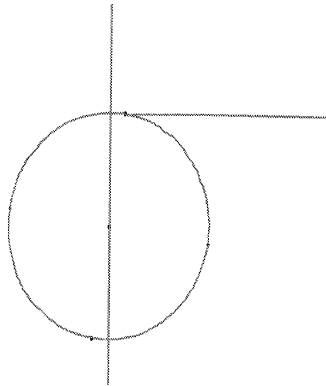


**Figure 59:** Tip of a rod.

### 4.3.1 2D simulations

There are two critical regions:

- the central region at  $z = 0$  and  $z = \pm 608mm$
- the “cylindrical to conical” connecting region at  $z = \pm 1500mm$

We have performed a 2D simulation for that central part ( $z = 0$ ) where the aluminized kapton foil is tangent to the Carbon fiber beams. Fig. 60 shows the results of that simulation. The average field strength is  $5.1kV/cm$  and rises to  $5.6kV/cm$  at the tip of the Carbon fiber beam. Close to the tip of the beam and the tangent point ( $\Delta z = 0.5mm$ ) of the kapton foil, the field has a sharp discontinuity (Figs. 60,61) dropping from  $5.6kV/cm$  down to  $4.7kV/cm$ . Those values are not critical in a dry air environment. They are well within the requirements that the field generated by structures placed in the inner field cage should not cause a field in excess of  $8kV/cm$  when the TPC is operated at the maximum drift potential of  $85kV$ .

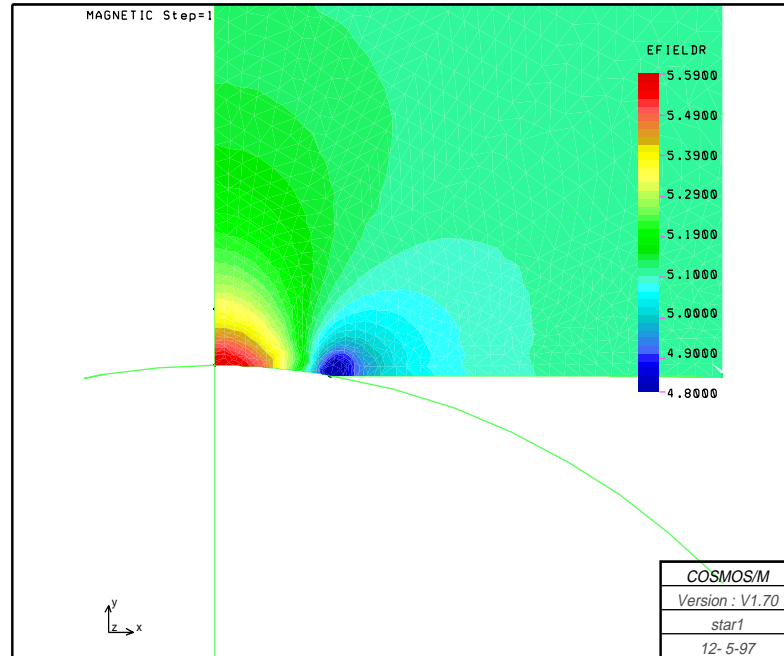


Figure 60: 2D simulation near the tip of a carrier rod.

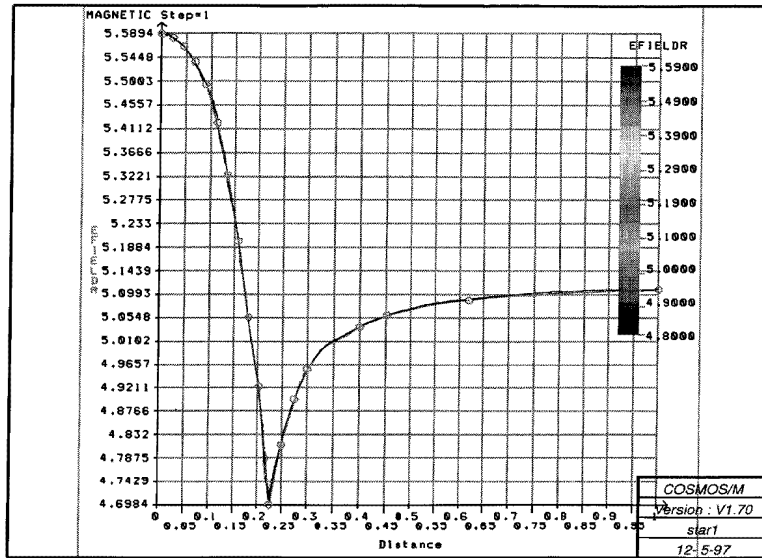


Figure 61: E-field irregularity on the tip of a rod.

#### 4.4 Radiation length of the SSD

The radiation length of the SSD material has been estimated by using a detailed description of the SSD geometry and materials in GEANT. The various described elements include silicon strip detectors, ladders made in carbon fiber structure, beryllium heat bridges, silicon FEE, beryllium oxide hybrids, aluminium cooling pipes (carrying water), kapton cables (in copper) and beryllium cable holders (see Figs. 44,45,46).

Simulations have been made following the example of the calculations performed for the SVT [45]. They are done in GSTAR by taking straight line trajectories from the main vertex and with  $\eta$  ranges from -1.2 to 1.2 and over a complete coverage in azimuthal angle ( $\phi$ ).

The total radiation length of the SSD is evaluated at 0.69 %  $X_0$ . The contributions of the various materials are shown in in Fig. 62 and Table 8 summarizes the detailed radiation length values. Two sets of values for the radiation length contributions are given : the first ones correspond to the mean value averages over  $-1.2 < \eta < +1.2$  without any correction due to incident angle effect. The second ones (“normalized mean value” are corrected by a normalized factor which gives the value of the radiation length at normal incidence.

One sees that the major contribution is due to the silicon strip detectors and the carbon fiber ladders, representing about 60 % of the total.

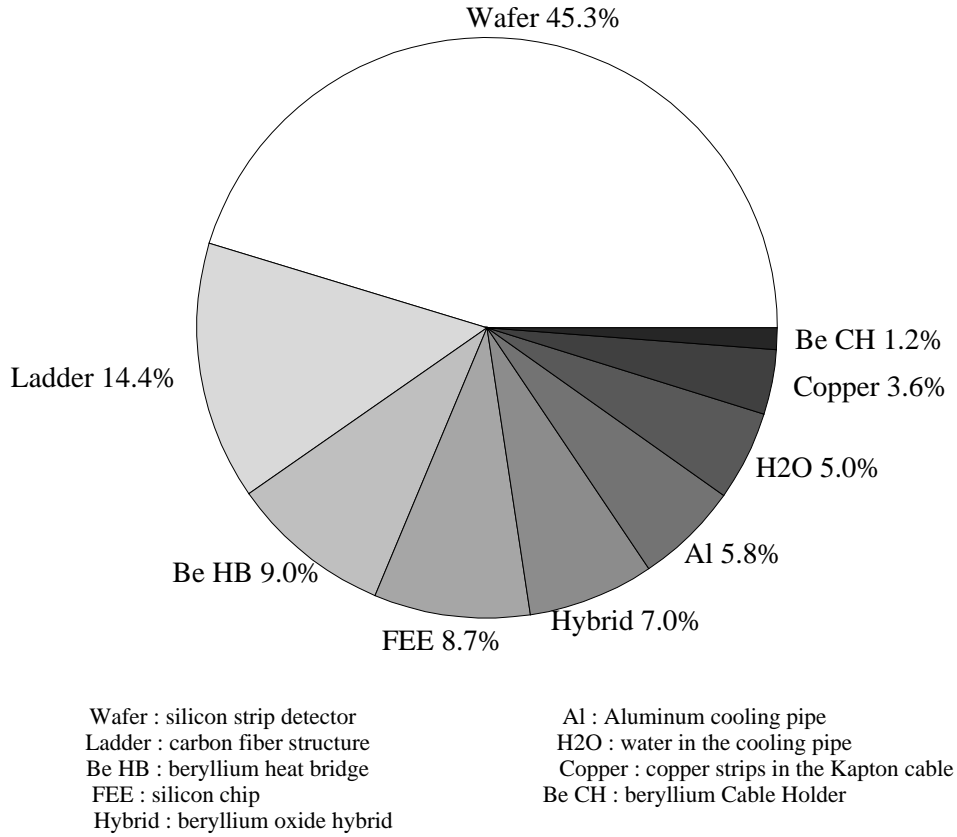


**Figure 62:** Contributions to the SSD 0.69 % radiation length.

Fig. 63 shows the radiation length of the SSD as a function of the pseudo-rapidity. Two hybrid–FEE modules are used per wafer which induce 16 peaks in the distribution. It is presented as a fraction and not as a percentage (hence, results are consistent with 0.69 %  $X_0$ ). The enhancement of the radiation length with  $\eta$  is due to the increase of the incident angle.

SSD PART	Mean value of the radiation length	Mean value of the normalized radiation length	Contribution of the part
Wafer (Si)	$0.3953 \cdot 10^{-2} X_o$	$0.3155 \cdot 10^{-2} X_o$	45.26%
Heat bridge (Be)	$0.7885 \cdot 10^{-3} X_o$	$0.6308 \cdot 10^{-3} X_o$	9.05%
Cable holder (Be)	$0.1064 \cdot 10^{-3} X_o$	$0.8333 \cdot 10^{-4} X_o$	1.19%
Hybrid (BeO)	$0.6049 \cdot 10^{-3} X_o$	$0.4885 \cdot 10^{-3} X_o$	7.00%
Chip (Si)	$0.7590 \cdot 10^{-3} X_o$	$0.6037 \cdot 10^{-3} X_o$	8.66%
Cooling pipe (Al)	$0.5044 \cdot 10^{-3} X_o$	$0.4040 \cdot 10^{-3} X_o$	5.80%
Cooling pipe ( $H_2O$ )	$0.4366 \cdot 10^{-3} X_o$	$0.3471 \cdot 10^{-3} X_o$	4.98%
Ladder (carbon fiber)	$0.1266 \cdot 10^{-2} X_o$	$0.1007 \cdot 10^{-2} X_o$	14.45%
Kapton cable (Cu)	$0.3310 \cdot 10^{-3} X_o$	$0.2519 \cdot 10^{-3} X_o$	3.61%
Total SSD	$0.8750 \cdot 10^{-2} X_o$	$0.6971 \cdot 10^{-2} X_o$	100.00%

Table 8: Contribution of the different parts of the SSD in the radiation length

Fig. 64 shows the radiation length as a function of the azimuthal angle for the mid-rapidity region  $-1.2 < \eta < +1.2$ . The trend of the distribution reflects the regular repartition of the SSD material completed by the 20 support structures.

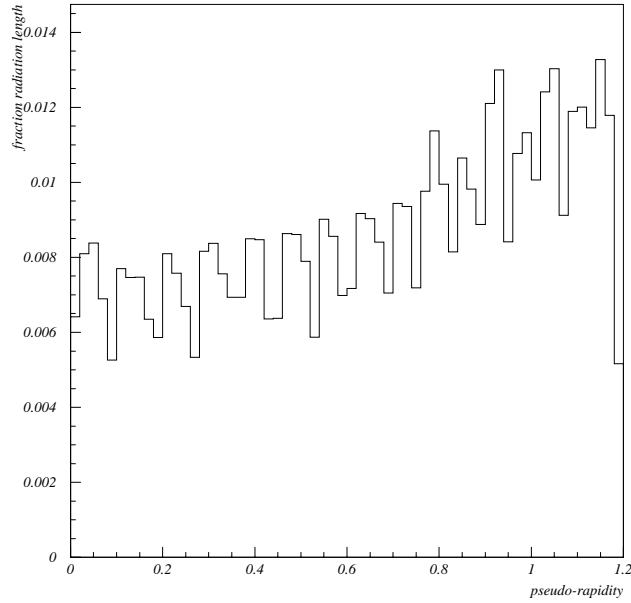
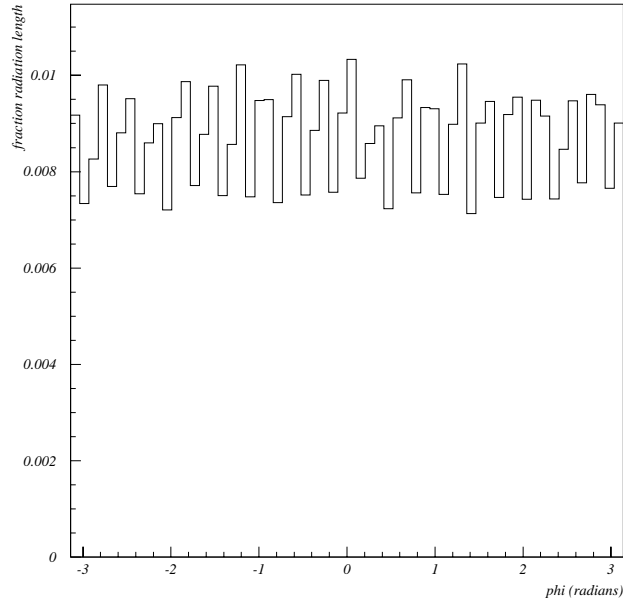


Figure 63: SSD radiation length as a function of pseudo-rapidity.



**Figure 64:** SSD radiation length as a function of the azimuthal angle.

Those radiation length calculations are preliminary, indeed it is needed to carefully study some particular points as:

- removing the BeO hybrid by processing the conductor layer directly on the Be heat bridge: it will decrease the total radiation length by  $0.49 \cdot 10^{-3}$ .
- investigating the cooling system to use, if possible, less material and a lighter one than aluminium.
- it must be notice that connection cables between hybrids and ADC boards have not been taken into account. Nevertheless, the possibility to use Kapton cables with aluminium strips instead of copper is under study.

## 4.5 Cable issues (see Appendix C)

### 4.5.1 Cables along the cones

The cables running along the cones are the following:

- 24 power cables of 3 conductors (AWG20)
- 6 shielded cables of 20 conductors
- 4 shielded cables of 26 conductors

This leads to 10 flat cables and 24 power cables per end of the SSD barrel.

### 4.5.2 Cables from the TPC wheels to the platform

The cables running from the TPC wheel to the platform are the following:

- 48 power cables of 3 conductors (AWG16)
- 16 shielded cables with 20 conductors

### 4.5.3 Cable crosstalk tests

A cable crosstalk test is required by the SVT. It consist in running two cables for about 2 meters :

- a digital cable of the same kind of the SSD digital cable (shielded with 20 conductors),
- an analog cable of the same kind of the SVT analog cable (shielded with 3 conductors).

It has been estimated that the crosstalk from the digital cables on the analog ones would be less than 2 mV. In order to reach this value, the following setup has been installed :

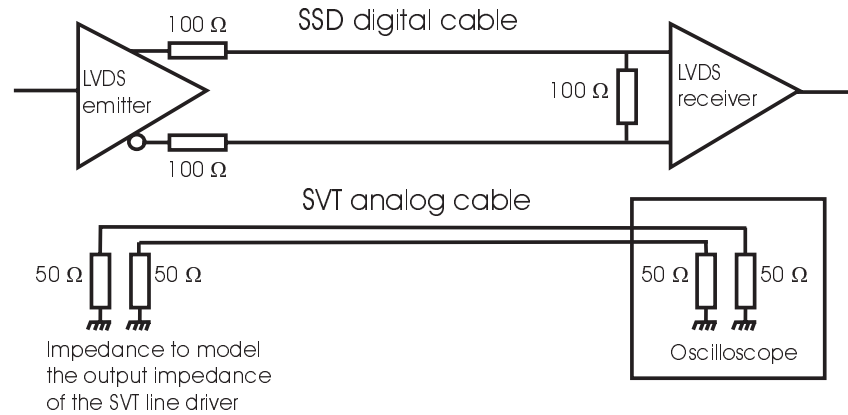


**Figure 65:** Crosstalk test setup

The result is the following :

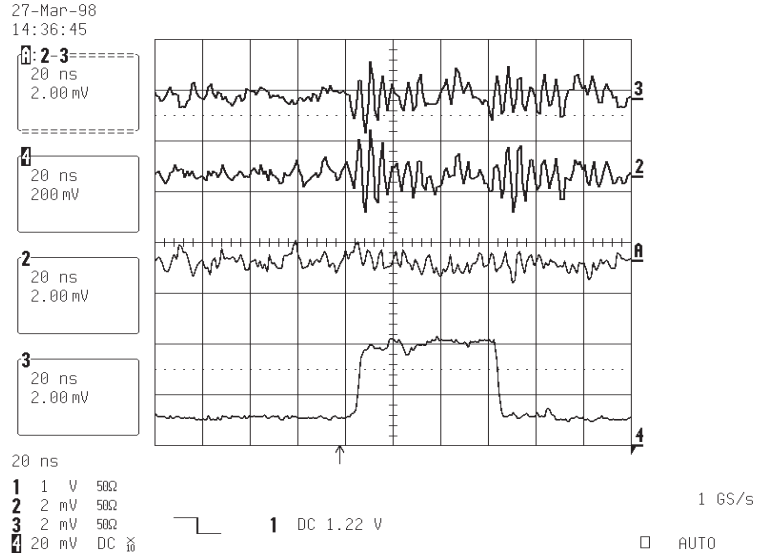


**Figure 66:** Channel 2 and 3 are the two analog channels of the SVT. Channel A is the difference of channel 2 and 3. Channel 4 is a LVDS signal in the digital SSD cable.

It can be concluded that, with an appropriate impedance adaptation, the crosstalk can be reduced to the ground noise level.

#### 4.6 Room requirement on the TPC wheel

On the TPC wheel, our data transfer system requires room for the following board for each end of the SSD barrel :

- 2 "Readout&Control" boards
- 2 power transition boards

#### 4.7 Room requirement on the platform

To respect the two different voltage levels for a ladder, two cabinets of racks are needed.

One contains twenty  $\pm 2V$  supplies for FEE and readout and two  $\pm 2V$  supplies for PCB strapped to ground level. The other contains the same twenty two supplies plus twenty high voltage supplies (depleting voltage); the equipments of this cabinet refer to floating voltage.

Each cabinet has also one interface board, two JTAG ports and two parallel ports for address&control bus. The interface board receives and converts temperature measurements for half the ladders, voltage and current measurements from ladders and high voltage measurements from the supplies in its cabinet. It sends also commands to control the voltage supplies. A PC installed near those cabinets drives the interface boards and the JTAG ports through a protocol to be defined.

From those two cabinets the number of conductors going out to the detector is :

- 60 for  $\pm 2V$  supplies for FEE strapped to ground level,
- 60 for  $\pm 2V$  supplies for FEE strapped to high voltage,
- 24 for  $\pm 2V$  supplies for PCB,
- 20 for temperature sensors,
- 160 for  $\pm 2V$  voltage sensors,
- 40 for JTAG (in differential),
- 32 for address&control bus (in differential).

## SSD Collaboration

At present, the SSD collaboration consists of five institutions :

- SUBATECH, Nantes
- IReS, Strasbourg
- LEPSI, Strasbourg
- Institute of Physics, Warsaw
- Wayne State University, Detroit

The main effort is lead by the french group from SUBATECH. The principal activity of the physicists from SUBATECH and IReS is the R&D program common for STAR and ALICE projects (see tables 10 and 11). Both institutions are still involved in the analysis of the data from SPS and FOPI experiments.

## Schedule and manpower

The SSD milestones, in accordance with SVT ones, are shown in tables 12 and 13. The proposed schedule will allow the completion of the SSD in June 2000, which coincides with the SVT implementation.

## Cost estimate

The overall cost of the construction of the SSD detector is estimated at 8.230 million FF (1.372 M\$). This global cost is detailed in Tables 14 and 15. The cost of manpower is about 9 MF (1.5 M\$).

The detailed cost estimate and schedule have been submitted for approval of :

- Institut National de Physique Nucléaire et de Physique des Particules (IN2P3)
- Ecole des Mines de Nantes
- Conseil Régional des Pays de la Loire
- Université de Nantes

At present following funds are allocated :

- IN2P3 : 4.230 MF (705 k\$) for construction and 9 MF (1.5 M\$) for manpower.
- Ecole des Mines : 3 MF for construction (0.5 M\$)

We apply for DoE additional funds in order to cover items (see Table 9) which will be purchased in the United States. Conventional systems include racks, crates, cabling and platform equipment. The DAQ components will include receiver and mezzanine cards, Gigalinks, crate and workstation.

DAQ	70 k\$
Conventional systems and installation	15 k\$
Total	85 k\$

Table 9 : Funds requested to the DoE

The Tape Automated Bonding (TAB) is a new technology proposed by two French companies Bull and Dassault. The application of the industrial process to the nuclear physics experiments requires a dedicated R&D. The use of the TAB technology is envisaged for ALICE (ITS and TPC) experiment. We plan to apply it for the SSD. A request will be made to French agencies in order to benefit from special funds allocated for the R&D related to industrial process and common for STAR and ALICE experiments. Regarding the great interest of the TAB technology for future development of the nuclear physics instrumentation we intend to invite U.S. institutions to share and contribute to our effort.



ACTIVITY PLANNING OF PHYSICISTS AT IReS

Years	1996	1997	1998	1999	2000	2001	2002	2003	2004	2005	2006	2007	2008
<b>FOPI</b>	⊙0.5	0.5	0.5										
<b>STAR</b>	Analysis			Production and tests	Assembly								
<b>ALICE</b>	Common R&D			Production and tests	Assembly and Mounting	Analysis	Global Mounting and Integration	Analysis					
<b>Total Physicists</b>	5	6	7	7	7	6	5						

⊙ Ended in 1998  
 Present Manpower : 5 Physicists  
 \* 1 CR CNRS requested in 1997  
 ( ) Manpower staying permanently at BNL

Additional Manpower expected \*\* 1 MC University  
 \*\*\* 1 CR CNRS (1 person leaving)  
 + 1 person leaving  
 ++\* 1 CR CNRS (2 persons leaving)

Table 11 : Planning of Physicist activities at IReS

## MANPOWER SCHEDULE OF SUBATECH FOR STAR EXPERIMENT

Table 12 : Planning for manpower at SUBATECH

Year	1997		1998		1999		2000	
	june		march	june	march		march	june
Detectors	<u>Prototypes order</u> ½ I	<u>Assembly + Test</u> 1 postdoc + 1 T	<u>Final design</u>		<u>Fabrication</u>	<u>Tests</u> 1 T		
ADC board	<u>Prototype + tests</u> ½ I + ½ T		<u>Final design</u> ½ I		<u>Tests + assembly</u> ½ T			
Data transmission and compression			<u>Prototype + tests + design</u> 1 I + 1/2 T		<u>Tests + assembly</u> 1/3 I + 1/2 T (2)			
Mechanics + cooling		<u>Prototypes</u> 1/16 I + 1 T		<u>Fabrication</u>	<u>Tests + assembly</u> 1/8 I + 1 T			
Integration tools			<u>Design</u> ¾ I + 2 T	<u>Fabrication</u> 1/16 IE	<u>Assembly</u> ½ I + 2T (2)			
SVT support		<u>Design</u> ¾ I	<u>Fabrication</u>	<u>Assembly</u> 1/4 I + 2 T	(1)			

(1) 4 persons during 2 weeks at BNL  
 (2) 4 persons during 3 weeks at BNL

I : engineer  
 T : technician

Dead line

22/07/98

## MANPOWER SCHEDULE OF IReS FOR STAR EXPERIMENT

year	1997 june		1998 march june		1999 march june		2000 march june	
Detectors	Prototypes order $\frac{1}{2}$ I	Assembly + Test $\frac{1}{2}$ I + 1 T	Final design		Fabrication Tests 1 T			
Cabling			Prototypes + tests $\frac{1}{3}$ I + 1 T		Final design $\frac{1}{3}$ I			
Hybrids	Prototypes + tests $\frac{2}{3}$ I + 1 T			Final design $\frac{2}{3}$ I				
Front end electronics	Prototypes + tests 1 I + 1 T			Fabrication	Tests + assembly 1 I + 1 T			
detector + electronics assembly					Assembly + test 1 I + 1 T			
Slow control	Prototypes 1 I + 1 T			Fabrication	Test + assembly 1 I + 1 T (1)			

(1) 4 persons during 3 weeks at BNL

Dead line

Table 13 : Planning for manpower at IReS

### BUDGET PLANNING FOR STAR EXPERIMENT

Year	1997		1998		1999		2000	
	June		March	June	March	June	March	June
Detectors	<u>Prototypes order</u> 600 kF	<u>Assembly + Test</u> 200 kF	<u>Final design</u>	1800 kF	<u>Fabrication</u> 1800 kF	<u>Tests</u> 40 kF		
Front end electronics	<u>Prototypes + tests</u> (1)		(1)	300 kF	300 kF	<u>Fabrication</u> 50 kF	<u>Tests</u>	
Hybrids	<u>Prototypes + tests</u> 50 kF			<u>Final design + fabrication</u> 400 kF				
Cabling				<u>Prototypes + tests</u> 50 kF	<u>Final design + fabrication</u> 100 kF			
Detector + electronics assembly					<u>Assembly + test</u> 400 kF			
Mechanics + cooling		<u>Prototypes</u> 50 kF		<u>Fabrication</u> 300 kF	<u>Tests + assembly</u> 100 kF			
Integration tools			<u>Design</u> 50 kF	<u>Fabrication</u> 350 kF		<u>Assembly</u> 20 kF	20 kF (4)	
SVT support	<u>Design</u> 20 kF		<u>Fabrication</u> 230 kF	<u>Assembly</u> 20 kF	(4)			

Dead line

22/07/98

Table 14 : Planning for budget (part 1)

Table 15 : Planning for budget (part 2)

Year	1997		1998		1999		2000	
	June		March	June	March		March	June
Data transmission and compression				Prototype + tests 500 kF (2) (3)		Tests + assembly 20 kF (4)		
ADC board		Prototype + tests 30 kF		Final design + fabrication 150 kF		Tests + assembly 10 kF		
Slow control		Prototypes 50 kF (2)			Fabrication 200 kF (3)	Test + assembly 20 kF (4)		
total per year		1000 kF		4350 kF		2860 kF		Dead line 20 kF
							Total 8230 kF	

- (1) 200 kF from ALICE project  
(2) used to buy prototypes at BNL  
(3) used to finance production in US  
(4) used to finance assembly on site

# Appendices

## Appendix A : Specifications of the double sided detector sent to the founder

- Expected radiation level: about 1 krad
- Chip size: 75 x 42 mm overall
- Number of strips: 768 on each side
- Length of the strips: about 40 mm
- Bonding pads: double on each end
- Pitch: 95  $\mu\text{m}$ . No floating strips
- Stereo angle: 35 mradian i.e.  $\pm 35/2$  mradian on each side with respect to the edge
- Thickness:  $300 \pm 15 \mu$  on the set of detectors  
 $\pm 5 \mu\text{m}$  on one detector
- Cutting: angle  $\pm 0,5$  mradian, position  $\pm 25 \mu\text{m}$
- Width of the strips: 15  $\mu\text{m}$  to be tuned for capacitance ratio
- Capacitance value:  $> 80 \text{ pF}$  to be tuned for capacitance ratio
- Capacitance ratio :  $> 20 \text{ pF}$  as reasonably high as possible
- Capacitance breakdown voltage:  $> 60 \text{ V}$  or  $>$  operational depletion voltage  $V_d$
- Guard and bias structure: distance between cutting line and active area
- Guard ring:  $< 1 \text{ mm}$ , all around the detector, metallized, accessible
- Bias ring: in the guard ring, around the detector, metallized, accessible
- Aluminum thickness: minimum thickness for bonding
- Leakage current through the guard ring:  $< 5 \mu\text{A}$  at depletion voltage  $V_d$
- Detector leakage current:  $< 2 \mu\text{A}$  at depletion voltage  $V_d$
- Strip leakage current:  $< 5 \text{ nA}$  at depletion voltage  $V_d$
- Depletion voltage:  $< 60 \text{ V}$
- Biasing scheme: FoxFet or punch thru on both sides
- Biasing resistors:  $> 10 \text{ M}\Omega$  on both sides
- Passivation on both sides: for example by LTO
- Dead channel rate:  $< 3 \%$  on each side with a goal of 1 %

These specifications have been sent to the founder in September 1997, for a prototype fabrication.

## Appendix B : Current and power consumption evaluation for the SSD layer at STAR

Due to an asymmetric design for saving power dissipation, the analog part of the integrated circuit Alice 128C can be modeled as shown in Fig. 67:

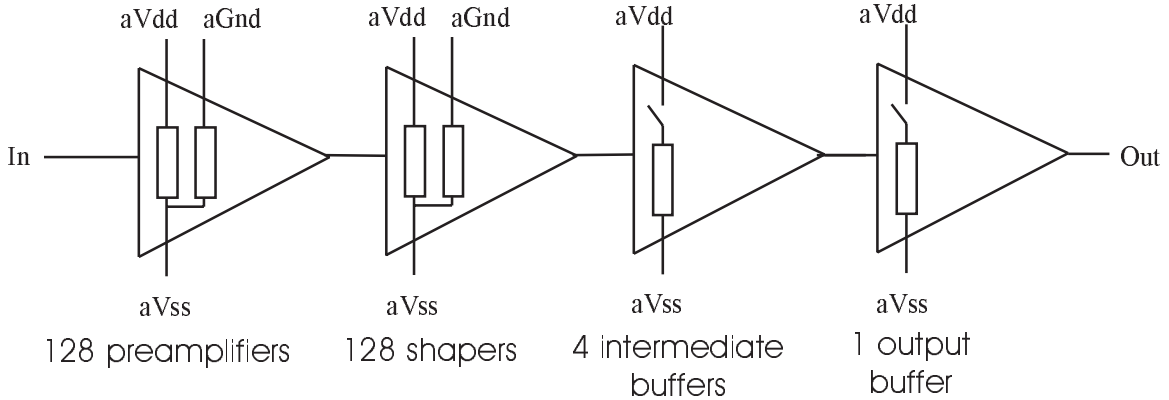


**Figure 67:** Analog part model of the Alice 128C chip.

The currents used by the circuit are the following for each part of the chip and for each different analog power supply:

	aVdd	aGnd	aVss
preamplifier	12 $\mu$ A	91 $\mu$ A	103 $\mu$ A
shaper	17 $\mu$ A	15 $\mu$ A	32 $\mu$ A
intermediate buffer	1850 $\mu$ A	0 $\mu$ A	1850 $\mu$ A
output buffer	8450 $\mu$ A	0 $\mu$ A	8450 $\mu$ A

Two main functioning states can be defined for the chip:

- the sampling state: the chip is working and waiting for the hold signal; only the preamplifier and the shaper are biased,
- the acquisition state: once the trigger and the hold command are sent, the chip is read-out when the shift-in signal is present in it; then 4 intermediate buffers and the output buffer are biased; this is the worst case for the power consumption.

The following table shows the current consumed by the whole chip and for the two states:

	aVdd	aGnd	aVss
sampling state	3.712 mA	13.568 mA	17.280 mA
acquisition state	19.562 mA	13.568 mA	33.130 mA

Same table for 6 chips which corresponds to one side of a detector (only one chip of the six is read-out):

	aVdd	aGnd	aVss
sampling state	22.272 mA	81.408 mA	103.680 mA
acquisition state	38.122 mA	81.408 mA	119.53 mA

In the SSD barrel read-out strategy, only one detector is read-out per half ladder which corresponds to 16 detectors. So the total currents per half ladder is the following:

	aVdd	aGnd	aVss
sampling state	356.352 mA	1302.528 mA	658.880 mA
acquisition state	372.202 mA	1302.528 mA	1674.730 mA

With a  $\pm 2$  V power supply, those results lead a power consumption per half ladder of:

- sampling state: 4030.464 mW
- acquisition state: 4093.864 mW

The both results can be approximate at 4.1 W per half ladder without doing a big error. That gives a total power dissipation of the front-end electronics for the whole barrel of:

$$P_d = 164 \text{ W}$$

## Appendix C : Cables and signal summary at different level of the SSD barrel at STAR

To reach a design with a minimum of defect, it is necessary to summarize the signals and cables at the following level of the electrical system :

- the detector,
- the FEE : ALICE 128C,
- the hybrid,
- the interface ladder/'ADC&control' board,
- the 'ADC&control' board interfacing to :
- the slow control (JTAG system, power supply, detector biasing and temperature control),
- the 'Readout&control' board,
- the DAQ system.
- the 'Readout&control' interfacing to :
- the slow control (JTAG & control),
- the trigger,
- the DAQ,
- the Gigalink emitter.

### 1 Detailed description of signals between the different subsystems of the SSD

#### 1.1 The detector :

- 768 strips per side connected to the FEE
- guard ring and biasing pad (low and high voltage)

Those links will be made via TAB.

To be defined after detector design review.

## 1.2 The FEE : Alice 128C

The different signals are described below according to the 'ALICE128C technical report' written by the designers.

### Power and biasing signals :

avss	analog +2V	2
gnd	analog ground	2
avdd	analog -2V	2
dvss	digital -2V	1
dvdd	digital +2V	1
dvss-pery	digital -2V for pads	1
dvdd-pery	digital +2V for pads	1
genvss	digital -2V for pulse generator	1
genvdd	digital +2V for pulse generator	1
CUREF	analog current reference	1

### JTAG signals :

TMS	JTAG mode select	1
TCK	JTAG clock	1
TDO	JTAG data output	1
TDI	JTAG data input	1
TRSTB	JTAG general reset	1

### Control and readout :

PWRRST	Power reset	1
LVDS-Test	Test pulse	2
LVDS-Hold	Hold pulse	2
LVDS-RCLK	Readout clock pulse	2
TOKENIN	Readout token output	1
TOKENOUT	Readout token output	1
ANALOGOUT	Analog output	1

### TOTAL :

Signals 22  
Pads 28



#### 1.4 The interface 'hybrid/ADC board' :

This interface drives 16 hybrids in parallel and is made of kapton cables with copper or aluminium conductors.

##### Power and biasing signals :

VDD	Digital & analog vdd	(com)	1
VSS	Digital & analog vss	(com)	1
GND	Analog ground	(com)	1
DetecBias	Detector biasing (ground or high voltage)	(com)	1
GuardRing	Guard ring biasing (ground or high voltage)		1

##### JTAG signals :

TMS	JTAG mode select	(com)	1
TCK	JTAG clock	(com)	1
TDO	JTAG data output	(dais)	1
TDI	JTAG data input	(dais)	1

##### Control and readout :

PWRRST	Power reset	(com)	1
LVDS-Test	Test pulse	(com,diff)	2
LVDS-Hold	Hold pulse	(com,diff)	2
LVDS-RCLK	Readout clock pulse	(com,diff)	2
TOKENIN	Readout token output	(dais)	1
TOKENOUT	Readout token output	(dais)	1
ANALOGOUT	Analog output	(com)	1

##### **TOTAL :**

Signals 16  
Lines 19

We have to think of the temperature control. For the moment, there is no precise requirements. We may have something very simple which can monitor an excess of heating. In that case only two independant lines are necessary for one ladder.

Total lines 21

(com = common signal, dais = daisy chained signal from one hybrid to the next one, diff = differential signal)

### 1.5 The 'ADC & control board' :

Each ladder will have two 'ADC & control board', one at both ends. This board will have three main features :

- to do the analog to digital conversion,
- to generate control signals,
- to interface other systems necessary to control, drive and power up the FEE.

In the readout strategy, 10 ADC&control boards (of the 20 ones at each end of the SSD barrel) are multiplexed together.

To this board several systems are connected :

- the front end electronics (described before),
- the slow control (connected indirectly via the power supply and detector biasing distribution, the temperature monitoring system and the
- Readout&control board with the JTAG),
- the Readout control board,
- the DAQ system.

The power supply and detector biasing distribution :

VDD	Digital & analog vdd	1
VSS	Digital & analog vss	1
GND	Analog ground	1
VddSens	Vdd sensor	2
VssSens	Vss sensor	2
DetecBias	Detector biasing (ground or high voltage)	1
HVSens	High voltage sensor	2

For reliability reasons, we plan to have two independent power supplies per ladder (one per side of the detector). All of those lines run along the cone to a transition board located on the TPC wheel and then to the platform.

The lines GND and Detectbias plus HVSens are exclusive. It depends whether it is the high voltage end of the ladder or the low voltage one.

VDD and VSS are floating power supply for the high voltage end.

Temperature monitoring system :

One temperature monitoring channel per ladder.

TempSens    Temperature sensor    2

The 'Readout control' board :

JTAG signals :

All the JTAG signal coming from the 'Readout control' board are common for ten ladders. The programming and the test of the FEE with the JTAG will be done using the 'Address&control' bus.

TMS    JTAG mode select    (com)    2  
TCK    JTAG clock            (com)    2  
TDO    JTAG data output    (com)    2  
TDI    JTAG data input    (com)    2

Test signal :

Test    Test pulse    (com,diff)    2

This signal is used with the JTAG and the Address&control bus to perform analog test.

Address&control bus :

This bus is used to multiplex 10 ADC&Control boards for the readout, the test and the programming of the FEE.

Address&control bus    (4 bits)    (com,diff)    8

Hold signal :

Hold    Hold pulse    (com,diff)    2

The Gigalink Emitter :

ADC data (10 bits)    data bus    (com,diff)    20

(com = common signal, diff = differential signal)

## 1.6 The Readout control board :

The main function of this board is to multiplex 10 ADC&control boards during the readout, the FEE test and programming. It also translates the trigger command word and the DAQ command word to control the readout.

### Slow control :

JTAG&control bus 20

### Trigger :

Trigger bus 4

### DAQ :

Control bus 4

## 1.7 Slow control :

The slow control controls the power supply and the high voltage of the barrel, monitors the temperature of the ladders and is able to perform the JTAG protocol for the initialisation and the testing of the front end electronics.

Two types of link are connected to the slow control :

- an external link already described part 1.6 (JTAG&control bus),
- an internal one via the VME bus to perform the control and the monitoring mentioned above.

## 1.8 Trigger :

A 4 bit trigger is defined in the 'Trigger/Clock distribution Tree' document as mentioned part 1.6.

## 1.9 DAQ :

The DAQ system will be the one already developed by BNL. As mentioned above, a 4 bit bus is foreseen but no real specifications are defined.

## 2 Summary of cables in the different parts of the SSD system :

### 2.1 Cables running along the cones :

Cables are summarised per end of clamshell. In the actual design, there is one end of each type at both ends of the SSD.

#### 2.1.1 low voltage end of the clamshell :

ADC&ladder power cables	10 VDD conductors 10 VSS conductors 10 GND conductors	   	10 shielded cables of 3 conductors (AWG20)
Power cables sensors	20 VddSens conductors 20 VssSens conductors	 	3 shielded cables of 20 conductors
Temperature control	20 TempSens conductors		
Line driver power cables	2 VDD 2 VSS 2 GND	   	2 shielded cables of 3 conductors (AWG20)
JTAG bus	10 diff. conductors		
Address&control bus	8 diff. conductors		1 shielded cable
Hold pulse	2 diff. conductors		of 26 conductors
Test signal	2 diff. conductors		
Data bus	20 diff. conductors		1 shielded cable of 20 conductors

### 2.1.2 high voltage end of the clamshell :

ADC&ladder power cables	10 VDD conductors 10 VSS conductors 10 DetecBias conductors	10 shielded cables of 3 conductors (AWG20)
Power cables sensors	20 VddSens conductors 20 VssSens conductors	3 shielded cables of 20 conductors
High voltage sensors	20 HVSENS conductors	
Line driver power cables	2 VDD 2 VSS 2 GND	2 shielded cables of 3 conductors (AWG20)
JTAG bus	10 diff. conductors	
Address&control bus	8 diff. conductors	1 shielded cable
Hold pulse	2 diff. conductors	of 26 conductors
Test signal	2 diff. conductors	
Data bus	20 diff. conductors	1 shielded cable of 20 conductors

### 2.1.3 summary of the cables running along one cone :

TYPE OF CABLES	NUMBER OF CABLES	REFERENCE NAME
shielded 3 conductors(AWG20)	24	power cable 1
shielded with 20 conductors	6	sensor cable
shielded with 26 conductors	2	'control signal' cable
shielded with 26 conductors	2	'data' cable height

These cables are connected at one end to the 'ADC&control' board and at the other end to different boards located on the TPC wheel :

- one transition board for the power cables,
- one transition board for the sensor cables,
- the 'Readout control' board for the 'control signal' cables,
- one transition board for the 'data' cables.

On the TPC wheel, there are two of those boards, one for each end of clamshell.

## 2.2 Cables running from the TPC wheels to the platform:

All the cables running from the TPC wheel to the platform are linked to the slow control. So the following cables are concerned :

- the power cables for the ladders and for the line drivers,
- the sensor cables (temperature and voltage),
- the JTAG and control bus.

TYPE OF CABLES	NUMBER OF CABLES	REFERENCE NAME
shielded with 3 conductors(AWG16)	48	power cable 2
shielded with 20 conductors	12	sensor cable
shielded with 20 conductors	4	JTAG&control cable

2.3 Cables running from the 'readout control' board to several systems :

2.3.1 Slow control :

Already mentionned in part 2.2

2.3.2 Trigger :

A 4 bit trigger command word is defined in the 'Trigger/Clock Distribution Tree' document, but no specification about the signal itself (differential, ECL or TTL ...).

The cable will be defined as soon as possible.

2.3.3 DAQ :

A 4 bit command word is foreseen in the 'Trigger/Clock Distribution Tree' document, but no meaning are defined yet.

A cable may be needed for this bus and will be defined as soon as possible.

## References

- [1] C.A. Pruneau Star Note 145.
- [2] Proposal for a Silicon Vertex tracker (SVT) as an upgrade of the STAR experiment at RHIC.
- [3] Alice Technical Proposal, CERN/LHCC 95-71, LHC/P3 (1995)
- [4] D. Liko, Star Note 87.
- [5] B. Batyunya et al., Alice Note 95-50.
- [6] D. Prindle, Star Note 153.
- [7] J. Rafelski, *Phys. Rep.* **88**(1982)331
- [8] P. Koch, B. Müller, and J. Rafelski, *Phys. Rep.* **142**, 167 (1986); *Z. Phys.* **A324**, 453 (1986).
- [9] J. Rafelski, J. Letessier and A. Tounsi, *Acta Phys. Pol.* **B27**, 1035 (1996).
- [10] J. Rafelski and B. Müller, *Phys. Rev. Lett* **48**, 1066 (1982); **56**, 2334E (1986).
- [11] J. Letessier, J. Rafelski, and A. Tounsi, *Phys. Lett.* **B389**, 586 (1996).
- [12] G. Odyniec, invited lecture at the QM'97-Tsukuba, to be published in proceedings *Nucl. Phys.* **A**, (1998).
- [13] D. Evans, (WA85 Collaboration), p. 79 in [19]. M. Venables, (WA94 Collaboration), p. 91 in [19].
- [14] S. Abatzis et al. (WA94 Collaboration) *Phys. Lett. B* **354**, 178 (1995); D. Evans et al. (WA85 Collaboration), *Nucl. Phys. A* **566**, 225c (1994).
- [15] S. Abatzis et al. (WA85 Collaboration), *Phys. Lett. B* **347**, 158 (1995); *Phys. Lett. B* **316**, 615 (1993).
- [16] T. Alber et al, (NA35 Collaboration) *Phys. Lett B* **366**, 56 (1996).
- [17] J. Rafelski, *Phys. Lett.* **B 262**, 333 (1991); *Nucl. Phys.* **A544**, 279c (1992).
- [18] *Strangeness in Hadronic Matter*, Tucson 1995, American Institute of Physics Proceedings Series Vol.340, J. Rafelski, ed. , New York 1995.
- [19] *Strangeness in Hadronic Matter*, Budapest 1996, T. Csörgö, P. Lévai and J. Zimányi, eds., *APHN N.S., Heavy Ion Physics* **4**, (1996), Akadémiai Kiadó, Budapest.
- [20] *Proceedings of SQM'97 meeting*, Thera, Greece, April 1997; A.D. Panagiotou et al. Edts., *J. Phys.* (1998).
- [21] G. Goldhaber et al., *Phys. Rev.* **120** (1960) 300.

- [22] G.I. Kopylov, M.I. Podgoretsky, *Yad. Fiz.* **15** (1972) 392; G.I. Kopylov, *Phys. Lett.* **B50** (1974) 472.
- [23] M.I. Podgoretsky, *Fiz. Elem. Chast. Atom. Yad.* **20** (1989) 628 (*Sov. J. Part. Nucl.* **20** (1989) 266).
- [24] S.E. Koonin, *Phys. Lett.* **B70** (1977) 43.
- [25] R. Lednicky, V.L. Lyuboshitz, *Yad. Fiz.* **35** (1982) 1316 (*Sov. J. Nucl. Phys.* **35** (1982) 770); Proc. Int. Workshop on Particle Correlations and Interferometry in Nuclear Collisions, CORINNE 90, Nantes, France, 1990 (ed. D. Ardouin, World Scientific, 1990) p. 42; JINR report P2-546-92 (1992) 1.
- [26] D.H. Boal, J.C. Shillcock, *Phys. Rev.* **C33** (1986) 549.
- [27] R. Lednicky, V.L. Lyuboshitz, B. Erazmus, D. Nouais, *Phys. Lett.* **B** (1996).
- [28] B. Erazmus, N. Carjan, D. Ardouin, *Phys. Rev.* **C44** (1991) 2663; B. Erazmus, L. Martin, R. Lednicky, N. Carjan, *Phys. Rev.* **C49** (1994) 349.
- [29] K. Werner, *Phys. Rep.* **232** (1993) 87.
- [30] Klaus Werner and Jörg Aichelin, *Phys. Rev.* **C52** (1995) 1584.
- [31] STAR Note, to be submitted.
- [32] Star Conceptual Design Report, PUB-5347 (1992)
- [33] see for example A guide to the High Energy Heavy-ion Experiments, Quark Matter '95, Ed. J. Thomas and P. Jacobs, UCRL-ID-119181 (1995) ; see also E864 and E896 at the AGS and NA52/NewMass at the SPS
- [34] C. Spieles et al., *Phys. Rev. Lett.* **76**, 1776 (1996)
- [35] J. Schaffner-Bielich et al., Preprint LBNL-39652, *Phys. Rev. C* (in press), and in Proc. of the Int. Symposium on Strangeness in Quark Matter '97, Thera (Santorini), Greece (1997)
- [36] S.A. Chin and A.K. Kerman, *Phys. Rev. Lett.* **43**, 1292 (1979)
- [37] e.g. C. Greiner, P. Koch and H. Stöcker, *Phys. Rev. Lett.* **58**, 1825 (1987) and J. Madsen, Proceedings of the Conf. of Strangeness 95', Tucson (1995).
- [38] C. Kuhn et al., Internal Note ALICE 95-49 (1995)
- [39] J.P. Coffin et al., Proc. of Int. Conf. on Nucl. Phys. At the Turn of the Millennium, Structure of Vacuum and Elementary Matter (1996), Wilderness/George, South Africa.
- [40] C. Spieles, private communication.
- [41] J.P. Coffin and C. Kuhn, in Proc. of the Int. Symposium on Strangeness in Quark Matter '97, Thera (Santorini), Greece (1997), see also *Journal of Phys.G.*

- [42] W. Dabrowski, P. Gryboś and M. Idzik, NIM A356 (1995) 241.
- [43] G. Tonelli, NIM A386 (1997) 129
- [44] InnovASIC, Inc, Specification for the STAR "Cluster-Finder ASIC", Juan Tabo (1996)
- [45] W.K. Wilson, R. Bellwied, C. Pruneau STAR Note 299